2018

Rigorous direct and inverse design of photonic-plasmonic nanostructures

https://hdl.handle.net/2144/30730

Boston University

BOSTON UNIVERSITY
COLLEGE OF ENGINEERING

Dissertation

RIGOROUS DIRECT AND INVERSE DESIGN OF PHOTONIC-PLASMONIC NANOSTRUCTURES

by

REN WANG
Msci. Physics, King's College London, 2012

Submitted in partial fulfillment of the
requirements for the degree of
Doctor of Philosophy
2018

Approved by

First Reader

Luca Dal Negro, PhD
Professor of Electrical and Computer Engineering
Professor of Materials Science and Engineering
Professor of Physics

Second Reader

Enrico Bellotti, PhD
Professor of Electrical and Computer Engineering
Professor of Materials Science and Engineering

Third Reader

Anna Swan, PhD
Associate Professor of Electrical and Computer Engineering
Associate Professor of Materials Science and Engineering
Associate Professor of Physics

Fourth Reader

Alexander V. Sergienko, PhD
Professor of Electrical and Computer Engineering
Professor of Physics

经：景到，在午有端，与景长。说在端。
说：景，光之人，照若射。下者之人也高；高者之人也下。
足蔽下光，故成景于上；首蔽上光，故成景于下。
在远近有端与于光，故景库内也。

墨子 (公元前470-391年)

Translation:

Phenomenon: The inverted image is formed on the screen after the small hole at where light rays crosses. The image size is related to the distance between the image and the hole.

Explanation: Taking a person as an object. When illuminated, light rays from the person travel in straight lines like arrows. The light from the lower part of the person is blocked and can only travel to the top part of the screen; and the light from the upper part of the person is also blocked and can only travel to the lower part of the screen. These can be tested by shadowing the feet or the head of the person, and only part of the image is formed. As a result, the location where each part of the image is formed is also affected by the distance, resulting varying size of the image.

Mozi (ca. 470-391 B.C.)

Acknowledgments

I would like to first acknowledge the continuous support and inspiration from my advisor, Prof. Luca Dal Negro, who provided me with this valuable opportunity to learn and apply theoretical understanding of physics to solve complex yet intriguing problems light-matter interactions. His broadly cross-disciplinary knowledge and the diversity of projects available in the group have shaped my PhD experience into an array of inspiring scientific endeavors, through which I have not only matured not in optical engineering but also become knowledgeable in areas including but not limited to scientific programming, statistical analysis, and network theory. The rest of the group have also provided opportunities for intra-group collaborations, which spans from analyzing properties of plasmonics structures to optimizing geometries for nanostructures with desired optical properties, and have turned into various publications. I would also like to thank our collaborators, in particular, Prof. Felipe A. Pinheiro, Prof. Carlo Forestiere, and Prof. Mike Kirby's group, for their contributions and active involvement in projects of this prospectus. I would also like to express my gratitude to my examination committee, Prof. Enrico Bellotti, Prof. Alexander Sergienko, and Prof. Anna Swan. Finally, I would like to acknowledge the support from the Army Research Laboratory to all the projects, as well as DARPA.

At the personal level, I would like to also express my gratitude to wife Yi Wei, who have been with me for the most of my PhD and making Boston a home to me. I would also like to thank both of our families, especially my mother, Chunli Zhang, for her continuous support and encouragement throughout my life; and my father, Jue Wang, who sparked my initial interest in physics. Finally, I would like to thank all important people and friends who have transformed my life at various stages. In particular, inspirational physics lectures and references from professors at the Physics Department of King's College London, including Prof. Alan Michette (undergraduate advisor), Prof. John Ellis FRS (physics master project advisor), Prof. Mairi Sakellariadou (cosmology project advisor), and Dr. Klaus Suhling (physics laboratory advisor), helped me to join the ECE department of Boston University. The Vice Principle of Hwa Chong Institution, Mr. Tan Pheng Tiong, who devoted his life to mainland Chinese scholars in Singapore, and supported us like a father. The Physics Department of Hwa Chong Institution (including formerly, The Chinese High School) provided me unique opportunities in working at its Photonics Laboratory during high school and finishing interesting projects on diffraction and spectroscopy of light, and in-depth course on special relativity. Ningbo Xiaoshi Middle School (Ningbo Foreign Language School)'s physics teachers, especially Ms. Bona He, where the foundational knowledge on ray optics and lens design continued to be useful well into my research life.

Ren Wang
PhD Candidate and Research Assistant
ECE Department Boston University

RIGOROUS DIRECT AND INVERSE DESIGN OF PHOTONIC-PLASMONIC NANOSTRUCTURES

REN WANG

Boston University, College of Engineering, 2018

Major Professor: Luca Dal Negro, PhD
Professor of Electrical and Computer Engineering
Professor of Materials Science and Engineering
Professor of Physics

ABSTRACT

Designing photonic-plasmonic nanostructures with desirable electromagnetic properties is a central problem in modern photonics engineering. As limited by available materials, engineering geometry of optical materials at both element and array levels becomes the key to solve this problem. In this thesis, I present my work on the development of novel methods and design strategies for photonic-plasmonic structures and metamaterials, including novel Greens matrix-based spectral methods for predicting the optical properties of large-scale nanostructures of arbitrary geometry. From engineering elements to arrays, I begin my thesis addressing toroidal electrodynamics as an emerging approach to enhance light absorption in designed nanodisks by geometrically creating anapole configurations using high-index dielectric materials. This work demonstrates enhanced absorption rates driven by multipolar decomposition of current distributions involving toroidal multipole moments for the first time. I also present my work on designing helical nano-antennas using the rigorous Surface Integral Equations method. The helical nano-antennas feature unprecedented beam-forming and polarization tunability controlled by their geometrical parameters, and can be understood from the array perspective. In these projects, optimization of optical performances are translated into systematic study of identifiable geometric parameters. However, while array-geometry engineering presents multiple advantages, including physical intuition, versatility in design, and ease of fabrication, there is currently no rigorous and efficient solution for designing complex resonances in large-scale systems from an available set of geometrical parameters. In order to achieve this important goal, I developed an efficient numerical code based on the Greens matrix method for modeling scattering by arbitrary arrays of coupled electric and magnetic dipoles, and show its relevance to the design of light localization and scattering resonances in deterministic aperiodic geometries. I will show how universal properties driven by the aperiodic geometries of the scattering arrays can be obtained by studying the spectral statistics of the corresponding Greens matrices and how this approach leads to novel metamaterials for the visible and near-infrared spectral ranges. Within the thesis, I also present my collaborative works as examples of direct and inverse designs of nanostructures for photonics applications, including plasmonic sensing, optical antennas, and radiation shaping.

Contents

List of Tables

List of Figures

List of Abbreviations

AR	Axial Ratio
CDA	Coupled Dipole Approximation
CMOS	Complementary Metal Oxide Semiconductor
CPA	Complex Prime Array
CPU	Central Processing Unit
DOS	Density Of States
EGO	Efficient Global Optimization (algorithm)
EIF	Expected Improvement Function
FDTD	Finite-Difference Time-Domain
FTIR	Fourier-Transform InfraRed (spectroscopy)
FWHM	Full-Width at Half Maximum
GP	Gaussian Process
IPR	Inverse Participation Ratio
ITO	Indium Tin Oxide
LDOS	Local Density Of States
LSPR	Localized Surface Plasmon Resonance
MIR	Mid-InfraRed (spectral range)
MLWA	Modified Long Wavelength Approximation
MoM	Method of Moments
NC	NanoCrystal
NIR	Near-InfraRed (spectral range)
PL	PhotoLuminescence
PMCHWT	Poggio-Miller-Chang-Harrington-Wu-Tsai (formulation)
RF	Radio Frequency
RWG	Rao-Wilton-Glisson (basis functions)
SERS	Surface Enhanced Raman Scattering
SIE	Surface Integral Equations
TCO	Transparent Conductive Oxide

Chapter 1

Introduction

”Light is, in short, the most refined form of matter.” (de Broglie, 1955) The deeper understanding of light and its interaction with matter through electromagnetic fields has not only laid the foundation to the two most important theories of the twentieth century, the theory of relativity and quantum mechanics, but also provided important insights to our universe through unifying fundamental forces of the nature using quantum electrodynamics as a prototypical framework. On the other hand, although physicists have developed accurate and advanced theoretical models describing light-matter interactions, controlling light and manipulating matters’ optical properties continue to present challenging engineering problems as researchers in the realm of photonics seeks to replicate the success of twentieth-century electronics in the new millennium.

Indeed, designing nanostructures with desirable electromagnetic properties is a central problem in modern research and device engineering in optics and photonics. Apart from discovering new types of optical materials through material engineering at molecular or atomic level, designing novel electromagnetic properties is largely on optimizing the shape of elements or array geometries of nanostructures, in order to manipulate light-matter interactions. Eventually, the observable electromagnetic field that can be excited and enhanced define the optical properties of the nanostructure or metamaterial of interest.

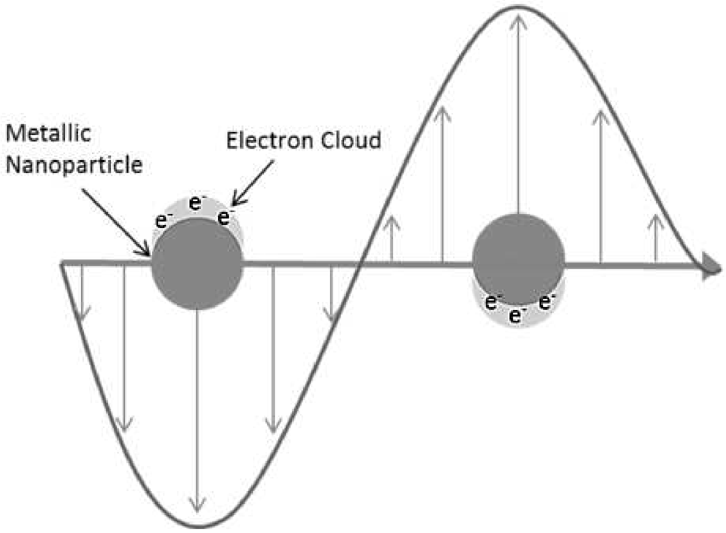

Figure 1·1: Interaction between light and metal nanoparticle through induced oscillation of electrons by electric field component of light.

1.1 Photonic-plasmonic nanostructures and metamaterials

Light interacts with ordinary materials through electromagnetic interaction, and a simple model for the dielectric properties of a material can be obtained by considering the motion of bound electron in the presence of an applied electric field. As shown in Fig. 1·1, the simplest example is the interaction between metal nanoparticle's electrons with the electric field component of light. As the electric field of light oscillates, the electrons in the metallic nanoparticle also oscillates with the same frequency, in analogy to the response of a spring by an external mechanical force.

With this analogy in mind, a simple model for the dynamics of the displacement $x(t)$ (as a function of time t) of the bound electron in the atoms of a nanoparticle can be expressed as:

$$\frac{d^2x}{dt^2} + \gamma\frac{dx}{dt} + \omega_0^2 x = \frac{q}{m}\tilde{E}, \tag{1.1}$$

where $\omega_0^2 x$ is a spring-like restoring force due to binding of electrons to atom's nucleus, based on the resonance frequency ω_0 of the atomic spring; the term $\gamma\frac{dx}{dt}$ is analogous to damping of mechanical oscillation due to friction; q is the charge; m is the mass of electron; and $\tilde{E}$ is a time-dependent sinusoidal electric field $\tilde{E} = Ee^{-i\omega t}$.

As a result, one can solve Eq. 1.1 and obtain the displacement as:

$$x = \frac{\frac{qE}{m}}{\omega_0^2 - \omega^2 + i\gamma\omega}, \tag{1.2}$$

From perspective of material's optical properties, the polarization per unit volume P (Jackson, 1999) can be expressed as:

$$P = Nqx = \frac{\frac{Nq^2}{m}}{\omega_0^2 - \omega^2 + i\gamma\omega}E = \epsilon_0 \chi E, \tag{1.3}$$

where χ is the frequency-dependent electric susceptibility, ϵ_0 is the free-space dielectric permittivity, N is the number of electrons.

Similarly, the electric displacement field D (Jackson, 1999) can be expressed as:

$$D = \epsilon_0 E + P = \epsilon_0 \epsilon_r E, \tag{1.4}$$

where ϵ_r is the relative dielectric permittivity of material, and the refractive index, n, for material in the visible is typically defined as $n = \sqrt{\epsilon_r}$. (This often valid because the relative magnetic permeability of ordinary optical materials is $\mu_r \simeq 1$.) As a result, we can obtain from microscopic interactions between light and matter the macroscopic optical properties of the material.

However, in nature, the materials available are limited, while the theory of electrodynamics (e.g. Maxwell's equations (Jackson, 1999)) permit far more possibilities for novel optical applications from a theoretical point of view. As a result, methods for engineering materials with unprecedented optical properties is of great importance to modern technology.

One promising paradigm for creating such novel optical materials is through metamaterials. Metamaterials are artificial engineered materials with subwavelength building blocks as a novel approach to manipulate electromagnetic fields. With modern fabrication techniques, bulks of metamaterials can be created in the visible spectrum to realize novel optical phenomena, such as achieving negative refractive index (Figs. 1·2(a),1·2(e), 1·2(g), 1·2(h), and 1·2(j)), optical chirality (Figs. 1·2(b) and (1·2(c))), as well as hyperbolic metamaterials (Fig. 1·2(d)). Enabled by this new class of designed optical materials, we can new engineer device applications such as energy squeezing (Edwards et al., 2008), scattering control (Alu and Engheta, 2008; Alù and Engheta, 2009), optical nonlinear effects (Ciattoni et al., 2010; Ciattoni and Spinozzi, 2012), and imaging (Silveirinha and Engheta, 2009).

Currently, metamaterials with controllable effective material parameters (Zhang and Wu, 2015; Zheludev and Plum, 2016; Menzel et al., 2008; Alu, 2011; Ou et al., 2013) have been studied and developed. However, these examples are largely limited to periodic arrangements, and lack efficient methods for large scale modeling.

From perspective of optical functionalities, numerous works have been also carried out in controlling various properties of light (Fig. 1·3), including the polarization (Li et al., 2015; Gordon et al., 2004; Yu et al., 2009) and direction (Rodrguez-Fortuo et al., 2013; Kosako et al., 2010; Pakizeh, 2012; Liu et al., 2012) control, as well as absorption enhancement (Xiong et al., 2015; Wang et al., 2012; Tan et al., 2013).

In particular, as shown in Fig. 1·3, gratings (Yu et al., 2009) and arrays (Liu et al., 2012) are often used for controlling optical polarization and directivity, while surface morphology (Wang et al., 2012) and cavities (Ou et al., 2013) are engineered to trap light and effectively changing optical properties of the material. From these studies, we can see that most of the structures used are either inspired by antenna theory (Kosako et al., 2010; Novotny and van Hulst, 2011; Bharadwaj et al., 2009) or well-known geometries (Yu et al., 2009; Pakizeh, 2012; Liu et al., 2012; Wang et al.,

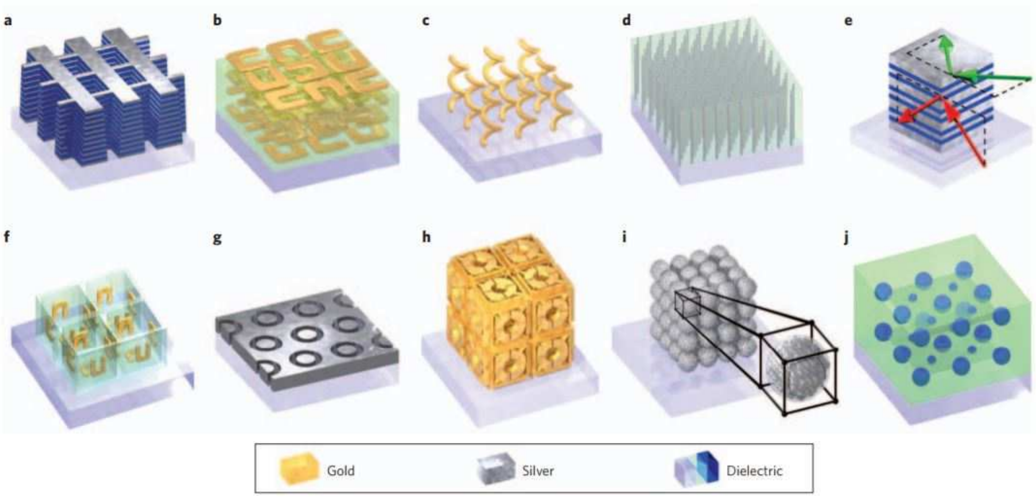

Figure 1·2: (1)Double-fishnet negative-index metamaterial with several layers. (b)Stereo or chiral metamaterial fabricated through stacked electron-beam lithography. (c)Chiral metamaterial made using direct-laser writing and electroplating. (d)Hyperbolic (or indefinite) metamaterial made by electroplating hexagonal-hole-array templates. (e)Metaldielectric layered metamaterial composed of coupled plasmonic waveguides, enabling angle-independent negative n for particular frequencies. (f) SRRs oriented in all three dimensions, fabricated using membrane projection lithography. (g)Wide-angle visible negative-index metamaterial based on a coaxial design. (h)Connected cubic-symmetry negative-index metamaterial structure amenable to direct laser writing. (i)Metal cluster-of-clusters visible-frequency magnetic metamaterial made using large-area self-assembly. (j)All-dielectric negative-index metamaterial composed of two sets of high-refractive-index dielectric spheres arranged on a simple-cubic lattice. (Soukoulis and Wegener, 2011)

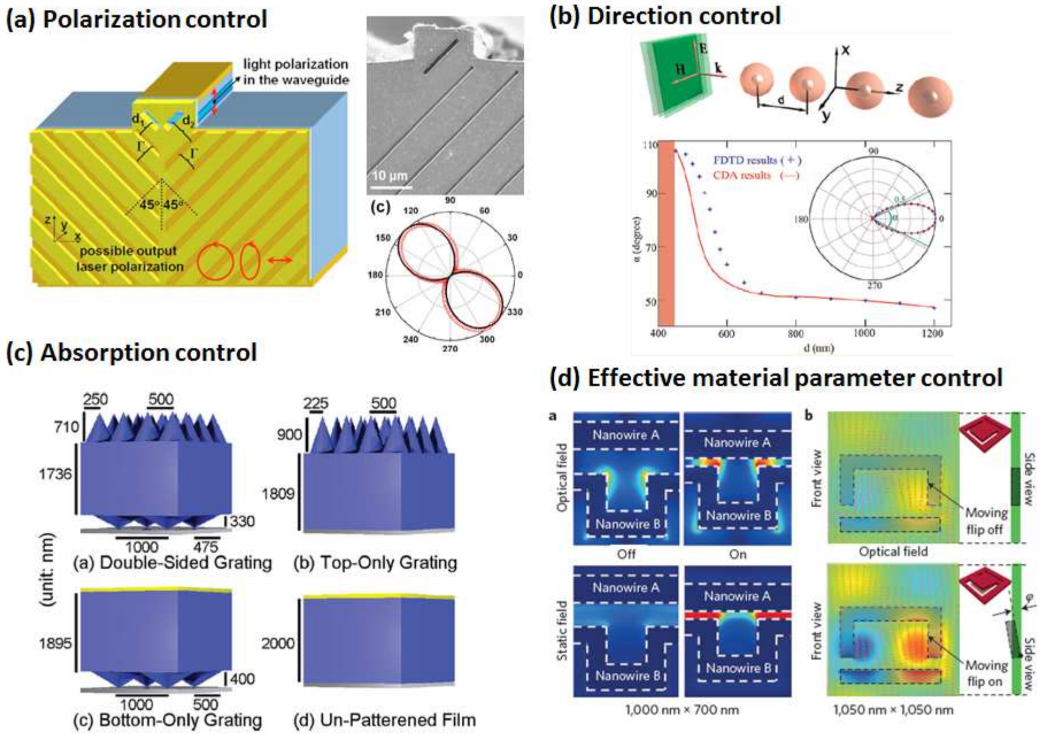

Figure 1·3: (a) Polarization control of semiconductor laser beam through metallic grating and subwavelength aperture (Yu et al., 2009). (b) Broadband unidirectional forward beaming achieved through array of core-shell nanoparticles made with silver core and silicon shell (Liu et al., 2012). (c) Engineering of silicon ultrathin film with grating at both sides to enhance light absorption for solar cell applications (Wang et al., 2012). (d) Dielectric reconfigurable metamaterial changing optical reflectivity and transmission by changing the resonant near-infrared optical field trapped in the structure (Ou et al., 2013).

2012; Tan et al., 2013; Zheludev and Plum, 2016; Ou et al., 2013). As a result, there is a need for rigorous and efficient method to optimize the performance of photonic-plasmonic nanostructures or to engineer the material properties with arbitrary optical properties. Therefore, engineering novel optical properties from direct and inverse designing of complex resonances at both element and array level will be the focus of this thesis.

1.2 Structure of the thesis

As engineering photonic-plasmonic behaviors of nanostructures is largely engineering the resonance of single nanoparticles or collective resonances of the whole nanostructure, I'll divide my works into three categories in this thesis, from engineering the resonances of single nanoparticle element, to engineering collective resonances of nanostructures, and finally to a more rigorous model for understanding collective resonances using the Green's matrix method.

In Chapter 2, I will first review my works on engineering the element of photonic-plasmonic nanostructures. First I briefly review two of my works on designing and understanding the effect of single nanoparticle shapes for indium tin oxide (ITO) disk and gold nanorod. In particular, with the novel ITO plasmonic material developed in my group, I show that micrometer-size ITO disk can be designed to have tunable resonances in the mid-infrared spectral range by simply changing the diameter of the disk. I also show that gold nanorod with two major plasmonic resonance modes can be used to enhance the quantum efficiency of silicon nanocrystals in the vicinity of the gold nanorod. With these examples, where both the geometric shape and resonance nature are simple, it is important to address two questions in designing nanoparticles with optimal optical functionalities. The first question is about the optimal geometric shape of single nanoparticles, and the second is about the nature of resonances. In particular, using surface integral equation coupled with efficient optimization algorithms from the University of Utah, I show an example for optimizing surface field enhancement of plasmonic nanoparticles by parametrizing a general shape using the so-called ”superformula”. On the other hand, using multipolar decomposition of induced electric current involving toroidal multipoles, my work shows how the geometrical shape of an element can be engineered to provide novel optical functionalities with simple dielectric nanodisks and nanopixles. This project investigates the non-radiative mode through employing multipolar decomposition method of current distributions induced by external electromagnetic field inside a nanostructure. Based on the internal field distribution directly calculated using finite-difference time-domain (FDTD) method, I created a routine for computing various multipole moments and their contribution to the far-field radiated power. Because of the new type of multipolar decomposition includes a third family of multipoles, the toroidal multipoles (will be introduced in Chapter 2), non-radiating modes in nanostructures can be analyzed and engineered. Based on the model, we have found that high-index dielectric nanostructures can be used to design non-radiating elements for absorption rate enhancement, which are highly relevant to photodetector and applications based on the trapping of the electromagnetic energy.

The following chapter, Chapter 3, serves as an intermediate step towards array-geometry engineering. I first introduce my collaborative work on broadband electrodes made of gold nanofiber in random arrangement and multiband Cesaro-type fractal plasmonic nanoantennas. In the first case, gold nanofibers, modeled as plasmonic half-shells of different sizes have different resonance peaks, and the overall effect is a broadband resonance. In the second case, fractal plasmonic nanoantennas have well-defined resonance elements at each fractal generation, contributing to an overall collection of discrete peaks in the transmission and reflection spectra. In both works, the nanostructures as a system, i.e. array, of different resonance elements is important for the understanding of the overall optical behavior in each case. Moreover, I also discuss my work on metal nanohelices to show that collective resonance can also be achieved using array of identical elements, and how the geometry of the array affect the collective optical behavior of nanostructures. This work involves designing gold (Au) nanohelices with unprecedented beam forming and polarization control capabilities, through systematically investigating the effect of four geometric parameters of a helix, namely the pitch, radius and number of turns of the helix, as well as the thickness of the wire forming the nanohelix. In this work, we have provided simple design rules for achieving perfect circular polarization in the optical to near infrared spectral range, and discovered quasi-axial modes with prevalent forward beaming capabilities. To a large extent, these optical properties of Au nanohelices can be understood by decomposing a helix into a linear array of identical single-coil helices. The project is carried out mainly with a surface integral equation code based on the method of moments, which will be explained in more detail in Section 2. The results of this project provides the basis for novel applications in sensors, lasers, and optical filters. From the example of gold nanohelices, which points to the emergent resonant behavior through collective resonances at the array level, it becomes clear that understanding array geometry holds the key to engineering more complex optical functionalities in nanostructures and metamaterials. I show in addition an inverse design example on optimizing the array geometry of Vogel spirals made of identical plasmonic nanospheres. In this example, we model the complex array geometry with coupled electric dipoles and show results for optimized cases for absorption and scattering efficiencies. In particular, this project reveals the importance of understanding complex point patterns under the theoretical framework of multiple scattering. Naturally, this leads to understanding how real-space array geometry affects the spectral properties of the vectorial Green's matrix, which is the kernel of the coupled-dipole multiple scattering problem, describing the propagation of electromagnetic waves from the coupled dipolar elements in the array. Therefore, I will use the following chapter, Chapter 4, for a more rigorous and detailed introduction for the method based on understanding vectorial Green's matrix, and apply it to complex aperiodic media.

While individual scattering elements can be designed through varying their geometries to manipulate light-matter interactions, they are limited by the materials available. There is also a difficulty in designing from scratch a geometry or configuration for optimal optical performance. In Chapter 4, I introduce my work on a novel approach that employ Green's matrix and multiple scattering theory to understand and design aperiodic nanostructures and metamaterials. This is potentially a more rigorous and physically intuitive approach, which is also faster compared to numerical methods, such as FDTD and finite elements. In particular, the study of classical and quantum waves in complex and disordered scattering media using Green's matrix unveiled fascinating capability of the method, and provided predictive understanding to phenomena such as Anderson localization (Lagendijk et al., 2009). To our knowledge, all existing theories of such kind deal with random systems, while we believe that the same set of equations should equally be applicable to aperiodic systems of scatterers. In this thesis, I present my works using the Green's matrix approach to study aperiodic arrays and compare them with known results of random systems. In particular, I use work on complex-prime-based arrays, and one-dimensional aperiodic systems, to show the relevance of the Green's matrix method in designing complex nanostructures and topological metamaterials. Interestingly, in one-dimensional systems, I show that Green's matrix is also useful for the theoretical study of photonic topological edgestates that exist in energy bandgaps. At the end of the chapter, I discuss extension of the existing Green's matrix method to include magnetic dipoles, which is important to many applications that need understanding of both effective electric and magnetic behavior of the nanostructures, especially for high-index dielectrics.

Finally, I will conclude my thesis in Chapter 5, and provide a brief outlook on potential directions for future works. My developed codes for simulation and analysis will be in the appendices.

Chapter 2

Engineering Individual Resonances Through Shapes of Nano-elements

Understanding and engineering single-element resonance through designed shapes of nanoparticles can be useful for many applications, including biosensing and bioimaging applications. I divide my work relevant to this chapter into three parts. I divide the first section into two examples and first introduce my work in collaboration with Dr. Yu Wang and Prof. Nanfang Yu's group at Columbia University on resonance tunability of engineered indium tin oxide (ITO) plasmonic disks at mid-infrared (MIR) spectral range (Wang et al., 2017). In this example, novel plasmonic material, ITO, provide possibility of achieving plasmonic resonance with low losses at MIR spectral range. Given this material platform, my work shows how the geometry affect single-element resonances through changing the size of ITO disks. I then show my work providing numerical and simulation understanding to the experiments by Dr. Hiroshi Sugimoto and Prof. B. M. Reinhard's group at Boston University on emission-rate enhancement of silicon nanocrystals with gold nanorod (Sugimoto et al., 2015). In this case, single-element resonance of gold nanorods changes the environment of silicon nanocrystals and improve the quantum efficiency of the system. In both examples, the resonances providing useful applications are due to plasmonic resonances of simple geometries. Relevant sections from published results of both works have been modified and included (Wang et al., 2017; Sugimoto et al., 2015).

While simple geometries can often provide satisfactory optical performances, such as surface field enhancement, there is a lack of theoretical justification of restricting to ordinary geometrical shapes for engineering single-element resonances. In addition, the nature of such resonances may vary from electric to magnetic, and even toroidal (Zel'dovich, 1957; Dubovik and Tugushev, 1990; Nanz, 2016; Miroshnichenko et al., 2015). I devote the next two sections to separately address these two problems.

In the second section, in order to answer the question on optimal geometry of a resonant single-element, I use my work on a novel method for optimizing surface field enhancement as an example. Through parameterizing a general smooth three-dimensional shape based on superformula, my collaborator find optimal solutions that are beyond conventional geometrical shapes. Relevant materials are extracted and modified from the published results from this collaborated work with by Prof. Carlo Foresteire and Prof. Robert M. Kirby's group at University of Utah (Forestiere et al., 2016).

Finally, In the third section, I focus on my work using multipolar decomposition to understand scattering properties of high-index dielectric nanodisks and nanopixels. In particular, using the novel decomposition method involving toroidal multipoles, I show that we can better understand scattering minima through cancellation between electric and toroidal dipoles, and engineer anapole modes for enhanced absorption. Relevant parts of my published work on this topic is modified and included in this thesis (Wang and Dal Negro, 2016).

2.1 Engineering resonance of single elements

In this section, I first introduce my work related to designing single-element resonances using the example of ITO disks (Wang et al., 2017), and then show how single-element resonance can be useful through the example of quantum efficiency enhancement by nanorod (Sugimoto et al., 2015).

2.1.1 Engineering of resonant materials for plasmonics applications

Traditional plasmonic materials such as noble metals (e.g. gold, silver, and aluminum), have been widely used in plasmonic devices and applications, but suffer high extinction losses in the visible and infrared spectra. In addition, most of these conventional plasmonic metals are neither CMOS-compatible nor tunable, limiting their application and integration with silicon-based technologies. In recent years, transparent conductive oxides (TCOs) have emerged as novel alternatives to these traditional plasmonic materials. These TCOs have the advantages including CMOS compatibility, low losses, and tunability. A particular example of the TCOs my group has been actively using in our researches is the group of indium tin oxide materials, whose dielectric permittivity can be described by the Drude-Sommerfeld model (Kim et al., 2013):

$$\epsilon(\omega) = \epsilon_\infty - \frac{\omega_p^2}{\omega^2 + i\Gamma\omega}, \tag{2.1}$$

where ϵ_∞ is the high frequency limit of the frequency(ω)-dependent $\epsilon(\omega)$, ω_p is the plasma frequency, and Γ is the charge carrier collision rate. Recently, my group has fabricated as variety of ITO materials and well as disks of ITO materials showing tunability of their plasmonic resonances in the mid-infrared range (Wang et al., 2017).

In particular, in order to demonstrate the shift in the resonances of designed ITO disks, simulations based on the finite-difference time-domain (FDTD) method is used to calculate reflectance spectra of micro-disc arrays. The intensity of the reflected infrared light is computed under normal incidence condition. In Fig. 2·1(a), I present calculated reflectance spectra with FDTD for ITO disks with diameters ranging from $1\mu m$ up to $5\mu m$. In Fig. 2·1(b), measured FTIR spectra by Prof.

Nanfang Yu's group at Columbia using Dr. Yu Wang's fabricated samples are shown. The results clearly indicate the excitation of a size-dependent plasmon resonance in the ITO disks, with a shift of the plasmonic resonance peak that follows the theoretical predictions. In particular, as the diameter of the ITO disks increases, the reflectance spectral peak shifts to longer wavelengths. However, the simulation results for ITO disks with diameters of $4\mu m$ and $5\mu m$ feature a larger peak shift and a broader spectrum compared to the experimental results. These differences are attributed to fabrication imperfections (residual ITO that covers the CaF2 substrates, over-etching in the regions that are between adjacent four micro-discs). Furthermore, we notice that the small dips in the calculated reflectance spectra (Fig. 2·1(a)) of disks with diameters of $4\mu m$ and $5\mu m$ correspond to the excitation of grating resonances in a perfectly periodic structure (FDTD simulations were conducted using periodic boundary conditions), and cannot be expected in the fabricated finite-size samples.

In Fig. 2·1(c) and 2·1(d) we show two representative electric-field distributions across the middle height of the disks at the peak of the simulated reflectance spectra (Fig. 2·1(a)): $\lambda = 6.1\mu m$ for ITO disks with $1\mu m$ diameter and $\lambda = 12.0\mu m$ for ITO discs with $5\mu m$ diameter. At $\lambda = 6.1\mu m$, the field distribution is predominantly due to a dipolar response induced at a wavelength significantly larger than the disk size. Compared to the distribution in Fig. 2·1(d), there is more field inside the disks in Fig. 2·1(c) due to the smaller value of the imaginary part of ITO permittivity, which makes ITO at this wavelength behave as a non-ideal metal. In contrast, as shown in Fig. 2·1(d), a dipolar field distribution is induced at the edges of the $5\mu m$ disk at the peak wavelength of reflectance ($\lambda = 12.0\mu m$) where a much larger imaginary part of the ITO permittivity makes the ITO material more metallic in nature. These findings demonstrate that ITO thin films with engineered dispersion support strongly confined plasmonic modes and are ideally suited for the fabrication

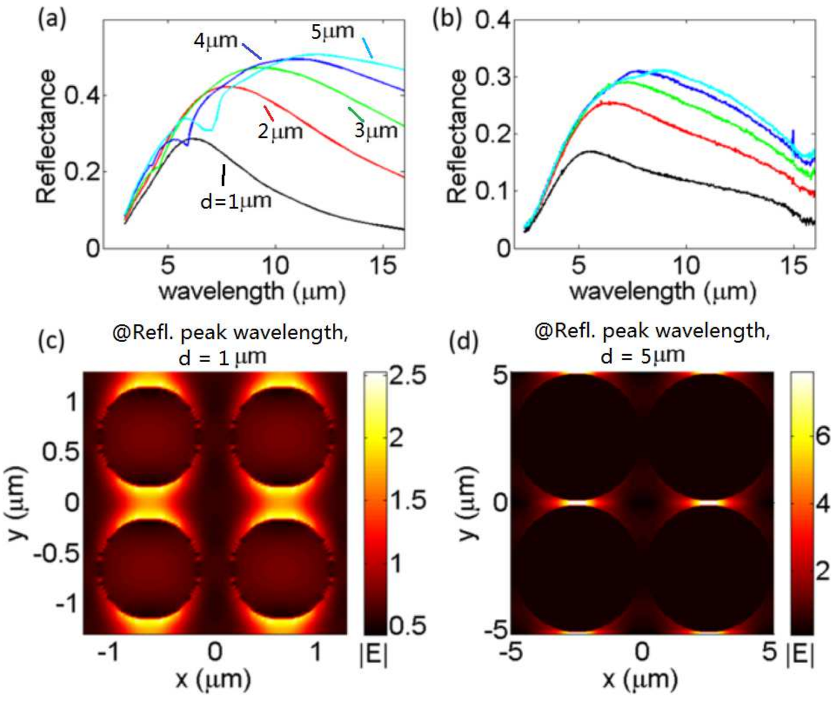

Figure 2·1: (a) FDTD simulations of the reflectance spectra of ITO disk arrays as a function of disk diameter: $1\mu m$ (black), $2\mu m$ (red), $3\mu m$ (green), $4\mu m$ (blue), $5\mu m$ (cyan). All ITO discs have a height of 280nm. (b) Measured reflectance spectra of ITO disk arrays patterned on CaF2 substrates with different disk diameters: $1\mu m$ (black), $2\mu m$ (red), $3\mu m$ (green), $4\mu m$ (blue), $5\mu m$ (cyan). (c) and (d) are field distributions inside and around the $1\mu m$ and $5\mu m$ ITO disks at $\lambda = 6.1\mu m$ and $12.0\mu m$, respectively (peaks of reflectance spectra). (Wang et al., 2017) of plasmonic structures with largely tunable spectral resonances across the mid-IR range.

As a summary, the simulation results have demonstrated good agreement with experimental measurements, and show that the plasmonic resonance of single ITO disks (enhanced through nearfield coupling with neighboring particles) of changing sizes contribute to the shift of resonances in the measured reflectance spectra.

2.1.2 Plasmon-enhanced emission rate of silicon nanocrystals in gold nanorod composites

In addition to the cylindrical disk geometries shown in the above example, plasmonic nanostructures such as nanospheres, and nanorods have also been tailored for various device applications. In the following, I show my work using gold nanorod of specific size for controlling the emission properties of organic dyes and semiconductor nanocrystals (NCs) (Pompa et al., 2006; Kinkhabwala et al., 2009). Significant light emission enhancement has been previously demonstrated utilizing the enhanced local field originating from localized surface plasmon resonance (LSPR) of metal nanostructures. The combination of plasmonic nanoparticles and nanoscale emitters into a single multifunctional colloidal platform has a large potential for the engineering of novel active devices for biosensing and bioimaging (Jin and Gao, 2014; Ayala-Orozco et al., 2014; Yao et al., 2014).

The enhancement of spontaneous emission rate is explained by the enhancement of local density of states (LDOS) due to the LSPR of Au nanorods. To discuss the contribution of the radiative and nonradiative rates as well as the quantum efficiency of Si NCs-decorated Au nanorods, I performed theoretical calculations using the MNPBEM code (Hohenester, 2012) which is based on the rigorous boundary element method. The decay rates in the vicinity of a Au nanorod with a diameter of $60nm$ and a length of $126nm$ have been simulated by placing point dipoles at fixed distances from the nanorod surface with tabulated dispersion data (Johnson and Christy, 1972). The geometrical parameters are estimated from measured nanoparticle sizes. The results are normalized by the emission rate of a dipole in water, and thus we use the term radiative and nonradiative rate enhancements to describe the modification of decay rate due to the presence of a Au nanorod. In Fig. 2·2(a), I demonstrate a good agreement between the extinction spectra for Au nanorods obtained from experiment and the simulation. Figure 2·2(b) shows both radiative and nonradiative rate enhancements of a single dipole placed $10nm$ from the top and side of a Au nanorod as a function of wavelength. The results are averaged over all dipole orientations. The largest enhancement of radiative rate is observed when the dipole is placed at the top of the nanorods. In contrast, when the dipole is positioned along the side of the nanorods, its radiative rate is small and comparable to the nonradiative rate at $750nm$. It is also worth noting that the radiative and nonradiative rate enhancement values, which determine the overall quantum efficiency of the plasmonic-coupled system,(Novotny and van Hulst, 2011; Busson et al., 2012) strongly depend on the orientation of the dipoles. To discuss the quantum efficiency of the dipoles with different orientations, we compare the ratio of radiative to total decay rate enhancement, called the antenna efficiency (Novotny and van Hulst, 2011; Busson et al., 2012). In Fig. 2·2(c), we plot the results of a dipole oriented parallel (solid) and perpendicular (dashed) to the major axis of the nanorods. For dipoles placed at the side of the nanorod (black curves), the efficiency is comparable for both orientations. On the other hand, we find a dramatic change in the efficiency when a dipole at the top is oriented parallel to the major axis of the nanorod. This explains our experimental results of emission polarization in Figure 4f of (Sugimoto et al., 2015). In the case of NCs attached at the top of the nanorod, the PL intensity becomes much larger when the analyzer is positioned parallel to the major axis of the nanorods. The polarization-selective PL enhancement may improve the sensitivity and performance of bioimaging.

In our samples, NCs are randomly located on the surface of the Au nanorod. Therefore, we also took into account the relative effect of dipole positions around the nanorod and obtained the positionally averaged decay rates shown in Fig. 2·2(c). We notice that around the emission peak of NCs-750, the radiative rate enhancement is about 2 times larger than the nonradiative rate enhancement. Therefore, in nanocomposite of NCAu nanorods, a significant quantum efficiency enhancement of the NCs can be obtained. The nonradiative decay becomes dominant at wavelengths shorter than $650nm$, which corresponds to the excitation region of the transverse scattering mode of the nanorods.

In order to provide an quantitative estimate of the quantum efficiency enhancement, results from both experiments and simulations are combined. We focus on the NCs-750 sample because the PL spectrum of NCs-750 fully overlaps with the LSPR of Au nanorods. The intrinsic quantum efficiency (Q_0) of Si NCs is expressed as $Q_0 = \gamma_r^0/(\gamma_r^0 + \gamma_{nr}^0)$, where γ_r^0 and γ_{nr}^0 are intrinsic radiative and nonradiative decay rates of NCs in the aqueous solution, respectively. On the other hand, the quantum efficiency of NCs-coupled Au nanorods (Q_m) is defined by:

$$Q_m = \frac{\Gamma_r}{\Gamma_r + \Gamma_{abs} + \gamma_{nr}^0}, \tag{2.2}$$

where Γ_r is the modified radiative rate, Γ_r/γ_r^0 is the Purcell factor (Purcell, 1946; Akselrod et al., 2014; Lu et al., 2014) with respect to the emission of a dipole in water, and Γ_{abs} is the plasmon-induced nonradiative rate due to the absorption by the metallic nanorods. In Eq. 2.2, we assume that only the radiative rate is modified by the coupling with Au nanorods because the intrinsic nonradiative rate (γ_{nr}^0)) arising from material imperfections of Si NCs is not affected by the local electromagnetic environment (Govorov et al., 2006; Bharadwaj et al., 2007). In fact, the decay rate

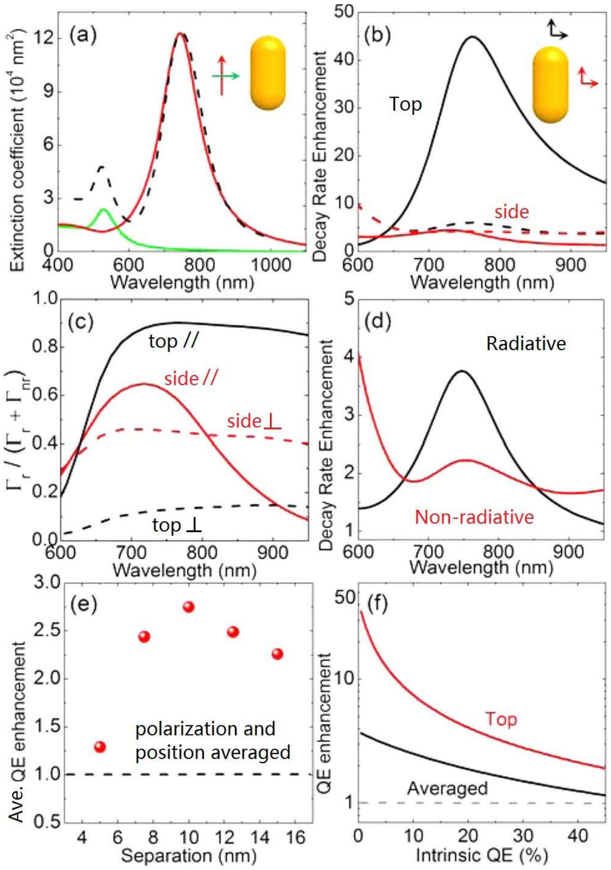

Figure 2·2: (a) Calculated extinction coefficient (solid line) of a Au nanorod excited by plane waves with two different polarizations (red and green curves) and measured extinction spectrum (dashed line). (b) Calculated radiative (solid line) and nonradiative (dashed line) decay rate enhancements of a dipole placed $10nm$ from the top (black) and side (red) of a Au nanorod. The results are normalized by the radiative rate of the dipole in water and orientationally averaged. (c) Ratio between radiative and total decay rate enhancement of dipoles oriented parallel (solid) and perpendicular (dashed) to the long axis of the nanorods. Black and red curves represent the results of dipoles placed $10nm$ from the top and side of the nanorods, respectively. (d) Both position- and orientation-averaged radiative (black) and nonradiative (red) decay rate enhancements. (e) Quantum efficiency enhancement as a function of separation between emitters and nanorods. (f) Quantum efficiency enhancements as a function of intrinsic quantum efficiency. Black and red curves represent positon-averaged results and the case of a dipole placed at the top of the nanorod, respectively. (Sugimoto et al., 2015) is almost unity at wavelengths that are detuned from the resonance of Au nanorods. This confirms that the measured decay rate enhancement is due to Γ_r/γ_r^0 (Purcell enhancement) and Γ_{abs}/γ_r^0 (absorption by Au nanorods) rather than modification of the internal nonradiative rate of Si NCs by coupling with nanorods.

By combining the experimentally obtained total decay rate enhancement (W_{total}) with Γ_r/γ_r^0 and Γ_{abs}/γ_r^0 values calculated from simulations in Fig. 2·2(c), Q_m, Q_0 as well as the enhancement of quantum efficiency of Si NCs can be calculated. In particular, with measured $W_{total} = 1.35$ at $\lambda = 750nm$ (the emission peak of NCs), and simulation values $\Gamma_r/\gamma_r^0 = 3.77$ and $\Gamma_{abs}/\gamma_r^0 = 2.23$, we get $Q_0 = 7.4\%$. The quantum efficiency enhancement is calculated to be 2.8, which is achieved only by engineering the radiative decay rate without the contribution from excitation enhancement (pumping enhancement).

Finally, it is necessary to discuss the perspective of the NC-Au nanorod composite. In this system, there are two determining factors for radiative rate enhancement, which are the NC location on the nanorod and their separation distance from the nanorod. In Fig. 2·2(e), we plot the quantum efficiency enhancement that can be obtained considering the emission of NCs with $Q_0 = 7.4\%$ (at $750nm$) as a function of their separation from the surface of a nanorod. The NC orientation and location around the surface of the nanorod have been averaged. We found that there exists an optimal separation distance in the range of 7.5 to $12.5nm$, which is very similar to the conditions of our samples. Figure 2·2(f) shows the quantum efficiency enhancement factors as a function of the intrinsic quantum efficiency of NCs. We plot both dipole position-averaged values as well as the case of a single dipole located at the top of the nanorod. From the curves of the position-averaged result, we demonstrate quantum efficiency enhancement in a wide range of values for the intrinsic quantum efficiency. This means that even in the case of emitters with significantly larger values of intrinsic quantum efficiency, the proposed plasmonic-coupled composites give rise to emission enhancement, especially when the emitters are located atop the nanorods. The selective binding of active molecules on top of nanorods has been already reported (Caswell et al., 2003; Fu et al., 2010; Chang et al., 2005). Although this work has been limited to Si NCs with low intrinsic quantum efficiency, the results of our numerical analysis demonstrate the applicability of the nanorod composite approach to other emitting materials that feature larger values of intrinsic quantum efficiency.

2.2 Inverse engineering of metal nanoparticles' shapes

In the previous two examples, conventional geometric shapes have been used for controlling the resonances at single-element level. However, ordinary geometrical shapes limit the space of engineerability of resonances at the single-particle level, and are not likely to be the optimal design for desired optical properties. In order to address this problem of optimal geometry, the inverse design of nanostructure geometries is needed. However, currently, difficulty of dealing with a large number of degrees of freedom prevents wide adoption of inverse designs in solving rigorous electromagnetic problems. Here, I show my work in collaboration with Prof. Carlo Foretiere, who's a former member of our group, and Prof. Kirby's group at the University of Utah (Forestiere et al., 2016). In this work, a new method is proposed for rigorous inverse design of the shape of metal nanoparticles, with the aim for maximizing surface field enhancement. In particular, in order to parameterize the geometric shape of a single nanoparticle, and reduce the number of degrees of freedom, Gielis' superformula in three dimension is used (Gielis, 2003).

2.2.1 The superformula

In order to parameterize the shape of a single nanoparticle, we describe the closed surface Σ of the metal nanoparticle by using a simple and general equation, the superformula introduced by J. Gielis introduced about a decade ago (Gielis, 2003). The superformula has been proved to be extremely effective to describe a variety of forms and patterns occurring in nature, including cells, tissues, stems, flowers, shells, starfish, galaxies, and DNA molecules (Gielis et al., 2005). It was first introduced in Plasmonics by Rodrig uez-Oliveros and San chez- Gil to describe the shape of 3D plasmonic nanoparticles (Rodríguez-Oliveros and Sánchez-Gil, 2011) and, in its 2D form, was also used for the inverse design of translational-invariant plasmonic cylinders (Tassadit et al., 2011; Macías et al., 2012). The Gielis superformula in three dimensions has the mathematical expression:

$$\begin{aligned} x &= \eta r_1(\phi)\cos(\phi) r_2(\theta)\cos(\theta), \\ y &= \eta r_1(\phi)\sin(\phi) r_2(\theta)\cos(\theta), \\ z &= \eta r_2(\theta)\sin(\theta), \end{aligned} \tag{2.3}$$

where

$$\begin{aligned} r_1(\phi) &= [|\frac{\cos(\frac{m^{(\phi)}}{4}\phi)}{a^{(\phi)}}|^{n_2^{(\phi)}} + |\frac{\sin(\frac{m^{(\phi)}}{4}\phi)}{b^{(\phi)}}|^{n_3^{(\phi)}}]^{-\frac{1}{n_1^{(\phi)}}}, \\ r_2(\theta) &= [|\frac{\cos(\frac{m^{(\theta)}}{4}\theta)}{a^{(\theta)}}|^{n_2^{(\theta)}} + |\frac{\sin(\frac{m^{(\theta)}}{4}\theta)}{b^{(\theta)}}|^{n_3^{(\theta)}}]^{-\frac{1}{n_1^{(\theta)}}}, \end{aligned} \tag{2.4}$$

and $\theta \in [\pi/2, \pi/2]$, $\phi \in [\pi, \pi]$. From Eqs. 2.3 and 2.3 it is apparent that the superformula can be completely described by 13 parameters, six of them, that is, $m^{(\phi)}$, $n_1^{(\phi)}$, $n_2^{(\phi)}$, $n_3^{(\phi)}$, $a^{(\phi)}$, and $b^{(\phi)}$ modulate the shape along the azimuthal angle ϕ, while the parameters $m^{(\theta)}$, $n_1^{(\theta)}$, $n_2^{(\theta)}$, $n_3^{(\theta)}$, $a^{(\theta)}$, and $b^{(\theta)}$ control the variation of the shape along the altitude angle θ (zenith). The remaining parameter η controls the scaling of the resulting shape. However, being interested in shapes compatible with planar nanofabrication technology we keep fixed the altitude parameters:

$$\begin{aligned} m^{(\theta)} &= 2; \\ n_i^{(\theta)} &= 2(i = 1, 2, 3); \\ a^{(\theta)} &= b^{(\theta)} = 1 \end{aligned} \tag{2.5}$$

Moreover, in order to exclude from the optimization space shapes with extremely sharp edges we impose the following constraints on the azimuthal parameters:

$$\begin{aligned} 1 &\leq m^{(\phi)} \leq 8; \\ 0.75 &\leq n_i^{(\phi)} \leq 6(i = 1, 2, 3); \\ 0.25 &\leq a^{(\phi)} \leq 2; \\ 0.25 &\leq b^{(\phi)} \leq 2. \end{aligned}$$

Finally, in order to avoid excessively small or large particles we also set constraints on the scaling factor η:

$$25nm \leq \eta \leq 75nm. \tag{2.6}$$

As a result, we have reduced the inverse problem of designing the nanoparticle shape to a constrained optimization with respect to only seven parameters.

2.2.2 Direct electromagnetic problem and surface integral equation method

In order to perform the inverse design, a solver of the direct electromagnetic problem is required. The desired solver should be at the same time fast, because it has to be executed a large number of times in a standard global optimization algorithm, yet accurate. The latter requirement is particularly compelling since we are interested in the accurate evaluation of electric field in the near-zone of a plasmonic particle, which is usually not easy to achieve if compared to any far-field quantity (Forestiere et al., 2012). For this case, the FDTD method, although widely used in the analysis of plasmonic structures, appears to be inadequate when high accuracy required (Hoffmann et al., 2009; Smajic et al., 2009). The FDTD method, with a regular square grid, not only poorly approximates arbitrary boundaries, but also suffers from staircasing effects, which drastically reduce its numerical accuracy (Smajic et al., 2009). In addition, the poor performances of FDTD are exacerbated when strong field localization is present (Hoffmann et al., 2009). On the contrary, formulations based on electromagnetic surface integral equations (SIE) (Harrington and Harrington, 1996) are particularly efficient because they only require a surface discretization without sacrificing the near-field accuracy. As a result, we reformulated the electromagnetic problem given as in terms of Surface Integral Equations (SIE). In particular, we use i and e to denote the domains inside the nanoparticle, Ω^i, or outside Ω^e. The scattered fields in each domain satisfy:

$$\begin{aligned} \nabla \times \mathbf{E}_S^{(t)} &= -j\omega\mu_0 \mathbf{H}_S^{(t)}, \\ \nabla \times \mathbf{H}_S^{(t)} &= j\omega\epsilon_t \mathbf{E}_S^{(t)}, \end{aligned} \tag{2.7}$$

where $\mathbf{E}_S$ and $\mathbf{H}_S$ are scattered electric and magnetic fields respectively, and $t = i, e$. In addition, the fields on the surface Σ separating the two domains satisfy:

$$\begin{aligned} \mathbf{n} \times (\mathbf{H}_S^e - \mathbf{H}_S^i) &= -\mathbf{n} \times \mathbf{H}_0, \\ \mathbf{n} \times (\mathbf{E}_S^e - \mathbf{E}_S^i) &= -\mathbf{n} \times \mathbf{E}_0, \end{aligned} \tag{2.8}$$

where $\mathbf{n}$ is the outward normal to the surface Σ, $\mathbf{E}_0$ and $\mathbf{H}_0$ are electric and magnetic fields of external excitations, respectively. For this particular problem, we used the JMCFIE formulation (Yla-Oijala and Taskinen, 2005), and numerically solved this formulation using the Method of Moments (MoM) with the Rao-Wilton-Glisson (RWG) basis functions (Rao et al., 1982). We also managed the weak singularities with the techniques described in ref (Graglia, 1993). A detailed analysis of the accuracy of the local fields in proximity of metal nanoparticles calculated by the JMCFIE formulation can be found in ref (Forestiere et al., 2012).

2.2.3 Optimization and results

In this work, we measure the performance of a metal nanoparticle in terms of the averaged electric-field enhancement on the surface Σ, namely:

$$g(\lambda) = \frac{1}{|\Sigma|} \int\int_{\Sigma} |\frac{\mathbf{E}^{(e)}}{\mathbf{E}_0}| dS, \tag{2.9}$$

where $\mathbf{E}^{(e)}$ is the electric field on the external surface of the nanoparticle and $\mathbf{E}_0$ is the incident electric field.

The averaged field enhancement g is a time-consuming quantity to evaluate accurately even using the SIE solver. Unfortunately, many standard global optimization algorithms, including genetic algorithms, particle-swarm optimization or simulated annealing are designed for objective functions that are inexpensive to evaluate (Pinter, 2002). Therefore, we need an efficient algorithm that requires less objective function evaluations, and that carefully chooses where to evaluate it to maximize the information gained at every step. In particular, the collaborating group at Utah used the Efficient Global Optimization (EGO), which is a global optimization algorithm based on response surface surrogates that satisfy both requirements (Jones et al., 1998; Adams et al., 2016). The procedure of the EGO algorithm follows the steps summarized in the flowchart shown in Fig. 2·3. First, we construct a tentative Gaussian process (GP) model of the objective function g defined in Eq. 2.9, that will be refined during the subsequent iterative process. The GP is a model that closely mimics the behavior of the average electric field enhancement g as a function of the superformula parameters, being able to provide an estimate of the value of g and the corresponding uncertainty with a reduced computational burden. We build it based on a set of $N = 36$ sample points, called training points, belonging to the search space spanned by the superformula parameters and on the corresponding real values of g evaluated by the direct SIE solver. Then, we start the iterative process. At each iteration, we maximize a quantity called Expected Improvement Function (EIF), using a deterministic global optimization algorithm. The function EIF is defined as the expectation that any point in the search space will improve the current optimal solution, and it is estimated based on the expected values of g and of the corresponding uncertainties obtained by the GP model (Adams et al., 2016). Thus, we choose the point at which the EIF is maximized as an additional training point for the GP. Therefore, EGO balances between exploring areas of the search space where good solutions have been found and area where the uncertainty is high to refine the GP model. When the value of EIF is sufficiently small, the iteration process is stopped. We employ the software DAKOTA (Adams et al., 2016) developed at Sandia National Laboratories to implement EGO.

I now present the results of the inverse design of silver (Ag) nanoparticle within the spectral range $[200, 500] nm$. We used the Ag permittivity obtained by interpolating the experimental data of Johnson and Christy (Johnson and Christy, 1972). The parameters of the superformula defining the optimal scatterer obtained by the EGO method are listed in Table 3 for several wavelengths; the corresponding $|E|-$field distributions on Σ are shown in Fig. 2·4(a). Additionally, in Fig. 2·4(b), we plot the achieved optimal values of g as a function of the optimization wavelength λ. In Fig. 2·4(c), we show the g spectrum of the found optimal shapes as a function of the inci-

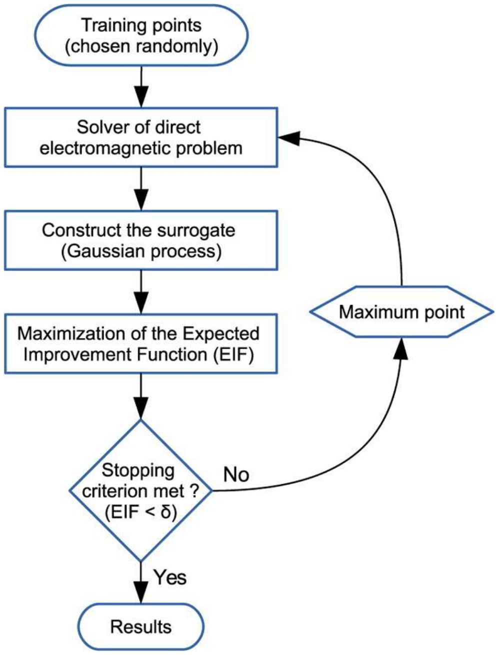

Figure 2·3: Flowchart of the EGO algorithm scheme for the solution of inverse design problems. (Forestiere et al., 2016)

dent wavelength. At the deep-ultraviolet wavelengths, $\lambda = 250$ and $300nm$, the optimal shapes resulting from the optimization process are approximatively nanospheres, as shown in the subpanels of Fig. 2·4(a) labeled with a red square and a blue circle, respectively. Unfortunately, at these wavelengths the silver does not exhibit good plasmonic properties and this is reflected in modest values of g, namely, 1.6 and 1.4, respectively. In facts, we are in the tail of the plasmonic resonant curve, as apparent if we examine the corresponding g spectra shown with red and blue curves in Fig. 2·4(c). Increasing the wavelength to 350 nm the optimal shape is the nanorod identified with a green triangle in Fig. 2·4(a), which features a much higher value of g, that is 10. At $375nm$ the inverse design algorithm returns approximately a prolate spheroids with $g = 19$, identified in Fig. 2·4(a) with a cyan diamond. Then, the objective function reaches its peak at $\lambda = 400nm$, where the nanorod labeled with a magenta star exhibits $g = 22$, which is the highest value that we are able to achieve for Ag, as shown in Fig. 2·4(b), and only slightly surpasses the maximum value obtained for gold. Finally, at 450nm, the tetrapod identified with a yellow inverted triangle in Fig. 2·4(a) maximizes the value of g. Moreover, it is apparent that the g spectra of the optimal shapes, shown in Fig. 2·4(c), feature their peak values at the prescribed optimization wavelength, in all but the first two cases. This fact corroborates the EGO efficacy for the design of Ag nanoparticles. It is worth noting that the scale factor η of the optimized particles, shown in Table 2.1, assumes in most of the investigated scenarios the minimum allowed value prescribed by the assigned constraint of Eqs. 2.6. This fact suggests that by relaxing the lower bound of η we may obtain different optimal shapes with higher value of g. However, this will results in particles too small to be fabricated with the current technology, and therefore outside the scope of this study.

Table 2.1: Superformula Parameters Describing the Inverse-Designed Ag Nanoparticles with Optimal g (Forestiere et al., 2016).

$\lambda(nm)$	$m^{(\phi)}$	$n_1^{(\phi)}$	$n_2^{(\phi)}$	$n_3^{(\phi)}$	$a^{(\phi)}$	$b^{(\phi)}$	$\eta(nm)$	g
200	1.01	4.43	4.26	2.00	0.50	0.73	25.0	1.6
250	1.01	4.04	4.26	5.43	0.82	0.70	25.0	1.6
300	3.32	2.50	3.68	0.76	0.72	0.51	32.7	1.4
325	3.32	0.93	4.26	1.34	0.50	0.50	25.0	1.8
350	1.01	3.66	4.26	1.90	0.50	0.50	25.0	10
375	3.80	4.43	0.76	3.76	0.50	0.50	25.0	19
400	4.38	5.71	0.89	6.00	1.39	0.50	25.0	22
450	7.58	6.00	3.68	3.27	0.52	2.00	26.0	16

As a summary, with the sample of integrating SIE with chosen optimization algorithms, I have shown that it is possible to address the issue of finding the optimal geometric shape for single nanoparticle resonance through inverse design. In the next section, I show the nature of each resonances can be understood through the multipolar decomposition of induced currents, and demonstrate how nonradiating modes can be engineered inside a single nanoparticle.

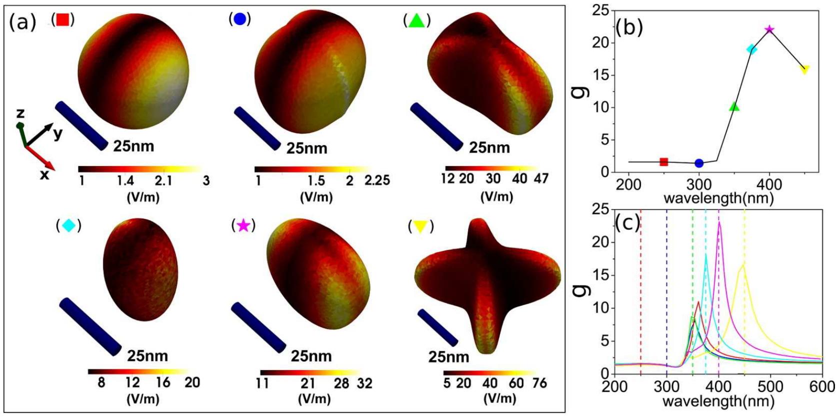

Figure 2·4: (a) Inverse-designed Ag nanoparticles and corresponding |**E**| distribution (V/m, linear scale) on Σ. The particles are excited by a xpolarized plane wave of unit electric field magnitude (1 V/m), propagating along the z-axis at wavelength (red square) 250 nm, (blue circle) 300 nm, (green triangle) 350 nm, (cyan diamond) 375 nm, (magenta star) 400 nm, (yellow inverted triangle) 450 nm. All scale bars correspond to 25 nm. (b) Optimimum value of g as a function of the incident wavelength. (c) g spectra calculated for the optimal shapes as a function of the incident wavelength; each curve corresponds to the particle of panel (a) labeled by the symbol of corresponding color. (Forestiere et al., 2016)

2.3 Engineering non-radiative anapole sources for broadband absorption enhancement in dielectric nanostructures

Non-radiating sources are charge-current distributions that radiate no electromagnetic fields outside the source region. When being pumped externally, induced non-radiating current configurations produce strongly localized fields inside the source region (Devaney and Wolf, 1973; Devaney, 2012), which provide the opportunity to enhance light-matter interactions. It has been theoretically shown that, for certain types of non-trivial current distributions, one can realize zero radiated power outside the source region (Devaney and Wolf, 1973; Devaney, 2012; Marengo and Devaney, 2004; Kim and Wolf, 1986). Although it is arguable that totally non-radiating sources may only be a theoretical idealism, one can define a small energy parameter $e(\omega)$ such that a source radiating energy below this threshold can be considered as essentially non-radiating (Devaney, 2012).

In order to find current distributions associated with essentially non-radiative modes in nanostructures, one approach is through multipolar decomposition involving toroidal multipole moments for current expansion in Cartesian coordinates (Radescu and Vaman, 2002; Nanz, 2016; Afanasiev, 1994). Static toroidal moments are first proposed by Zel'dovich to explain parity symmetry violation in weak interactions (Zel'dovich, 1957), and extensively studied by Dubovik (Zel'dovich, 1957; Dubovik et al., 1986; Dubovik et al., 2000; Dubovik and Tugushev, 1990; Afanasiev and Dubovik, 1998). A typical way to visualize a current distribution with toroidal moment is through thinking of the toroidal current as the current following on a solenoid wire bended into a toroid (Dubovik and Tugushev, 1990; Afanasiev and Dubovik, 1998; Afanasiev, 2001), and such a toroidal charge-current configuration can be radiationless (Afanasiev and Dubovik, 1998; Afanasiev, 2001; Afanasiev, 1993). The dynamic toroidal multipole moments are introduced in the electrodynamics as a result of splitting transverse multipoles of electric parity into two parts, namely the electric and the toroidal, where the toroidal terms are higher order terms of an expansion of the transverse multipolar coefficients of electric parity (Fernandez-Corbaton et al., ; Nanz, 2016). In general, both electric and toroidal parts contain non-radiative components due to the separation of terms of different order in the size of the source, and cancel each other when summed (Fernandez-Corbaton et al.,). As are result, toroidal multipoles are typically thought of as a third family of multipole moments other than electric and magnetic multipole moments (Radescu and Vaman, 2002), one can not separately determine the electric and toroidal parts by measuring the radiation outside the source, or by measuring the coupling between the source and external electromagnetic waves (Fernandez-Corbaton et al.,). However, this does not preclude the usefulness of modeling the current distribution inside the source using toroidal multipole moments in addition to electric and magnetic ones. Indeed, various works (Kaelberer et al., 2010; Miroshnichenko et al., 2015; Liu et al., 2015; Dong et al., 2012; Huang et al., 2012; Ogut et al., 2012; Basharin et al., 2015; Bao et al., 2015; Dong et al., 2013) have recently demonstrated that by engineering the geometry of nanostructures, one can artificially enhance the evasive toroidal moments associated with toroidal current distributions. In particular, it has been shown that one can have significant toroidal response in purely dielectric nanostructures (Kaelberer et al., 2010; Miroshnichenko et al., 2015; Liu et al., 2015; Basharin et al., 2015). On the other hand, recent works have also demonstrated the relevance of analyzing an induced current through multipolar expansion method involving toroidal multipoles (Radescu and Vaman, 2002; Nanz, 2016; Afanasiev, 1994), and design non-radiating modes (Kaelberer et al., 2010; Miroshnichenko et al., 2015; Bao et al., 2015). In particular this type of multipolar expansions (Radescu and Vaman, 2002; Nanz, 2016) identifies part of the far-field scattering power by nanostructures as being from toroial moments (Kaelberer et al., 2010; Miroshnichenko et al., 2015; Liu et al., 2015; Dong et al., 2012; Huang et al., 2012; Basharin et al., 2015; Bao et al., 2015).

In particular, the multipolar expansion (in the spherical basis) represents the scattered electromagnetic fields $\mathbf{E}_{sca}$ as a series of spherical wave harmonics with coefficients explicitly determined by radial and angular distribution of induced charge density ρ and current $\mathbf{J}$ (in the absence of magnetization) (Papasimakis et al., 2016):

$$\mathbf{E}_{sca} = \sum_{l,m} (Q_{l,m}\mathbf{\Psi}_{l,m} + M_{l,m}\mathbf{\Phi}_{l,m} + T_{l,m}\mathbf{\Psi}_{l,m}), \tag{2.10}$$

where the multipole moments that characterize dynamic multipole strengths are defined as:

$$\begin{aligned} Q_{l,m} &= \frac{c}{\sqrt{l(l+1)}} \int \rho Y^*_{l,m} \frac{d}{dr}[r j_l(kr)] d^3r \\ M_{l,m} &= \frac{1}{i\sqrt{l(l+1)}} \int (\nabla \cdot [\mathbf{r} \times \mathbf{J}]) Y^*_{l,m} j_l(kr) d^3r \\ T_{l,m} &= \frac{k}{\sqrt{l(l+1)}} \int (\mathbf{r} \cdot \mathbf{J}) Y^*_{l,m} j_l(kr) d^3r \end{aligned} \tag{2.11}$$

and $\mathbf{\Psi}_{l,m}$ and $\mathbf{\Phi}_{l,m}$ are vector spherical wave harmonics, $Y_{l,m}$ are scalar spherical harmonics, j_l are spherical Bessel functions. As result, one can associate $Q_{l,m}$ to electric multipole moments, $M_{l,m}$ to magnetic multipole moments, and $T_{l,m}$ to toroidal multipole moments. The interaction energy and farfield radiation pattern of the lowest multipole (i.e. dipole) moments in each of the three family is summarized below in Table 2.2. In particular, from the interaction energy expression of the toroidal dipole in Table 2.2, toroidal dipole interacts with the rotating part of the $\mathbf{H}$ field (since $\nabla \times \mathbf{H} = (\dot{\mathbf{D}} + 4\pi\mathbf{J})/c$ (in Gaussian units) where the $\dot{}$ denotes time derivative. A further observation is that, although toroidal dipole dipole has the same radiation pattern as the electric and magnetic counterparts, the strength of it is reduced by a factor of $(\omega/c)^2$. This relative weakness of the toroidal dipole moment in the farfield has contributed partly to the difficulty in directly observing it in experiments (Nanz, 2016).

Table 2.2: Electric, magnetic, and toroidal dipole moments ($\mathbf{p}$, $\mathbf{m}$, $\mathbf{T}$), interaction energy (W) with an electromagnetic field, and radiated power (expressed as the radial component of the Poynting vector $\mathbf{S}$) for the three multipole families.(Papasimakis et al., 2016).

Dipole moment	Interaction energy $W = \int(\rho\phi - \frac{1}{c}\mathbf{J} \cdot \mathbf{A})d^3r$	Far-field radiation patterns $(\hat{\mathbf{r}} \cdot \mathbf{S})$
$\mathbf{p}$	$-\mathbf{p} \cdot \mathbf{E} - \frac{\partial}{c\partial t}(\mathbf{p} \cdot \mathbf{A})$	$\frac{\omega^4}{4\pi c^3}\lvert\mathbf{p}\rvert^2(1 - (\hat{\mathbf{r}} \cdot \hat{\mathbf{p}})^2)$
$\mathbf{m}$	$-\mathbf{m} \cdot \mathbf{B}$	$\frac{\omega^4}{4\pi c^3}\lvert\mathbf{m}\rvert^2(1 - (\hat{\mathbf{r}} \cdot \hat{\mathbf{m}})^2)$
$\mathbf{T}$	$-\mathbf{T} \cdot (\dot{\mathbf{D}} + 4\pi\mathbf{J})/c$	$\frac{\omega^6}{4\pi c^5}\lvert\mathbf{T}\rvert^2(1 - (\hat{\mathbf{r}} \cdot \hat{\mathbf{T}})^2)$

In Fig. 2·5, visual representations of lowest order multipoles of the three families are shown. In particular, the lowest order toroidal dipole $\mathbf{T}$ (top panel in the 3rd column of Fig. 2·5) can be seen as the result of the circulation of magnetic dipole moment, which is itself a result of circulating electric dipole moment.

Since the lowest-order toroidal dipole moment is originated from the curl of induced magnetization (Dubovik and Tugushev, 1990; Afanasiev and Dubovik, 1998; Afanasiev, 2001), it can be parallel or anti-parallel to the electric dipole moment. This helps to explain the origin of these essentially non-radiating modes in nanostructures as situations where toroidal and electric dipole moments radiate out of phase and destructively interfere (Radescu and Vaman, 2002; Kaelberer et al., 2010). The resultant mode with essentially non-radiating character is termed as anapole mode, which comes from the explanation of Majorana dark matter in particle physics (Ho and Scherrer, 2013). Therefore, engineering essentially non-radiating anapole modes in high-index dielectric nanostructures is a promising alternative to increase light-matter interaction within nanostructures, and hence enhance absorbed power. Compared to conventional approaches (Casadei et al., 2015; Cao et al., 2009), engineering anapole modes in nanostructure provide an angularly and frequency broadband alternative for making components of photo-detectors, which can be readily integrated into designs

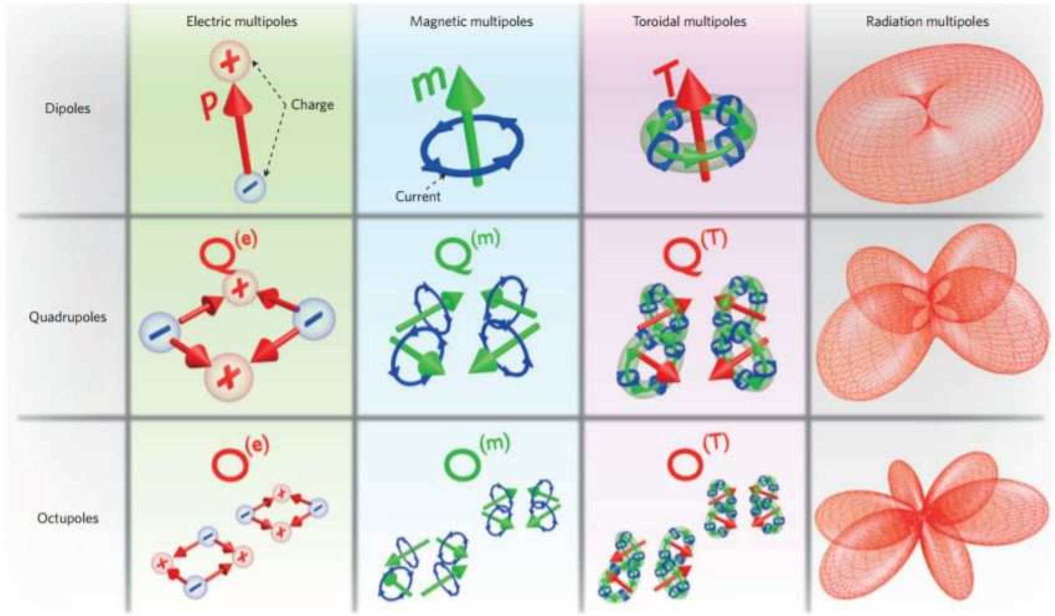

Figure 2·5: Electric multipoles represent charge configurations (far left column), whereas magnetic multipoles correspond to current sources (second column from left). The (magnetic) toroidal multipole family (second column from the right) corresponds to current distributions that cannot be represented by electric and magnetic multipoles. Same order members of each multipole family have identical power radiation patterns of corresponding oscillating multipoles (far right column). Electric and toroidal dipoles also have identical radiated field patterns as indicated by the same colour (red) arrows. (Savinov et al., 2014; Papasimakis et al., 2016) in (Michel et al., 2010; Tang et al., 2008).

In the following subsection, the application of the method of multipolar decomposition is presented. Silicon (Si) and germanium (Ge) nanodisks and square nanopixels with realistic dispersion (Palik, 1998) are used as examples to demonstrate the relevance of multipolar decomposition method to engineering anapole-induced absorption enhancement. The anapole mode can be also be excited by plane wave at oblique incidence at large angles, and are robust against low-index coatings. Finally, the potential for spectrally broadband photo-detector components is discussed by combining nanodisks or nanopixels of different sizes into single absorbing unit cell.

2.3.1 Applying the method of multipolar decomposition and anapole modes

Here, I show representative cases of current distributions induced by an external plane wave, where the far-field scattering powers can be decomposed as the radiated power by individual multipole moments and their interactions. In particular, the existence of essentially non-radiating anapole modes are found not only in high-index cylindrical nanodisks, but also in square nanopixels. The multipole moments are directly computed from the electric field distributions for each frequency (Jackson, 1999; Radescu and Vaman, 2002; Nanz, 2016). A commercial-grade simulator based on the finite-difference time-domain (FDTD) method was used to perform the calculations (Lumerical Solutions,).

In Fig. 2·6 (a), the geometry of a silicon nanodisk with diameter D and height H is shown. A linearly polarized plane wave is used to excite the structure. For an example structure with $D = 350nm$ and $H = 60nm$, we show in Fig. 2·6(b) and (c) the electric and magnetic field enhancements when the structure is in the anapole mode at 710nm. The arrows overlapping the field plots indicate the field directions for the electric and magnetic fields respectively (see Fig. 2·6 (b) and 2·6(c)). The electric

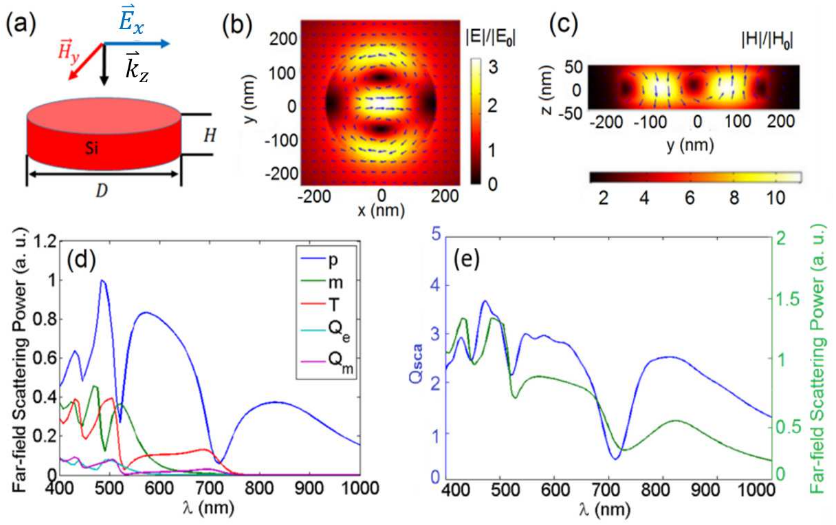

Figure 2·6: For a single Si nanodisk in the anapole mode, (a) geometry of nanodisk and excitation condition for anapole mode, (b) and (c) are the E-field and H-field enhancement at anapole mode respectively, the superimposed arrows indicates the direction of the fields. (d) The full multipolar decomposition of the first contributing five multipole moments: electric dipole ($\mathbf{p}$), magnetic dipole ($\mathbf{m}$), toroidal dipole ($\mathbf{T}$), electric quadrupole (Q_e), magnetic quadrupole (Q_m). The powers are normalized with respect to the maximum value by electric dipole in the investigated spectrum. (e) The far-field scattered power (green, in arbitrary units) as a sum of all intensity contribution from multipole moments in (d), as well and the actual scattering efficiency (blue) with normalization with respect to the geometrical cross-section area. In this case $D = 350nm$ and $H = 60nm$. (Wang and Dal Negro, 2016) field distribution in Fig. 2·6(b) is typical to the anapole mode, where almost all of the field circulates inside the square nanopixel. The magnetic field in Fig. 2·6(c) is also mostly confined into the square nanopixel, and the vortex in the middle as a result of rotation of the induced magnetic field is responsible for the toroidal dipole (Ho and Scherrer, 2013; Casadei et al., 2015; Staude et al., 2013). Based on the computed field distributions inside the structure, we can calculate the current distribution at each frequency using (Jackson, 1999):

$$\mathbf{J}(\mathbf{r}) = -i\omega\epsilon_0(n^2 - 1)\mathbf{E}(\mathbf{r}), \tag{2.12}$$

where $\mathbf{J}$ and $\mathbf{E}$ are current and electric field distributions at internal positions $\mathbf{r} = (x, y, z)$ in a Cartesian coordinate system, ω is the angular frequency, ϵ_0 is the dielectric permittivity of the free space, and is the complex refractive index of the structure. With the calculated current distributions in the nanodisk, we can then compute the components of the first five multipole moments (see Table 2.3) (Radescu and Vaman, 2002), where $\mathbf{p}$, $\mathbf{m}$, $\mathbf{T}$, $Q_{\alpha\beta}$, $M_{\alpha\beta}$ are components of electric dipole, magnetic dipole, toroidal dipole, electric quadrupole, and magnetic quadrupole moments, respectively. c is the speed of light in the free space (Table 2.3). The indices, α and β, take x, y, and, z. From the computed values of these radiating multipole moments, we can calculate the decomposed far-field scattered power by each multipole moment and their interactions (Radescu and Vaman, 2002). From Ref. (Radescu and Vaman, 2002), the expansion of the far-field scattering power in term of the contribution from multipole moments to the order of c^{-5} includes an extra term, which is proportional to the interaction between the magnetic dipole and the first-order mean radius of its distribution. In this case, this term is universally zero and is therefore omitted.

In Fig. 2·6(d) we plot the far-field power scattered by each radiating multipole

Table 2.3: Current multipoles and their far-field scattering powers (Wang and Dal Negro, 2016).

Multipole Expression	Far-field Scattering Powers
$\mathbf{p} = \frac{1}{i\omega}\int \mathbf{J} d^3r$	$I_p = \frac{2\omega^4}{3c^3}\|\mathbf{p}\|^2$
$\mathbf{m} = \frac{1}{ic}\int \mathbf{r} \times \mathbf{J} d^3r$	$I_m = \frac{2\omega^4}{3c^3}\|\mathbf{m}\|^2$
$\mathbf{T} = \frac{1}{10c}\int \{[\mathbf{r} \cdot \mathbf{J}]\mathbf{r} - 2[\mathbf{r} \cdot \mathbf{r}]\mathbf{J}\} d^3r$	$I_T = \frac{2\omega^6}{3c^5}\|\mathbf{T}\|^2$
($\mathbf{p}, \mathbf{T}$ interaction)	$I_{pT} = -\frac{4\omega^5}{3c^4} Re[\mathbf{p} \cdot \mathbf{T}]$
$Q_{\alpha\beta} = \frac{1}{2i\omega}\int \{r_\alpha J_\beta + r_\beta J_\alpha - \frac{2}{3}[\mathbf{r} \cdot \mathbf{J}]\delta_{\alpha\beta}\} d^3r$	$I_Q = \frac{\omega^6}{5c^5}\sum \|Q_{\alpha\beta}\|^2$
$M_{\alpha\beta} = \frac{1}{3c}\int \{[\mathbf{r} \times \mathbf{J}]_\alpha r_\beta + [\mathbf{r} \times \mathbf{J}]_\beta r_\alpha\} d^3r$	$I_Q = \frac{\omega^6}{20c^5}\sum \|M_{\alpha\beta}\|^2$

moments for the representative geometry with $D = 350nm$ and $H = 60nm$. From Fig. 2·6(d), all five multipole moments contribute to the far-field scattered power at shorter wavelengths, while electric dipole moments dominate at larger wavelengths. The interesting region happens near $700nm$, where electric dipole and toroidal dipole are the dominating radiating multipole moments. From the definition of electric and toroidal dipoles (Table 2.3), it is possible to have them destructively interfere and even cancel each other. This can be identified as an anapole mode. Besides, the partial cancellation between the electric and toroidal dipole near $500nm$ can also be identified as a partial anapole response, although the overall mode (i. e. electric and magnetic field distributions) is affected by other multipole moments. On the other hand, contributions from other multipoles and interaction between p and T makes the anapole not fully radiationless. In particular, the magnetic quadrupole moment is responsible for non-zero overall far-field scattered power near $700nm$ (Fig. 2·6(e)). Besides, as $\mathbf{p}$ and $\mathbf{T}$ are anti-parellel, the term I_{pT} becomes positive. The total scattering efficiencies normalized to the nanoparticles geometrical cross-section in Fig. 2·6(e) confirms the essentially non-radiating feature with a significant minimum at $700nm$. It is also worth noticing that, although the anapole mode is not totally radiationless, the scattering cancellation is angularly broadband as indicated by a minimum in the overall scattering cross-section in Fig. 2·6(e). This is to be contrasted with cases where electric and magnetic dipole moments interfere to cancel only the backward scattered light (Staude et al., 2013; Liu et al., 2012). Finally, as other multipole moments decrease faster than the electric and toroidal dipole moments, the anapole mode at longer wavelengths (near $700nm$ in this case) has a purer anapole response than the one near $500nm$. From Fig. 2·6, an important observation is that the toroidal dipole moment is responsible for the essentially non-radiating behavior of the structure, and it is induced circulation of the magnetic field, i.e. the magnetic field vortex, is in the YZ-plane (Fig. 2·6(c)). Therefore, for a given dielectric material, it is the aspect ratio (H/D in this case) rather than the geometric shape of the top cross-section (XY-plane) that is responsible for the formation of the magnetic field vortex and the essentially non-radiating mode. Indeed, while the study of anapole Si nanodisk is pioneered by Ref. (Miroshnichenko et al., 2015), we found that, for high-index dielectric nanostructures, it is not necessary to use cylindrical nanodisk to realize anapole modes. In fact, we can realize in a variety of geometries. In particular, we extend the circular cross-section of the nanodisk to a square, which we refer to as a square nanopixel, and show that the anapole mode can be also engineered in the same fashion.

Figure 2·7(a) shows the geometry of a square nanopixel, the normally incident linear plane wave has its electric field along one of the sides of the square nanopixel. In this particular example, we use the square nanopixel with the same height H and side length D (diameter in the case of nanodisks) as the nanodisk case in Fig. 2·6. Through multipolar decomposition, Fig. 2·7(b) demonstrates that the same origin of the anapole mode in square nanopixels. In particular, the far-field scattering power of both electric and toroidal dipole moments are similar in strength near $750nm$ (Fig. 2·7(b)), which give interfere destructively and give rise to the anapole mode (Figs. 2·7(c) and 2·7(d))similar to the nanodisk case. In the next subsection, we discuss how

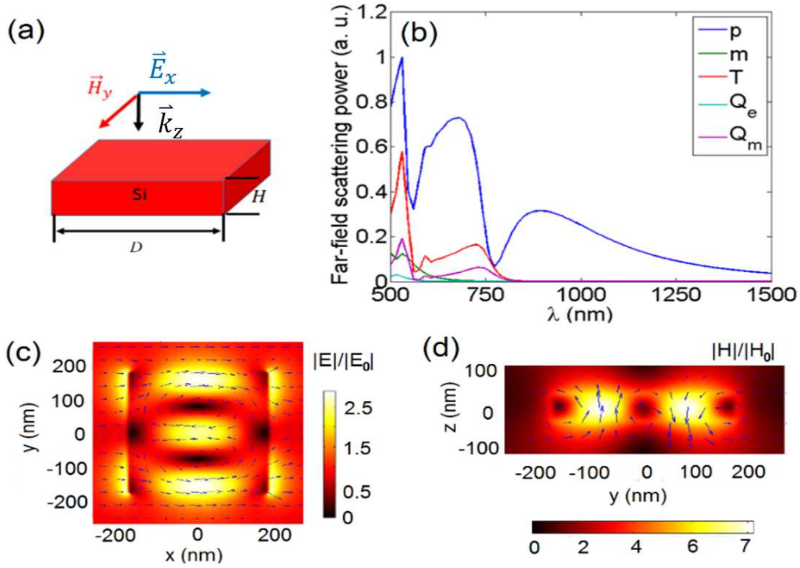

Figure 2·7: (a) Geometry of Si square nanopixel and excitation condition for anapole mode, (b) The full multipolar decomposition of the first contributing five multipole moments: electric dipole ($\mathbf{p}$), magnetic dipole ($\mathbf{m}$), toroidal dipole ($\mathbf{T}$), electric quadrupole (Q_e), magnetic quadrupole (Q_m). The powers are normalized with respect to the maximum value by electric dipole in the investigated spectrum. (c) and (d) are electric and magnetic field enhancements at the anapole mode. In this case $D = 350nm$ and $H = 60nm$.(Wang and Dal Negro, 2016) geometric and other relevant parameters affect the performance of anapole-induced absorption rate enhancements.

2.3.2 Effect of geometry, incidence angle, dielectric coating and change of material

In the previous section, it has been shown that the decomposition of multipole moments of a current source provides a robust approach to investigate the contributions by various radiating current multipole moments, and can be used to engineer non-radiating anapole modes. This section summarizes the results from systematically studying of the effects of the geometry of silicon and germanium nanodisks (and square nanopixels) on the multipole moments, especially the anaople modes. Then, the study also includes the effect of oblique incidence, and low-index coating. In the study, the absorption rate enhancements is defined by the ratio between the amount of power absorbed by a single Si nanodisk or nanopixel to that by a segment of an infinite Si thin-film with the same thickness and volume:

$$\gamma_{abs} = \frac{P_{abs}}{P^0_{abs}}, \tag{2.13}$$

where P_{abs} is the power absorbed by the single Si square nanopixel, and P^0_{abs} is the power absorbed by the reference thin-film case. In each case, since the structure has no imaginary magnetic permeability, the power absorbed by the structure at each wavelength is calculated using [79]:

$$P_{abs} = \frac{\omega}{2} \int \epsilon_r\text{"} |\mathbf{E}(\mathbf{r})|^2 d^3r, \tag{2.14}$$

where ϵ_r" is the imaginary part of the relative dielectric permittivity. The effects of geometric sizes (D and H) on the wavelengths for the peaks of anapole-induced absorption rate enhancements are summarized in Figs. 2·8 and 2·9.

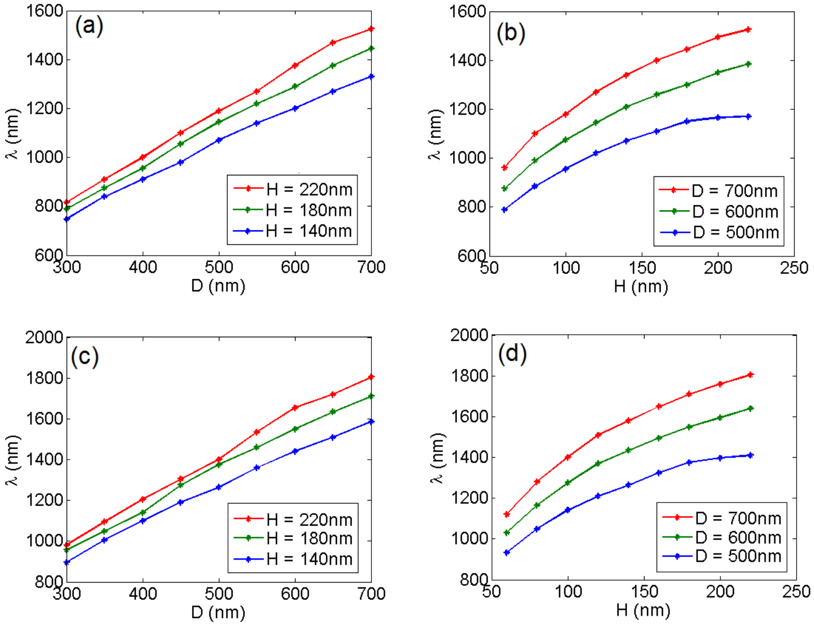

Figure 2·8: (a) and (b) are the change in the wavelengths of anapole-induced absorption rate enhancement peaks depending on *D* and *H* respectively for Si nanodisks. In each panel, three representative fixed heights or diameters are shown. (c) and (d) are the similar study for Si square nanopixels.(Wang and Dal Negro, 2016)

In Fig. 2·8(a), the shift anapole-induced absorption rate enhancement peaks is shown when the diameter of the nanodisk is increased, for three representative cases of fixed heights for Si nanodisks. The wavelength for the anapole-induced absorption rate enhancement peaks is found to follow an almost linear trend as we increase the diameter. This is expected since the anapole is a resonant behavior, and the wavelength of resonance should increase linearly with respect to the geometric size. In Fig. 2·8(b), the shift anapole-induced absorption rate enhancement peaks when is shown for varying height of the nanodisk, and for three representative cases of fixed diameters for Si nanodisks. The trend is less linear as the wavelength increase saturates when the height of the nanodisk increases. Fig. 2·8(c) and 2·8(d) are the counterpart cases for Si square nanopixels with the same D and H values. Since the volume for a square nanopixel is larger than a nanodisk with the same D and H, the wavelengths at which the anapole-induced absorption rate enhancements occur are slightly higher. Other than this, the general trend for the shift of anapole-induced absorption rate enhancements peaks due to an increase in D or H is very similar to the behavior found for the Si nanodisk case.

Figure 2·9 shows the cases where the material in Fig. 2·8 is replaced by Ge, while keeping all other geometrical shapes and sizes constant. The general effects of changing D (also for the cases of square nanopixels) and H are the same as the cases for Si. Overall, the wavelengths at which the anapole occurs for the Ge cases are slightly higher compared to the Si cases, due to higher refractive index of Ge. From both Figures, by varying the geometric size shape of Si and Ge nanodisks or square nanopixels, there is a wide tunability for the wavelength of the anapole-induced absorption rate enhancements. In realistic situations, it is also important to consider the effect of non-ideal incident angles. Fig. 2·10(a) and 2·10(b) shows the effect by the angle of incidence for a Si nanodisk and a Si square nanopixel,

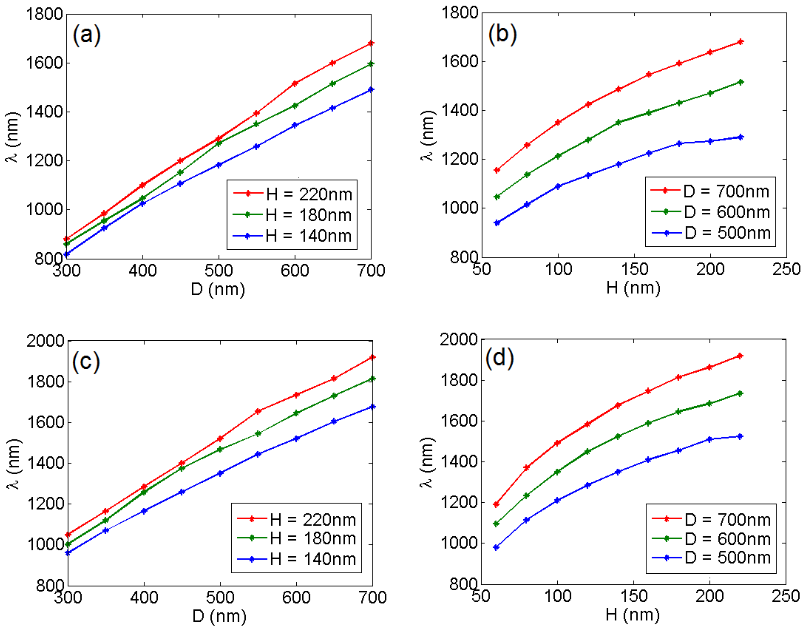

Figure 2·9: (a) and (b) are the change in the wavelengths of anapole-induced absorption rate enhancement peaks depending on *D* and *H* respectively for Ge nanodisks. In each panel, three representative fixed heights or diameters are shown. (c) and (d) are the similar study for Ge square nanopixels.(Wang and Dal Negro, 2016) respectively. They both have the same $D = 350nm$, and $H = 60nm$. In this case, because of the symmetry of the situation, we need to consider two different linear polarizations. We show that, for both polarizations, the wavelength for the anapole-induced absorption peak blue-shifts, as the nanodisks cross-sectional area decreases. For p-polarized plane wave, the anapole modes are less affected in both nanodisk and square nanopixel cases (blueshifts by about $10\circ$ as compared to $20\circ$ in the s-polarized cases). We found that the quality of anapole modes in both nanodisk and square nanopixel cases quickly deteriorate for the s-polarized plane wave, when the angle of incidence moves away from normal incidence condition ($0\circ$). The reason is that s-polarized plane wave results in a stronger magnetic dipole response in the nanodisk, and effects the purity of the anapole mode. As the incident angle increases, the increases in scattering efficiency at the wavelength of the anapole mode also indicate a less pure anapole response (more energy radiated). Nevertheless, the anapole mode in Si nanodisk can be induced by obliquely incident plane wave with an angle as high as $20\circ$ to $30\circ$ away from the normal incidence. The same conclusion can also be extended to Ge nanodisks and square nanopixels.

The effect of dielectric coatings on the anapole mode is also investigated. The representative cases is shown where low-index ($n = 1.8$) coating is attached to both sides of a Si nanodisk (Fig. 2·10(c)) and Si nanopixel (Fig. 2·10(d)), both with $D = 350nm$ and $H = 60nm$ (inset, Figs. 2·10(c) and 2·10(d)). Apart from negligible shift in the peak of the absorption rate enhancement in both cases, the value of the enhancement is also insignificantly affected (Figs. 2·10(c) and (d)). This shows that non-radiating anapole modes and the anapole-induced absorption rate enhancements are robust with respect to low-index coatings.

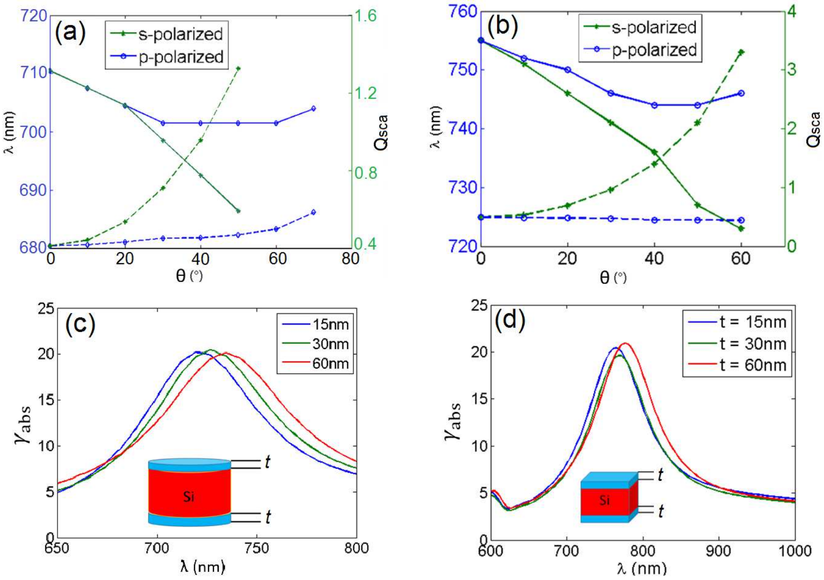

Figure 2·10: (a) and (b) show the change in the wavelengths of anapole-induced absorption rate enhancement peaks for two linear polarizations at varying incident angles with respect to the normal to the surface, for Si nanodisk and square nanopixel respectively. Both have $D = 350nm$, and $H = 60nm$. The scattering efficiency Qsca is obtained by normalizing with the projected area of the square nanopixel onto the plane of the wave front. (c) and (d) show the effect of absorption rate enhancement change for three representative cases with different thicknesses d of ITO ($n = 1.8$) coatings on both side of the Si nanodisk or square nanopixel (insets) with the same geometries as in (a) and (b) respectively. (Wang and Dal Negro, 2016)

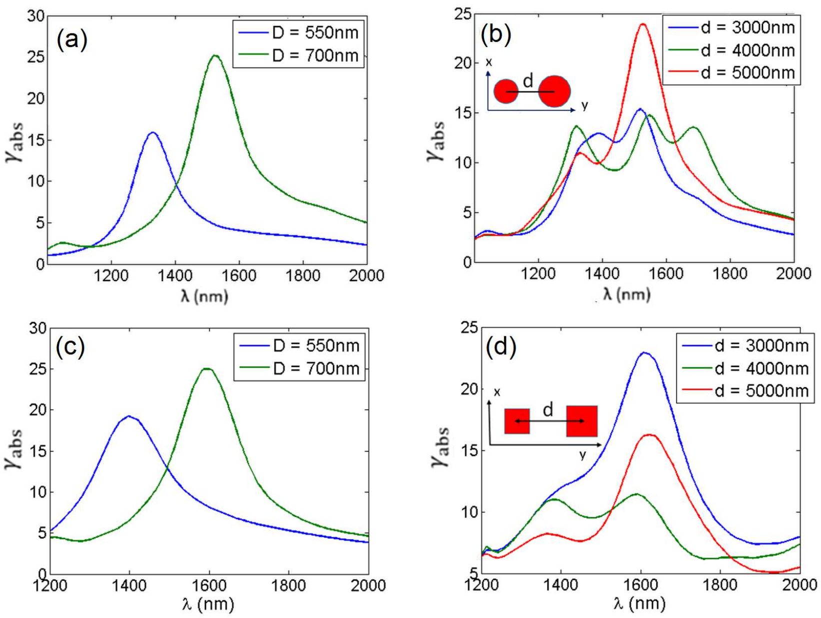

Figure 2·11: The absorption rate enhancements for a surface element formed by two Ge square nanopixels of side lengths 550nm and 700nm respectively (H = 100nm). (a) The absorption rate enhancements of each single Ge square nanopixel, and the inset show that they are to be separated with distance d (center-to-center) in a surface element. (b) shows the absorption rate enhancements for three different separations.(Wang and Dal Negro, 2016)

2.3.3 Absorption spectrum engineering using arrays of square nanopixels with varying sizes

In this subsection, we demonstrate the opportunity of using array of nanodisks or square nanopixels with different side lengths to broaden the bandwidth of anapole-induced absorption rate enhancements. In this case, the inhomogeneous arrays are formed using nanodisks or square nanopixels of different side lengths.

Figure 2·11(a) shows the absorption rate enhancements of single Ge nanodisks of two different side lengths and the same height $H = 100nm$. The inset of Fig. 2·11(b) shows a situation where each pair of the two square nanopixels form a unit base for an absorbing surface. When we consider absorption rate enhancements (normalized with respect to the total material volume) of the unit base, we can achieve a larger bandwidth for the absorption rate enhancement. Figure 2·11(b) shows the absorption rate enhancements for three different cases of separations $d = 3000nm$, $4000nm$, and $5000nm$ respectively. In particular, when the two Ge nanodisks are separated far enough ($5000nm$ in this case), we can clearly see two distinct peaks as a result of anapole-induced absorption rate enhancement at different wavelengths. Because of the fact that the normalization is with respect to the total (enhance larger) volume, the maximum absorption rate enhancement (Fig. 2·11(b)) is lower than the highest for individual cases (Fig. 2·11(a)). In Figs. 2·11 (c) and 2·11(d), we replace the Ge nanodisks by Ge square nanopixels. Similar to the case with nanodisks, we are able to use square nanopixels with absorption rate enhancement peaks at different wavelengths (Fig. 2·11(c)) to engineer absorption rate enhancements in larger wavelength rages (Fig. 2·11(d)). Comparing Fig. 2·11(b) and 2·11(d), we also notice that the optimal distance of separation for nanodisks or square nanopixels are different. For example, at the center to center separation of $3000nm$, Ge nanodisks have similar absorption rate enhancements for either nanodisk at its own absorption rate enhancement peaks. For square nanopixels, the condition is achieved when separation is $4000nm$. This different provide further optimization opportunities at the level of using arrays of nano-geometries, and is beyond the scope of the current paper. We also expect that when nanodisks or square nanopixels of more side lengths are included, a further broadening of the bandwidth for the absorption rate enhancement.

2.3.4 Section summary

Based on rigorous multipolar decomposition method, we have shown that we can enhance absorption rates through engineering angularly broadband non-radiating anapole modes in high-index dielectric nanostructures. We have used Si and Ge nanodisks and square nanopixels as examples for demonstration. In particular, we have shown that the wavelength of the anapole-induced absorption enhancement peak is widely tunable by varying the diameter (or side length as in the case of square nanopixels) D and height H of Si and Ge nanodisks and square nanopixels, and by increasing either of the geometric parameters (D or H) we can increase the wavelength of the anapole mode in an almost linear fashion. We also noticed that, by increasing D while keeping H constant rather than the other way round, we separate the anapole mode further away from other multipole moments, especially magnetic dipole moment. The ideal aspect ratio for anapole modes is near $H/D \sim 0.2$. We have also shown that nanodisks and square nanopixels made with germanium have more advantage of being used to engineer anapole induced absorption rate enhancements, since its higher refractive index makes the anapole modes more separated from other multipole moments compared to Si cases. We also found that the anapole mode associated with absorption rate enhancement can be achieve not only by normally incident plane wave, but also by obliquely incident plane wave. For oblique incidences, the anapole mode is polarization sensitive, and the quality of the anapole mode deteriorates beyond $30\circ$ especially for s-polarization. Furthermore, the anapole-induced absorption peak is robust against low-index coatings on both sides of the nanodisk or the square nanopixel. With these results, engineering wide bandwidth absorbing layers can be realized by mixing nanodisks or square nanopixels with different side lengths. In particular, we have shown that unit cells formed by Ge nanodisks or square nanopixels of two different side lengths can increase the bandwidth of the absorption rate enhancement in the near-infrared spectral range.

2.4 Chapter summary

In this chapter, I reviewed my works related to direct and inverse design of single nanoparticles for various applications. In particular, novel ITO disks are shown to have tunable resonances in the mid-infrared spectral range, and resonant nearfield enhancement of nanorods made of gold provide an avenue for quantum efficiency enhancement of silicon nanocrystals. However, in order to optimize single-particle designs for general applications, it is important to answer two questions. In particular, in order to address the problem of optimal geometrical shape and size of single nanoparticles, I have demonstrated how the inverse design paradigm by parameterizing a general geometric shape using superformua can be useful for optimizing the surface field enhancement of plasmonic nanoparticles. In order to address the problem on the nature of the modes, I have shown my work using multipolar decomposition including toroidal moments, and used it for engineer anapole modes for enhanced absorptions. At the end of this example, it has been shown that, for engineering broadband spectral features such as absorption, arrays of more than one types of elements are needed. Indeed, for many device applications, large device footprint and complexity of functions require the engineering of nanostructure resonances beyond the single-element level. Therefore, in the next chapter I will extend my discuss to my works related to array-geometry engineering.

Chapter 3

Engineering Collective Resonances Through Geometry of Nano-arrays

In the previous chapter, I have shown works related to engineering single-element's resonances, and addressed problems on the optimal shapes for resonance effect and the nature of resonances. In this chapter, I show my work related to engineering collective resonances of nanostructures.

In order to motivate the need for collective resonances I first introduce an example based on nano-fiber "forest", which is a work I collaborated with Ran Zhang in our group and Prof. Minteer's group from the University of Utah(Chen et al., 2016). In this example, nanofibers of different size and shapes are disorderly placed on the surface of nanostructure to provide broadband resonance features. However, collective resonances of disordered nanostructures are difficult to control as the composition and proportion of constituent resonant elements are mostly random. For many applications, it is important to have controllable designs of collective resonances. Therefore, in the third section I use my work in collaboration with Ekin Aslan and Erdem Aslan on using fractal nanoantennas to provide controllability of multiband resonances (Aslan et al., 2016).

The work on fractal nanoantenna points to a reductionist approach on engineering and understanding collective resonance. While we can understand the fractal antenna as a collection of different resonant elements, engineering collective resonances is also possible through exploiting the geometrical arrangement of identical resonant units. In this approach, we are able to decouple the resonance effect of geometrical arrangement and the property of single resonant units.

In order to show that collective resonance by arranging identical elements can indeed provide emergent optical properties, I introduce my work on helical nanoantenna (Wang et al., 2015). In this case, novel polarization and beaming control of helical geometry can be understood as collective properties of single helical turns arranged periodically in the nanohelix.

In addition, our group has been pioneering in exploring the collective effect base on quasiperiodic and aperiodic (see Chapter 4.1 for more detailed introduction) nanostructures, and many of the works have been related to Vogel spirals (Trevino et al., 2012a; Christofi et al., 2016; Pollard and Parker, 2009; **?**; Liew et al., 2011; Dal Negro et al., 2012; Lawrence et al., 2012b). In the fourth section, I use my recent work in collaboration with Prof. Kirby's group at the University of Utah on optimizing Vogel spiral arrays of plasmonic nanospheres for enhanced absorption and scattering to show case how inverse engineering collective resonances is possible purely through manipulation of geometrical arrangement of identical elements.

I will leave the part on rigorous understanding and engineering of such aperiodically arranged geometries to the next chapter.

3.1 Collective resonances of nano-forests and fractal nanoantennas

3.1.1 Gold nanofiber-based electrodes for plasmon-enhanced electrocatalysis

In this example, the role of light-induced resonant phenomena in electrocatalysis is investigated. In particular, our group made random networks of gold nanofibers as a novel type of electrode for enhanced electrocatalytic activities. The fabricated sample

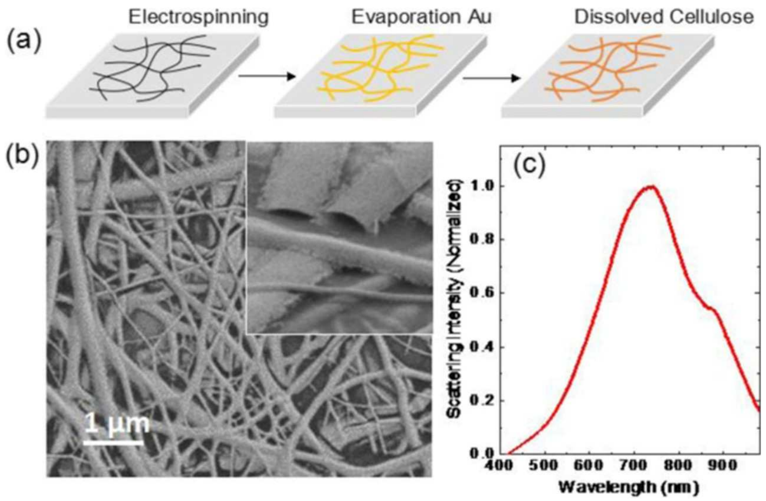

Figure 3·1: (a)Au nanofiber fabrication process. (b) SEMmicrograph of a fabricated electrode. (c) Measured dark-field scattering spectrum of a representative Au nanofiber sample. (Chen et al., 2016)

of a ”nano-forest” of gold half-shells by Ran Zhang is shown in Fig. 3·1, where he first created dielectric cellulose fibers through electrospinning and removed the dielectric part after deposition of gold (Fig. 3·1(a)). Figure 3·1(b) shows the SEM image of the nanofiber-based electrode, where randomly arranged gold half-shells of different sizes are displayed. A broadband characteristic scattering intensity spectrum of the sample is shown in Fig. 3·1(c).

In order to better understand the origin of the broadband resonant peak in the measured dark-field scattering data (Fig. 3·1(c)), it is not enough to attribute the resonance behavior to individual gold(Au) fibers. In particular, in this case, collective resonance from Au fibers of different sizes contribute to the overall broadband scattering spectrum of the measured sample. Therefore, I modeled a long ($10\mu m$) Au half-shell structure placed atop an indium tin oxide (ITO) substrate, which reproduces the actual morphology of the measured samples. Figure 3·2 shows the simulation geometry and the calculated results using 3D finite-difference time-domain (FDTD) method. As shown in Fig. 3·2(a), I use a normally-incident and linearly polarized plane wave illumination with electric field in the transverse plane (x-y plane) as a simple model for excitation. In the simulations I also included the ITO substrate with a measured refractive index $n = 1.8$. The relevant geometrical parameters of a single Au half-shell are the external diameter D and shell thickness h as shown in Fig. 3·2(a). The values of these two parameters are measurable and chosen to be consistent with the values extracted from SEM data on the actual samples. Figure Fig. 3·2(b) shows the electric field distribution in the near field of an Au half-shell responsible for the observed peak in the dark field scattering spectrum ($738nm$). The computed field distribution demonstrates the excitation of an electric multipole mode that resonates along the length of the Au half-shell. Figure 3·2(c) shows the calculated scattering efficiencies (scattering cross-sections normalized to the physical cross-sectional area of the half-shell in the z-x plane), for structures with fixed $h = 7nm$ and varying D. As D increases, we observed redshift in the scattering peak, as expected for nanofiber-based plasmonic systems 22. Moreover, Figure 2d shows that the peak of the scattering efficiency redshifts as h decreases due to the excitation of coupled surface plasmon modes. From the calculated scattering efficiency results,we can see that, when considering a half-shell with $D = 250nm$ and thickness of $7nm$, the scattering peak occurs around $738nm$, which is in qualitative good agreement with the measured dark-field scattering spectra (broad peak near $740nm$) and fully compatible with the measured geometrical parameters obtained from the SEM analysis.

From this example, it is evident that although such random structure enables broadband engineering for certain applications such as electrocatalysis, the lack of controllability on collective behavior of resonances makes such nanostructures not ideal for many potential applications such as biosensing and multispectral detection. As a result, a more common approach that has been adopted uses fractal nanoantennas, which I will now discuss with the example of my collaborate work in the next

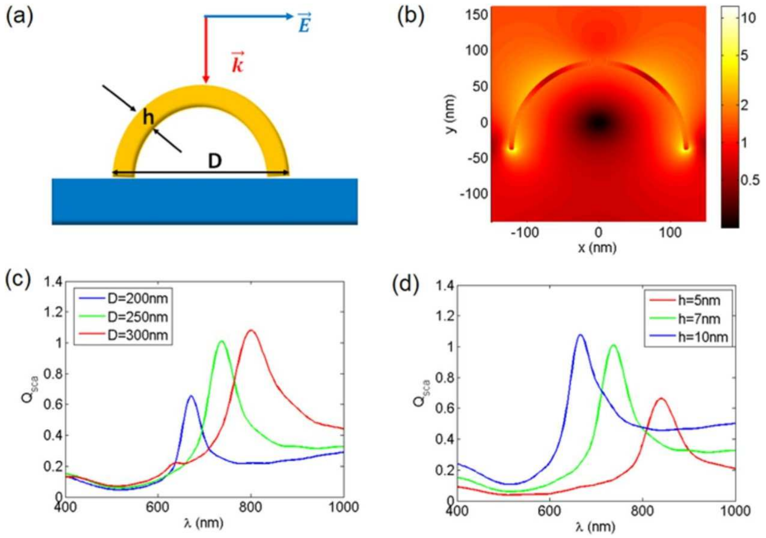

Figure 3·2: Simulation setup and results of Au half-shell using finite-difference time-domain (FDTD) method. (a) shows the simplified model of a Au half-shell with external diameter D and thickness h on an ITO substrate (refractive index = 1.8), pumped by linearly polarized plane wave with transverse electric field at normal incidence. (b) is a representative electric field plot of the mode at $738nm$ for a structure with $D = 250nm$ and $h = 7nm$. The color bar shows the electric field enhancement, normalized to the amplitude of the incident electric field. (c) shows scattering efficiency shift due to varying D, for fixed $h = 7nm$. (d) shows scattering efficiency shift due to varying h, for fixed $D = 250nm$. (Chen et al., 2016) subsection.

3.1.2 Multispectral Cesaro-type fractal plasmonic nanoantennas

Unlike in the case of electrolysis, many applications require controlled design of collective resonances. In the following example, Cesaro-type fractal plasmonic nanoantenna serves as a platform for biosensing with engineered multi-resonant spectrum based on carefully designed collective resonances.

Cesaro fractals, also known as PeanoCesaro triangle sweeps, are among the early examples of space-filling continuous curves with topological dimension $d = 1$ and fractal dimension $DF < 2$. Differently from the more famous Peanos space-filling curve (Batty and Longley, 1994; Mandelbrot, 1977) whose fractal dimension is equal to the Euclidean dimension of the embedding space, Cesaros curves are more irregular and feature a hierarchical structure of self-similar pointed or spiky resonant elements that repeat the same geometrical motif when filling the Euclidean plane with a constant scaling factor (Cesàro, 1905). Cesaro fractal structures can be generated by a recursive geometrical algorithm using a Lindenmayer system (L-system) implementation (Flake, 1998), which enables easy optimization and customization of desired geometrical features. Moreover, differently from other examples of space-filling objects, Cesaro-type fractals scale inwardly; namely, their total size does not grow with the fractal generation number n, but it is determined at the outset in order to cover a prescribed area. This characteristic geometrical property is extremely appealing to plasmonic antenna engineering since it provides a simple approach to enable a large number of individual resonances with controllable log-periodic spacing on a small device area. In this paper, different generations of Cesaro nanoantennas are analyzed, which are created using a turtle language interpretation of the custom-made L-system. Here it suffices to say that an L-system is a deterministic approach to iteratively generate complex fractal objects starting from a finite alphabet of symbols and a collection of production rules. These rules are simple prescriptions, such as inflations, that expand each symbol into larger strings of symbols starting from an initial "axiom" that is considered the seed of the recursive construction. L-systems provide a computationally efficient and general method to produce many fractal shapes, including Cesaro fractals. In particular, this work uses a turtle graphics implementation of the L-system in the SI that gives rise to the Cesaro antenna structures shown in Figs. 3.1.2(a) to 3.1.2(e). for different generations of the algorithm. Turtle graphics is an ideal tool to geometrically interpret L-systems, and it consists of a series of simple moves prescribed by a command list executed by a cursor, called the turtle, on a graphic screen. Typical examples are simple instructions such as move forward 10 steps and turn by an angle of θ degrees. When combined with control flow procedures and recursion, the idea of turtle graphics implementations of L-systems becomes a powerful tool to generate fractal structures. In particular, the vertices (x, y) of the Cesaro fractal structures displayed in Fig. 3.1.2(a) to 3.1.2(e) can be easily obtained for each generation number n and imported directly into the FDTD simulation software (Lumerical Solutions,) for electromagnetic modeling. Figure 3.1.2 shows a top view of the first five generations of the designed Cesaro nanoantenna. The geometry is obtained with 10○ aperture spikes. Additional spikes are added at each iteration step with a constant ratio of lengths, or scaling factor k. The scaling factor is the ratio of the spikes lengths L_n/L_n1 and equals 0.46 in this case. The maximum linear dimensions of the structure remain the same for all the iterations, while Ln, the minimum size of the spikes for the nth generation, progressively decreases. The Cesaro fractal is a deterministic fractal object with a fractal dimension (Flake, 1998; Cesàro, 1905; Mandelbrot, 1977; Batty and Longley, 1994) $D_F = \lim_{n\to\infty} \frac{\ln N(n)}{\ln(1/r_n)} = 1.7852$ where $N(n)$ is the number of elements needed to cover it at each generation and $r_n = L_n/L_0 = (0.46)^n$ is the scaling ratio (Batty and

Longley, 1994) where $L_0 = 9686nm$ in this case.

Cesaro-type metallic nanoantennas exhibit large and controllable spectral density within a compact design that supports multifrequency operation capabilities. In order to demonstrate this property, we investigate the scattering and absorption behavior of the first five iterations of the antenna with a maximum linear size $W = 6849nm$. The calculated scattering efficiency $\eta_{sc} = \sigma_{sc}/A$ and the absorption efficiency $\eta_{abs} = \sigma_{abs}/A$ (cross sections normalized by the geometrical area A of the device) are shown in Figs. 3.1.2(f) and 3.1.2(g), respectively. These parameters are numerically computed using the three-dimensional FDTD method (Lumerical Solutions,) with perfectly matched layers. Realistic Au dispersion data are considered as in Ref. (Palik, 1998), and the Au thickness is fixed to $30nm$. Unless otherwise stated, all simulations are performed under x-polarization and using a uniform mesh size of $3nm$ across the structures. The cross section and spatial distribution simulations are carried out without any substrate, while the transmission and reflection simulations are performed with the antennas atop the CaF_2 substrate. As clearly shown in Figs. 3.1.2(f) and 3.1.2(g), each generation of the antenna introduces additional resonant bands at higher frequencies. In particular, the number of individual resonances in a Cesaro antenna simply equals its generation number n and does not depend on the total device footprint. This characteristic behavior of Cesaro fractal structures can be better understood by studying the electric field distribution and the corresponding charge density ρ for the plasmon modes at each generation of the antenna, as shown in Fig. 3.1.2. The spatial maps of near-field electric enhancements, $|E|/|E_{in}|$ as well as the charge and current densities at the resonant peaks unveil the role of local and global geometrical symmetries of plasmonic structures and of the corresponding plasmon resonances (Gottheim et al., 2015; Trevino et al., 2013). All these parameters are calculated from the near-field distribution. Although, it is well known that there exists a red-shift between far-field and near-field responses of nanoantennas (Alonso-González et al., 2013), in order to understand the fractal scaling effect on the spatial distributions, we carried out these analyses for the far-field scattering peaks. In all corresponding charge density maps, charge density values are normalized to $\rho_0 = 0.141C/m^3$ and $Re[\rho/\rho_0]$ is shown. Meanwhile, current density amplitudes are normalized to $J_0 = 1.75 \times 106A/m^2$ and given as $|J/J_0|$ in all current density maps.

The results demonstrate the excitation of dipole-type modes that extend across the entire structure. On the other hand, by increasing the fractal generation number n the antenna exhibits smaller and smaller clusters of resonant features with the same local geometry, resulting in additional plasmonic modes at higher and higher frequencies, as shown in Fig 3.1.2. This mechanism provides a multiscale electromagnetic hot-spot density that produces large values of electric and magnetic field enhancement (Li et al., 2003). Electric field (E-field) distributions are illustrated in Fig. 3.1.2 for the modes corresponding to the scattering peaks from the longest to the shortest wavelength in Cesaro nanoantenna of the fifth generation. For better visualization in Figs. 3.1.2(e) to 3.1.2(h) we show the first quarter of the structure, while in Figure Figs. 3.1.2(a) to 3.1.2(d) we display the field distributions over the entire structure. As it can be noticed by analyzing the distribution of electric hot-spots in the left panels of Fig. 3.1.2, the subclusters of the antenna structure at the smaller scales resonate with shorter wavelength radiation, leading to multiscale hot-spot distributions with strongly enhanced local electromagnetic fields. This hierarchical cascade of optical resonances at different length scales of the antenna can also be appreciated from the charge density distributions displayed in the right panels of Fig.3.1.2. These plots demonstrate clearly that the plasmonic resonances of the antenna for the nth generation consists of nth subclusters of dipolar modes formed by the opposing metallic spikes in the structure.

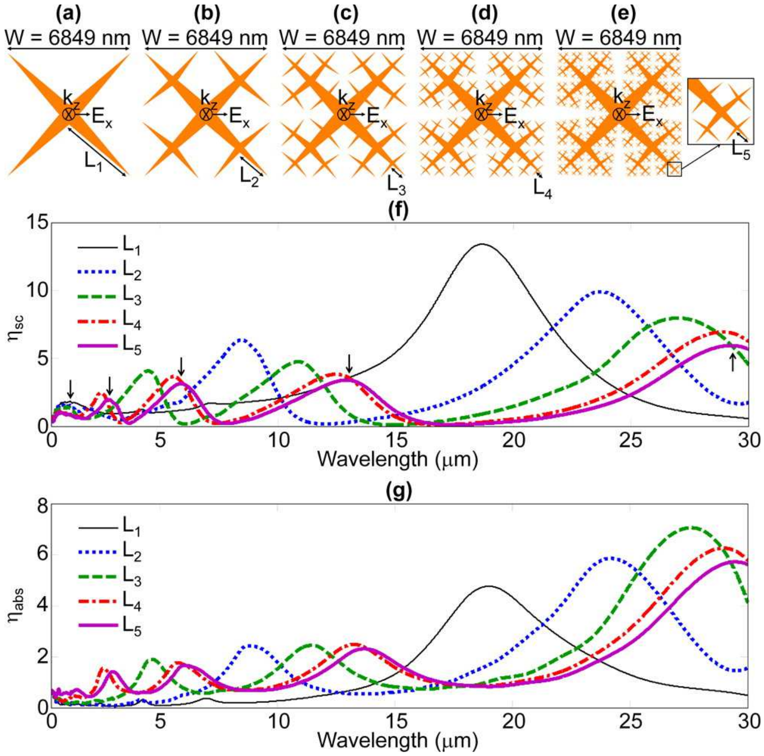

Figure 3·3: Dependence of the scattering and absorption cross sections on the fractal generation. By each one-step increase of the fractal generation with keeping the unit cell area constant, a new higher frequency resonant mode emerges. Top view of the (a) 1st, (b) 2nd, (c) 3rd, (d) 4th, and (e) 5th iteration of inverse Cesaro fractals. Ln (n: iteration number) indicates the smallest feature size for the corresponding nth iteration, and W indicates the width of the fractal nanoantennas. The spectral normalized (f) scattering cross section sc and (g) absorption cross section abs to the surface area of the nanoantenna for each iteration. In scattering and absorption spectra, lines are labeled by the smallest feature sizes of each iteration, which are $L_1 = 4470nm$, $L_2 = 2056nm$, $L_3 = 946nm$, $L_4 = 435nm$, and $L_5 = 200nm$. (Aslan et al., 2016)

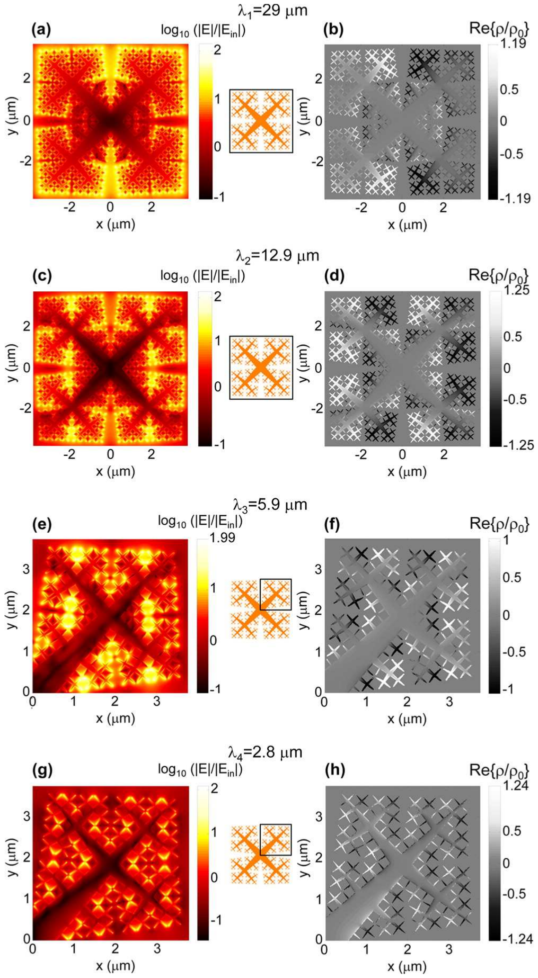

Figure 3·4: Near E-field and charge density properties of 1st to 4th order resonant modes for 5th generation fractal nanoantenna with L5 = 200 nm under x-polarized light. (a, c, e, g) E-field enhancement $|E|/|Ein|$ and (b, d, f, h) normalized charge density $Re[/_0]$ distributions on the top surface of structure for (a, b) 1st ($\lambda_1 = 29\mu m$), (c, d) 2nd ($\lambda_2 = 12.9\mu m$), (e, f) 3rd ($\lambda_3 = 5.9\mu m$), and (g, h) 4th ($\lambda_4 = 2.8\mu m$) order modes, respectively. The antenna figures with zoom boxes between the panels specify the spatial distribution region that panel couples represent. Corresponding resonant wavelengths are given on top of the E-field enhancement plot and charge density plot couples. Electric field enhancement plots are given in log scale, and normalized charge density plots are given in linear scale. (Aslan et al., 2016)

3.2 Radiative properties of diffractively-coupled optical nano-antennas with helical geometry

Metallic nanostructures with helical shapes feature a broad spectrum of interesting radiation and polarization characteristics that can largely be controlled by varying their geometrical parameters (Balanis, 2005). In the field of plasmonics (Brongersma and Kik, 2007; Maier, 2007), there have been many studies focusing on the dichroic properties of metal nano-helices excited using light with circular polarization (Song et al., 2013; Gibbs et al., 2013; Kuzyk et al., 2012; Gansel et al., 2010; Radke et al., 2011; Gansel et al., 2009). As the helix is a chiral shape, meaning that it cannot be superimposed to its mirror image, plasmonic nano-helices have chiral properties that make light-matter interaction sensitive to the handedness of circularly polarized radiation. In particular, differential scattering and absorption of left- and right-circularly polarized light, which is known as circular dichroism, have been demonstrated using plasmonic nano-helices in the visible and infrared spectral range (Mark et al., 2013; Liu et al., 2014). However, most of the structures mentioned in these studies have sub-wavelength dimensions and their properties have been investigated only over a limited range of geometrical parameters with respect to the optical wavelength. In addition, the plasmonic behavior of nano-helices is often captured by considering their optical transmittance or scattering/extinction cross-sections, which fail to reveal the rich angular scattering and directivity properties that are unique to the nano-helices. As a result, it is very interesting to systematically explore the directional scattering of plasmonic nano-helices in the diffractive regime, where their geometrical features are comparable to the wavelength of light. Using the rigorous Surface Integral Equation (SIE) method (see 2.2.2), the far-field radiation characteristics of diffractively coupled gold (Au) nano-helices is systematically studied in the optical regime. By doing so, novel opportunities to achieve highly directional scattering along multiple directions, with controlled polarization states in the visible regime, can be demonstrated by engineering of their geometrical parameters. General design rules is also established, which can be utilized to engineer novel directional nano-antennas of great interest for the development of sensors and filters with unprecedented beam forming and polarization capabilities. The study focused on the excitation with linearly polarized plane waves that propagate along the helical axis. In this case, classical antenna theory (Balanis, 2005; Kraus, 1949; Kraus and Marhefka, 2001), which is valid in the limit of perfectly metallic (i.e., no losses) helical wires with infinitesimally small r, provides general guidelines on the choice of the geometrical parameters that give rise to different radiation patterns. However, due to the dispersive nature of the Au material in the visible regime, the axial modes supported by nano-helices at optical frequencies are qualitatively different from the classical antenna case (Balanis, 2005; Kraus, 1949; Kraus and Marhefka, 2001) and no longer have a well-defined circular polarization. Nevertheless, a class of thin-wire ($r = 10nm$) nano-helices is identified which support perfectly circularly polarized backward radiation lobes when their pitch is equal to one wavelength. Moreover, when Au wires with larger $r = 100nm$ are used, highly directional modes can be formed in the optical regime resembling the radiation patterns of the traditional (i.e., radio frequency) axial modes over a wide range of R and P values. The term quasi-axial modes is used to designate this class of highly directional (beaming) modes that are created in the optical regime, with various degrees of elliptical polarization, beyond the standard thin-wire approximation (Kraus, 1949; Kraus and Marhefka, 2001). The Surface Integral Equation (SIE) method (Harrington and Harrington, 1996; Hoffmann et al., 2009; Smajic et al., 2009; Forestiere et al., 2012) is used in the numerical study. In the SIE method the electromagnetic properties of scattering materials are replaced by equivalent surface electric and magnetic currents. The SIE method is computationally advantageous

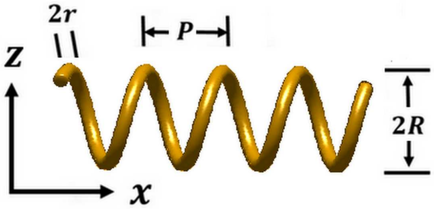

Figure 3·5: Definition of geometrical parameters of a helix. r is the radius of the cylindrical wire that forms the helix, R is the radius of the helix, and P is the pitch (separation between consecutive helical turns) of the helix. In this case, the number of helical turns shown is $N = 4$. The orientation of the nano-helix is such that its helical axis is parallel to the x-axis. (Wang et al., 2015)

since only surface discretization is required, and it is accurate for both the near-field and the far-field properties of general dielectric objects with realistic dispersions and complex shapes, such as the plasmonic nano-helices. In particular, the implemented SIE code used Poggio-Miller-Change-Harrington-Wu-Tsai formulation (PMCHWT) (Yla-Oijala and Taskinen, 2005) using the Rao-Wilton-Glisson (RWG) basis functions (Rao et al., 1982), and calculated the weakly singular integrals using the technique described in (Graglia, 1993). Besides, tabulated data for the optical constants of Au at each wavelength are used, as provided in (Johnson and Christy, 1972). In Fig. 3·5 the geometry of a representative nano-helical structure, which can be parameterized by the radius R of the helix, the helical pitch P, and the radius r of the cylindrical Au wire. The helix has a number of helical turns N, which together with R, P, and r define the set of the basic geometrical parameters that will be studied in the paper. As we will systematically discuss in this work, Au nano-helices feature vastly different radiation patterns and polarization characteristics of scattered plane waves depending on the values of their geometrical parameters with respect to the wavelength of light.

3.2.1 Scattering and radiation modes of single Au nanohelices

By considering an Au nano-helices pumped with a plane wave traveling along the positive x-direction, and linearly polarized in the positive z-direction (Fig. 3·6), the analysis by considering an incident wavelength across the visible spectrum ($\lambda_{exc} = 600nm$, and also $400nm$ and $500nm$ as an extension) is presented. By focusing on these representative wavelengths, a general picture is provided by this study to show how diffractively-coupled Au nano-helices interact with light in the visible spectrum. From classical antenna theory, helical antennas with sizes smaller than the wavelength produce isotropic radiation modes, called normal scattering modes, while larger helices with sizes comparable to the wavelength support highly directional modes called axial or beam modes (Kraus, 1949; Kraus and Marhefka, 2001). The formation of axial modes can be qualitatively understood based on a simple model (i.e., the array model) of a helical antenna. According to this picture, helical antennas are reduced to linear arrays of single-turn helical elements spaced by P. Axial modes then correspond to the end-fire radiation modes of such equivalent linear arrays. The conditions for the formation of normal and axial modes in radio frequency (RF) helical antennas have been studied in detail by Kraus (Kraus, 1949), who summarized his results by constructing a diagram, known as the Kraus diagram, which captures the effect of different geometrical parameters on the radiation properties of helical antennas. This diagram provides a sort of modal phase space that displays different radiation diagrams against the helical pitch $P\lambda$ and the circumference of the helical cross-section $\pi D\lambda$ ($D = 2R$), all scaled by the excitation wavelength λ_{exc}.

In Fig. 3·6, the calculated the Kraus diagram is shown, which corresponds to Au nano-antennas of helical shape with realistic dispersion data (Johnson and Christy, 1972) at $600nm$ and for different geometrical parameters. The wavelength scaling rules inspired by RF antenna theory are generally valid to approximate the scattering

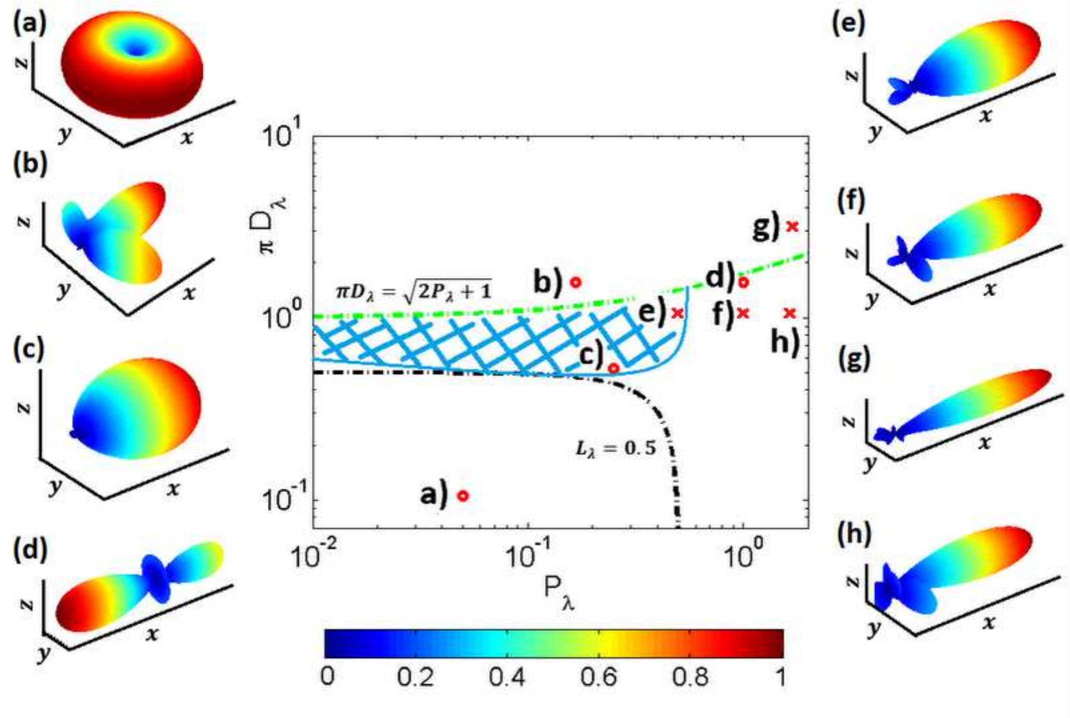

Figure 3·6: Representative radiation patterns of Au nano-helices and their corresponding positions in Kraus' diagram for RF helical antenna radiation patterns (Kraus, 1949; Kraus and Marhefka, 2001). Plane wave excitation at $\lambda_{exc} = 600nm$ is used. The region under the black dashed curve, where the length of one helical turn (L, where $L^2 = (\pi D)^2 + P^2$) is smaller than half of the wavelength, corresponds to radiation normal modes in Krauss diagram (Kraus, 1949; Kraus and Marhefka, 2001). The region shaded blue corresponds to the region of axial modes (Kraus, 1949; Kraus and Marhefka, 2001). Outside this region, higher order modes exist, with more complex radiation patterns. The Au nano-helices have $N = 4$, and: a) $R = 20nm$, $P = 30nm$, $r = 10nm$; b) $R = 300nm$, $P = 100nm$, $r = 10nm$; c) $R = 100nm$, $P = 150nm$, $r = 10nm$; d) $R = 300nm$, $P = 600nm$, $r = 10nm$; e) $R = 200nm$, $P = 300nm$, $r = 100nm$; f) $R = 200nm$, $P = 600nm$, $r = 100nm$; g) $R = 600nm$, $P = 1000nm$, $r = 100nm$; h) $R = 200nm$, $P = 1000nm$, $r = 100nm$.(Wang et al., 2015) behavior of thin-wire ($r = 10nm$) nano-helices in the visible spectral range. On the other hand, the results ($\lambda_{exc} = 600nm$) summarized in the diagram include cases for both thin-wire ($r = 10nm$) Au nano-helices (Figs. 3·6(a)-3·6(d), circles) and thick-wire ($r = 100nm$) nano-helices (Figs. 3·6(e)-3·6(h), crosses). The data clearly demonstrate the wide range of radiation patterns that can be achieved using Au nano-helices with different geometrical parameters. Moreover, we note that in the case of thin-wire nano-helices, classical RF antenna theory (Kraus, 1949; Kraus and Marhefka, 2001) qualitatively predicts the respective regions of the parameter space for normal modes and axial mode formation (Fig. 3·6). In particular, it is shown in Fig. 3·6(a), a calculated radiation diagram corresponding to a typical normal mode region (labeled (a) in the Kraus diagram), while in Fig. 3·6(c) the radiation diagram of a structure in a shaded region of the Kraus diagram where axial modes are predicted to exist by antenna theory. The radiation diagram in Fig. 3·6(c) consistently features a predominant radiation lobe in the forward direction. In addition, the radiation diagrams shown in Fig. 3·6(b) and Fig. 3·6(d), which correspond to helical structures with parameters outside the Kraus region of axial mode formation, do not feature directional radiation modes, in agreement with the prediction of classical antenna theory. Besides, the axial mode shown in Fig. 3·6(c) can simply be designed by following the well-known rules (Kraus, 1949; Kraus and Marhefka, 2001):

$$2\pi R \sim \lambda_{exc}, \tag{3.1}$$

and

$$P \sim \frac{\lambda_{exc}}{4}, \tag{3.2}$$

where λ_{exc} is the incident wavelength. However, marked deviations from the classical antenna theory begin to appear when we look at the polarization properties of the scattered radiation. The character of polarization for the radiated modes of helical antennas is captured by the axial ratio (AR), which is ratio of the semi-major axis to the semi-minor axis of the polarization ellipse of the radiated field. By this definition:$AR \in [1, \infty)$, with $AR = 1$ corresponding to perfectly circularly polarized radiation and $AR = \infty$ corresponding to linear polarizations. In the case of an N-turn helical antenna designed for increased degree of circular polarization in the axial mode (as from Eqns. 3.1 and 3.2), RF antenna theory predicts a simple scaling of the axial ratio given by (Kraus and Marhefka, 2001):

$$AR = \frac{2N+1}{2N}. \tag{3.3}$$

By applying this design rule to the radiation pattern in Fig. 3·6(c), nearly perfect circularly polarized light is expected in the forward direction, with $AR = 1.125$ ($N = 4$). However, the actual value of AR, which we calculated numerically by considering the realistic dispersion data for Au and the geometrical parameters of this Au nano-antenna, is about 10.5 and the directionality of the radiation pattern of the axial modes is very poor. Figure 3·6 also includes results obtained on a group of helices with thicker Au wire radius of $r = 100nm$ and have found that such helical structures produce radiation patterns with very good directionality (Figs. 3·6(e)-3·6(h)). These high-directivity modes are referred to as quasi-axial modes since they are obtained in the optical regime using thick Au wires with realistic dispersion properties. Interestingly such modes, which are qualitatively very similar to the axial modes of RF antenna theory, cannot be obtained using thin wires in the optical regime. These quasi-axial modes provides very good directionality even outside the axial mode region of Kraus diagram (see Fig. 3·6) and that they can be excited in a large range of either R (Figs. 3·6(h)-3·6(g)) or P (Figs. 3·6(e)-3·6(f)) values. Finally we remark that this group of nano-helices do not support normal scattering modes since, due to their much thicker wire radius, their overall size is comparable to the wavelength of light

(Collings, 2002). This study clearly demonstrates that classical antenna theory, even when augmented by wavelength scaling arguments (Novotny and van Hulst, 2011), can only serve as a qualitative guideline for the design of optical nano-antennas with complex shapes and strongly dispersive materials. As a result, there is a compelling need to embark in a systematic numerical study of the scaling properties of thin-wire and thick-wire Au helical nano-antennas with geometrical parameters comparable to the optical wavelength. In the next subsections the design rule to get circular polarization is summarized.

3.2.2 Polarization control of Au nanohelices

In this subsection, the effect of the geometrical parameters on the polarization states of nano-helices is presented. As discussed previously, quasi-axial modes with pronounced forward lobes are obtained for a large range of geometrical parameters, R and P, when the radius of the wire r is large ($r = 100nm$). However, the general polarization state of quasi-axial modes is elliptical, with different degrees of eccentricity. Similarly, the forward lobes of other cases of Au helical nano-antennas with thinner wires are all found to be elliptical to various degrees. These behavior results from the losses associated to the dispersion of Au in the visible regime. To overcome this limitation, we consider thin-wire helical nano-antennas, and identify the special conditions that allow us to obtain perfect circular polarization scattering.

We focus now on the radiation patterns that are supported by structures with small r and a pitch equal to one wavelength, excited using linearly polarized plane waves directed along the helical axis. In this particular case, backward lobes with perfectly circularly polarized radiation can be obtained when $P = \lambda$. Moreover, these structures feature radiation patterns with circularly polarized radiation in the backward lobe, while showing elliptically polarized forward lobes. This interesting phenomenon is analogous to the selective reflection of light by chiral liquid crystals,

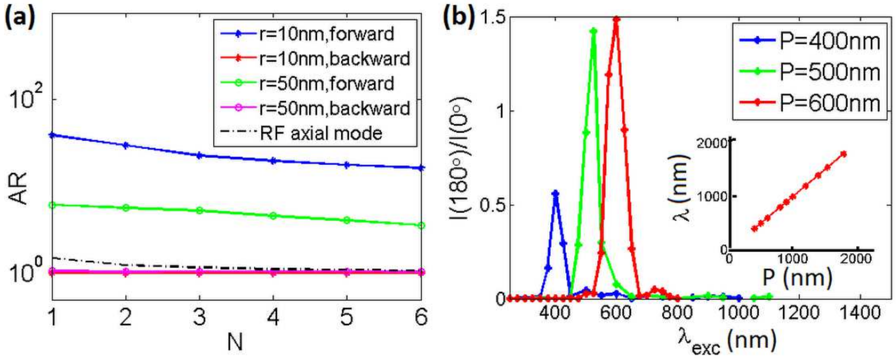

Figure 3·7: (a) The axial ratio (AR) of the forward lobe (blue) and the backward lobe (red) by Au nano-helices with $R = 300nm$, $P = 600nm$, $r = 10nm$, and of the forward lobe (green) and the backward lobe (pink) by Au nano-helices with thicker wire of r = 50nm. The results are plotted against increasing N. The black dashed curve is the theoretical value of AR for axial mode helix, calculated as $AR = (2N + 1)/(2N)$. (b) The relative intensity of the backward lobe to the forward lobe as a function of wavelength. Fixed $R = 300nm$, $r = 10nm$ and $N = 4$. The inset shows the wavelength and pitch at which the backward lobe with perfect circular polarization is obtained, in the case of Au nano-helices with fixed $r = 10nm$, $R = 300nm$, and $N = 4$. (Wang et al., 2015) which occurs when the pitch of the chiral liquid crystal is equal to the wavelength of normally incident light (Collings, 2002; Warner and Terentjev, 2003). In Fig. 3·7(a), the calculated AR values are shown for both the back and forward scattered lobes of this interesting class of nano-helices as a function of N for two different wire thicknesses of Au nano-helices. In particular, the AR values of backward lobes with $r = 10nm$ (red) overlap with the corresponding cases with $r = 50nm$ (pink), and are identically equal to one. In the figure the theoretical AR values calculated according to RF antenna theory for the axial-mode (black dotted line) are also plotted. These results demonstrate that, for thin-wire Au nano-helices with pitch equal to one wavelength, the AR of the backward lobe can be well-below the RF limit of axial modes supporting perfectly circular polarization states. As shown in Fig. Fig. 3·7(a), even with a thicker wire of $r = 50nm$, there is still a reflection of circularly polarized light in the backward direction. Therefore, significant reflection of circularly polarized light can be achieved even with a thicker Au wire diameter ($2r = 100nm$), which can easily be achieved using current fabrication techniques (Song et al., 2013; Gibbs et al., 2013; Kuzyk et al., 2012; Gansel et al., 2010; Radke et al., 2011; Gansel et al., 2009). Figure 3·7(a) also shows that the AR of the forward lobe decreases with increasing number of turns, i.e., the polarization states in the forward direction are more circular. However, as mentioned, for helical nano-antennas with realistic Au dispersion data, the polarization states that can be achieved in the forward direction are always far from ideal circular polarization. Furthermore, in Fig. 3·7(b), the bandwidth of the circularly-polarized backward lobe is also shown. The wavelength of the incident light is varied in the optical and near-infrared regime for Au nano-helices with three different pitches equal to the wavelength of blue ($400nm$), green ($500nm$) and red ($600nm$) light. The data clearly indicate that the circularly polarized backward lobe can only be obtained when the wavelength is close to one helical pitch, with a bandwidth (Full Width at Half Maximum, FWHM) that is roughly $50nm$ around the central wavelength. The calculated results agree well with the analogous case observed in chiral liquid crystals, where a single reflection bandgap is created when the wavelength equals one helical pitch . The inset of Fig. 3·7(b) demonstrates that, for diffractively coupled Au nano-helices, the condition to obtain circularly polarized backward lobe ($P = \lambda$) can be extended from the visible to the near-infrared regime.

3.2.3 Section summary

Based on the rigorous SIE method, I have completed a systematic study of the radiative properties of single diffractively-coupled Au nano-helices in the optical regime. When the wire radius is small, we have found a variety of highly directional radiation patterns depending on the ratio of P and R with respect to the incident wavelength. For this class of Au nano-helices, RF antenna theory provides a good guide to find the regions in the parameter space (Kraus diagram) for normal and axial modes. However, due to the dispersive nature of Au in the optical regime, axial modes no longer produce circularly polarized radiation. On the other hand, when $P = \lambda$, radiation modes are found that support perfectly circularly polarized light. The radiated intensity in both forward and backward directions become comparable when the wire radius is thin. However, as the radius of the helical wire increase, radiation properties start to deviate from the RF antenna theory. Au nano-helices with R and P comparable to the incident wavelength are found to operate in the quasi-axial modes when their wire radius is large ($r \simeq 100nm$). In quasi-axial modes, most of the radiated energy is directed forward along the helical axis, and the polarization of radiation in the forward direction are always elliptical with various degrees of eccentricity. Based on these results, engineering nano-helical antennas in the visible regime with multi-directional operation can be realized with thin-wire ($r = 10nm$) nano-helices with

R and P comparable to the wavelength. In this case, the radiation pattern is very sensitive to the values of geometrical parameters R and P, and the number of elliptically polarized forward lobes in the equatorial plane is proportional to $R\lambda$. Besides, when P is equal to one wavelength, the backward lobe at $180\circ$ is perfectly circularly polarized with the same handedness as the nano-helix. These radiation properties can be achieved with as little as 2 to 6 number of helical turns. This effect of diffractive coupling of nearby identical elements shows the importance of modeling the radiative properties of nanohelices as results of collective resonances in terms of arrays. Also, we have found that we can achieve this behavior with a thicker wire of r up to around $50nm$. Furthermore, it is found that the resonant condition $P = \lambda$ for circularly polarized backward lobe is general and can be extended to near-IR regime. A more detailed version of these results are presented in my publish paper (Wang et al., 2015). These results are important as they provide novel opportunities for the design of nano-helical antennas that can be used to engineer sensors, filters and plasmonic components with unprecedented beam forming and polarization capabilities in the optical and near-infrared spectral range. Furthermore, single metallic nanohelices can be used as elements of more complex deterministic aperiodic arrays (see Chapter 4.1 for more detailed introduction) for novel optical properties.

3.3 Optimization of large-scale Vogel spiral arrays of plasmonic nanoparticles

Although nanohelices feature a variety of radiation properties, its elements, single helical turns, are both difficult to model and fabricate. On the contrary, complex arrays formed by point patterns provide more simplicity and flexibility in design through decoupling of complexcity of array and simplicity of elements. Our group has been pioneering in the study of complex aperiodic arrays called Vogel spiral (Lawrence et al., 2012a; Capretti et al., 2012; Lawrence et al., 2012b; **?**; Christofi et al., 2016), which is a family of distinctive 2D geometries. As will be introduced in more detail in the next chapter, Vogel spirals are generated by only two geometric parameters, but has complex rotationally symmetric diffraction pattern. As a result, the class of Vogel spirals is ideal for optimization problems aimed to inversely engineer large-scale devices. In the following subsections, I show how large Vogel spiral plasmonic arrays are optimized for scattering and absorption efficiencies.

3.3.1 Motivation for the array optimization problem

Recent progress in plasmonics and metamaterials driven by the continuing advancements in nanofabrication technology motivates the need to develop efficient and accurate simulation approaches for the design of large-scale arrays of resonant nanoparticles. However, the engineering of complex nanoplasmonic structures poses severe difficulties due to the large number of degrees of freedom and the difficulties in solving the multiple scattering problem for a large number of resonant nanoparticles. In particular, plasmonic inverse scattering requires the coupling of efficient optimization codes with full-wave electromagnetic solvers of high numerical accuracy that enable the evaluation of precisely-defined objective functions to achieve optimal designs. Our previous work introduced a rigorous approach based on Surface Integral Equation (SIE) coupled to optimization codes, and used analytical formula to describe different particles' shapes and reduce the parameter space for the morphology optimization (Forestiere et al., 2016). While in one of my previous work we targeted the optimization of the near-field properties of individual nanoparticles (Forestiere et al., 2016), the present work addresses the design of the far-field properties of large-scale nanoparticle arrays. In order to improve the efficiency of the approach we consider here the case of sub-wavelength nanoparticles that can be accurately described within the limits of the coupled dipole approximation (CDA) (Zhao et al., 2003; Yang et al., 1995). This choice, applied to the vast category of structures known as Vogel spiral arrays, enables efficient surveying of a large number of complex arrays and the rapid identification of best configurations resulting in optimal scattering and absorption efficiencies. Vogel spiral arrays are a two-parameter class of two-dimensional (2D) systems with vastly varying geometrical configurations, and have been shown to manifest rich scattering properties of interest to a variety of device applications in plasmonics and photonics (Pollard and Parker, 2009; Guo et al., 2017; Trevino et al., 2012a; Trevino et al., 2012b; Lawrence et al., 2012a; Dal Negro et al., 2016; Christofi et al., 2016; **?**). An N-particle Vogel spiral is specified by only two scalar parameters, the scaling factor a_{vs} and the divergence angle α_{vs}, that uniquely determine the $2N$ coordinates (x and y positions) of the nanoparticles in the Vogel array. In section, I introduce the study on Vogel spirals systems composed of sub-wavelength gold (Au), silver (Ag), and aluminum (Al) nanospheres, and identify array geometries for optimal scattering and absorption efficiencies using an efficient cyclic coordinate minimization algorithm (Saha and Tewari, 2013) coupled to CDA electromagnetic field computation (Trevino et al., 2012a). This work does not only demonstrate the capabilities of the proposed approach, but it also provides applicable design rules for the engineering of large-scale plasmonic structures with optimal absorption or scattering properties that are relevant to the engineering of photonic-plasmonic devices such as optical sensors, photodetectors, solar-cell components, random lasers, and more efficient nonlinear optical elements.

3.3.2 The coupled-dipole approximation method

The coupled dipole approximation (CDA) is a framework for the efficient modeling of the optical response of a collection of identical scatterers that are approximated as vectorial electric dipoles. The method is equivalent to the rigorous self-consistent solution of the multiple scattering equations for the case of nanospherical particles with small dimensions compared to the wavelength of the exciting radiation (Zhao et al., 2003; Yang et al., 1995; Guerin et al., 2006; Christofi et al., 2016). Nonmagnetic metallic nanospheres with sizes much smaller than the wavelength of light respond primarily with an electric dipole component to the driving local fields. Moreover, as long as the nanospheres in the arrays are not spaced too closely (this work constrains their edge-to-edge separation to be larger than $d_e > 25$nm and validate this choice using the more accurate multipolar theory (**?**)), the response of a plasmonic array to electromagnetic radiation can be accurately determined by the self-consistent solution of the local electric fields, $E_{loc}(r_i)$ of each ith sphere induced by the incident light $E_0(r_i)$ as well as the the scattered fields of the other particles in the array. Thus, considering N metallic particles described by the same volumetric polarizability $\alpha(\omega)$ located at vector positions r_i, we can express the local field $E_{loc}(r_i)$ as (Guerin et al., 2006):

$$\mathbf{E}_{loc}(\mathbf{r}_i) = \mathbf{E}_0\mathbf{r}_i + \frac{\alpha k^2}{\epsilon_0}\sum_{j=1,j\neq i}^{N}\mathbf{G}_{ij}\mathbf{E}_{loc}(\mathbf{r}_j), \tag{3.4}$$

where $\mathbf{E}_0(r_i)$ is the incident field in vector form, k is the wavenumber in the background medium, ϵ_0 is the dielectric permittivity of vacuum ($\epsilon_0 = 1$ in CGS unit system), and $\mathbf{G}_{ij}$ is the 3×3 block of the overall $3N \times 3N$ Green's matrix for the ith and jth particles and the summation runs through all jth particles except for $j = i$. In particular, the 3×3 $\mathbf{G}_{ij}$ is a zero matrix when $j = i$, and is otherwise computed as (Guerin et al., 2006; Christofi et al., 2016; Dal Negro et al., 2016):

$$\mathbf{G}_{ij,i\neq j} = \frac{\exp(ikr_{ij})}{r_{ij}}\{\mathbf{U} - \hat{\mathbf{r}_{ij}}\hat{\mathbf{r}_{ij}} - [\frac{1}{ikr_{ij}} + \frac{1}{(kr_{ij})^2}(\mathbf{U} - 3\hat{\mathbf{r}_{ij}}\hat{\mathbf{r}_{ij}})\} \tag{3.5}$$

where $\hat{\mathbf{r}_{ij}}$ is the unit position vector from jth to ith particle, and $r_{ij} = |\hat{\mathbf{r}_{ij}}|$. $\mathbf{U}$ is the 3×3 identity matrix. Besides, the polarizability is computed using the retarded Clausius-Mossotti relation

$$\alpha = \alpha_0 a^3 F \tag{3.6}$$

with

$$\alpha_0 = \epsilon_b \frac{\epsilon_r - 1}{\epsilon_r + 2}, \tag{3.7}$$

where ϵ_b is the background medium's relative dielectric permittivity, ϵ_r is the relative dielectric permittivity of nanospheres with radius a, and F is the factor for Modified Long Wavelength Approximation (MLWA) (Zeman and Schatz, 1987) that ensures more accurate results in the presence of field retardation:

$$F = (1 - \frac{2k^3\alpha_0}{3} - \frac{\alpha_0 k^2}{a})^{-1}. \tag{3.8}$$

Solving the $3N \times 3N$ linear system of equations (3.4), the total local fields, $\mathbf{E}_{loc}(r_i)$ can be obtained and the local electric dipole polarizations across the array can be directly constructed by $\mathbf{P}_{loc}(r_i) = \alpha \mathbf{E}_{loc}(r_i)$. Once the polarizations are know, the extinction and absorption cross-sections σ_{ext} and σ_{abs} respectively, can be computed using the well-known expressions (Zhao et al., 2003; Yang et al., 1995):

$$\sigma_{ext} = \frac{4\pi k}{|\mathbf{E}_0|^2} \sum_{j=1}^{N} Im\{(\mathbf{E}_0(r_j))^* \cdot \mathbf{P}_j\} \tag{3.9}$$

and

$$\sigma_{abs} = \frac{4\pi k}{|\mathbf{E}_0|^2} \sum_{j=1}^{N} \{Im[\mathbf{P}_j(\alpha_j^{-1})^*(\mathbf{P}_j)^*] - \frac{2k^3|\mathbf{P}_j|^2}{3}\}. \tag{3.10}$$

Using the optical theorem, the scattering cross-section can be calculated as:

$$\sigma_{sc} = \sigma_{ext} - \sigma_{abs}. \tag{3.11}$$

Once the scattering and absorption cross-sections are computed, they are normalized with respect to the total projected area of the array (i.e., sum of the areas of the particles projected perpendicularly to the direction of the excitation beam) in order to achieve the scattering (Q_{sc}) and absorption (Q_{abs}) efficiencies. These dimensionless quantities can be compared for different arrays and provide the quantitative metrics for this optimization. Finally, dispersion data for realistic materials are used according to references (Johnson and Christy, 1972) (for silver and gold) and (McPeak et al., 2015) (for aluminum).

3.3.3 Optimization approach

The purpose of the optimization in the present work is to obtain the optimal Vogel Spiral configurations that produce the maximum absorption (Q_{abs}) or scattering efficiency (Q_{sc}) for a fixed number of dipolar nanoparticles. The optimization takes into account the average of the scattering and absorption cross-sections calculated considering the two orthogonal linear polarizations of a normally incident plane wave. For this purpose, a Fortran code was developed based on the coupled-dipoles approximation (CDA) theory and coupled to the optimization algorithm, which is performed at Prof. Kirby's group at the University of Utah. In this approach, the cost of computation scales with the number of scatterers. The design variables for the optimization are the incident wavelength λ, the divergence angle α_{vs}, and the scaling factor a_{vs} that uniquely specify the Vogel spiral geometry for a fixed number of particles, according to (Christofi et al., 2016; **?**):

$$\rho_n = \sqrt{n} a_{vs}, \tag{3.12}$$

$$\theta_n = n\alpha_{vs}, \tag{3.13}$$

where ρ_n and θ_n denote, respectively, the radial distance and the polar angle of the n-th particle in a Vogel spiral array.

In this optimization, the radius of the particles is set to be fixed at $25nm$, which guarantees the validity of the CDA approximation when additionally combined with the constraint that the particles center-to-center separation (d) is restricted to be larger than $75nm$. In order to produce the optimal configurations with a reasonable computational efficiency, a greedy optimization algorithm is used, which is known as cyclic coordinate optimization, uses one-dimensional particle swarm optimization for each dimension (with all other variables being held fixed in each step) to find the optimal value for all design variables in a step by step computational process. Next, a pattern search strategy is used to optimize the array of particles configuration in the direction of incrementation of all design variables from their old to new values. Then the greedy loop is repeated again with the newly found values of the design variables until the selected objective function (either $f = -Q_{abs}$ or $f = -Q_{sc}$) minimum is equal to the previous step minimum value within a specified tolerance (here $\varepsilon = 10^{-3}$). It should also be noted that the constraint of center-to-center distance $d \geq 75$ nm is imposed using a penalty step function, in order to avoid excitation of higher order modes other than electric dipole moments in the nanoparticles (which destroy the validity of dipole approximation).

Cyclic coordinate or block coordinate descent minimization approaches have been used in different areas of science and engineering such as statistics (Breheny and Huang, 2011), image processing (Bouman and Sauer, 1996; Ye et al., 1999), machine learning (Hsieh et al., 2008), compressive sensing (Wu and Lange, 2008; Kyrola et al., 2011) and dynamic programming (Zuo and Wu, 1989). The reason behind this broad range of applications is its ease of implementation and numerical stability as well as its reasonable convergence speed due to its low computational cost for each iteration. In this context, Saha and Tewar have provided a convergence analysis for one of this approach called cyclic coordinate descent method (Saha and Tewari, 2013). Under Lipschitz continuity and strong convexivity assumptions for the objective function, they proved that the convergence rate of this variant of cyclic coordinate minimization to be of the order of $\frac{1}{k}$, for which k is the iteration count. Such a convergence is ideal for dealing with the optimization problems of large dimension. This deduction has been confirmed in the work of Friedman et al (Friedman et al., 2010). A

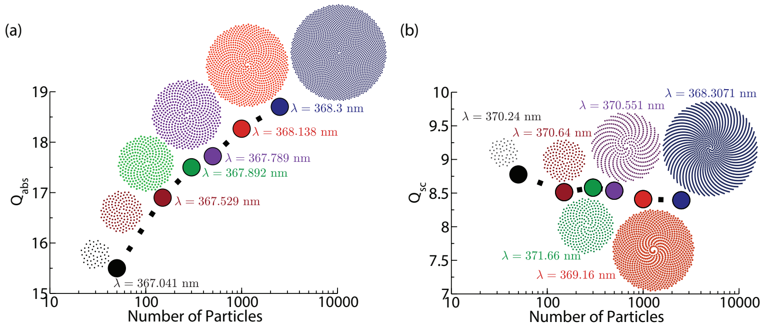

Figure 3·8: Optimal Vogel Spiral with respect to (a)Q_{abs} (b)Q_{sc} within 5 percent of highest found value; Silver(Razi et al., 2018)

comprehensive overview of the coordinate descent algorithms has been provided by Wright (Wright, 2015). In the present work, a combination of a one-dimensional heuristic approach with cyclic coordinate algorithm provides a cost effective tool to study the optimal configurations of Vogel spirals with hundreds to thousands of particles, for which the computational cost of each sample data can be significantly high.

3.3.4 Results and discussion

The absorption and scattering efficiencies are important quantities in the study of nanoparticle arrays and quantify their ability to efficiently couple with the incoming radiation, which is a desired feature for a number of different engineering applications. In this section, we discuss the results of the optimization of Vogel spiral arrays with respect to the absorption/scattering efficiency. The results of optimal configurations will be provided in this section for three types of commonly utilized plasmonic materials, namely silver, aluminum and gold. Moreover, the optimal arrays' configurations, which are shown in Figs 3·8, 3·10 and 3·12, are found for different numbers of particles ($N = \{50, 150, 300, 500, 1000, 2500\}$).

It should be noted that these optimal arrays were selected among a small set of arrays, which are all obtained as a design space local optima, with at most 1 to 5 percent variations in the values of absorption/scattering efficiency. In order to show

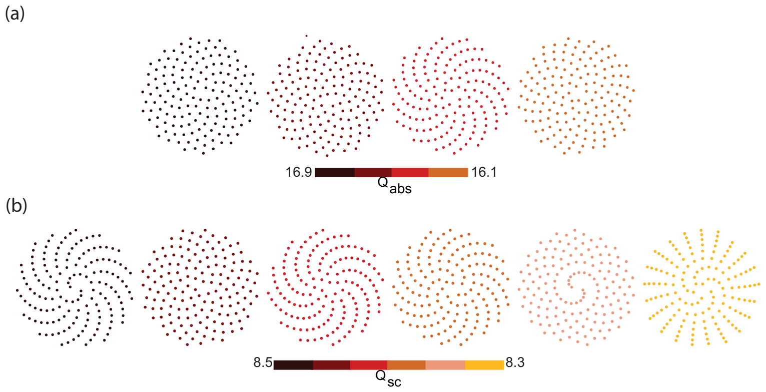

Figure 3·9: Set of optimal Vogel Spirals with respect to (a)Q_{abs} (b)Q_{sc} within 5 percent of highest found value; Silver; $N = 150$ (Razi et al., 2018)

the geometrical diversity of such set, a corresponding group of silver, aluminum and gold arrays are illustrated in Figs 3·9, 3·11 and 3·13. Within these sets of configurations, many geometrically different configurations can be found. Among them, the most consistent configurations in the range of $50 \leq N \leq 2500$ are selected as the optimal configuration. As shown in Fig. 3·8(a), the optimal Q_{abs} increases with the number of particles for silver. In contrast, the optimal scattering efficiency appears to be insensitive to the number of particles in the corresponding optimal Vogel spiral arrays (see Figs 3·8(b)). This difference is due to the fact that the scattering cross-section increases with overall area whereas the absorption cross-section increases with the volume. Therefore, the scattering efficiencies are expected to weakly depend on the number of particles since they are normalized to the total projected area of each array, which compensates for the absolute increase in the scattering cross-sections. On the other hand, we found that the absorption efficiencies follow a linear trend proportional to the linear size of the system (i.e., the particle number). Besides, we show that the optimal wavelength remains approximately constant among these optimal configurations for silver, indicating that the different optimal geometries only slightly perturbs the scattering/absorption resonant wavelength of the individual sil-

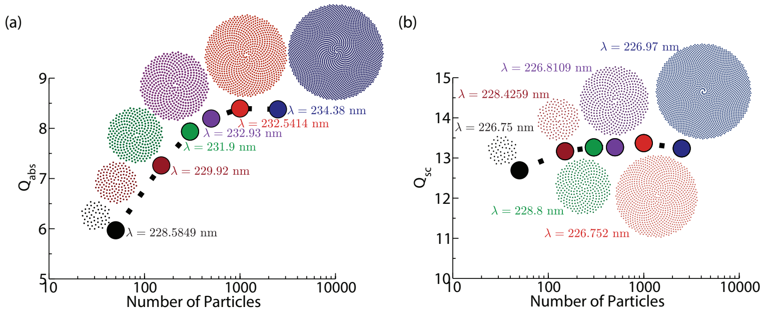

Figure 3·10: Optimal Vogel Spiral with respect to (a)Q_{abs} (b)Q_{sc} within 5 percent of highest found value; Aluminum (Razi et al., 2018)

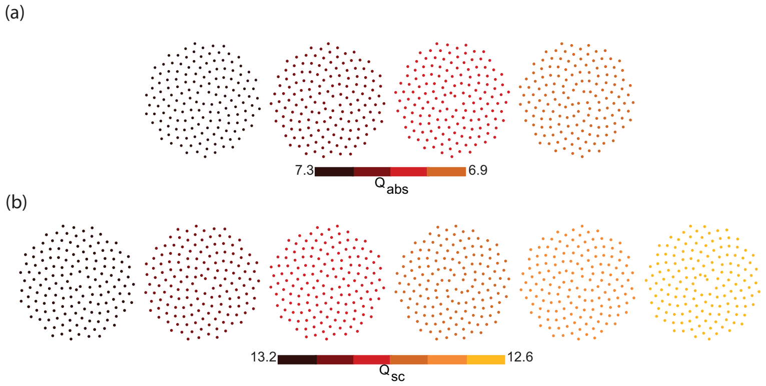

Figure 3·11: Set of optimal Vogel Spirals with respect to (a)Q_{abs} (b)Q_{sc} within 5 percent of highest found value; Aluminum; $N = 150$ (Razi et al., 2018)

ver nanospheres. We notice that, for Vogel spirals formed by silver nanospheres, densely-packed arrays of similar geometrical configurations can be observed at different particle numbers. This is so because in this study we selected optimal array configurations with similar morphology across a wide range of N. It is interesting to note that among the selected optimal configurations, few arrays can be found with a distinctive chiral structure, as shown for example in Figs 3·8(b). However, if we consider the arrays geometries of all the optimal solutions illustrated in Fig. 3·8, we can appreciate that Vogel spirals with approximately the same structure are obtained across a large range of particles numbers, i.e., in the range of $50 \leq N \leq 2500$. Moreover, from these results one can learn that the optimal Vogel spiral arrays con-

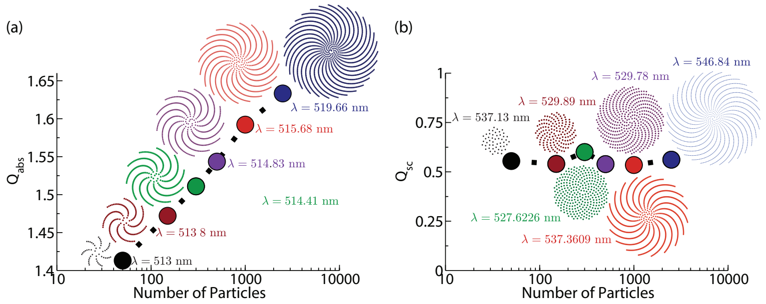

Figure 3·12: Optimal Vogel Spiral with respect to (a)Q_{abs} (b)Q_{sc} within 5 percent of highest found value; Gold (Razi et al., 2018)

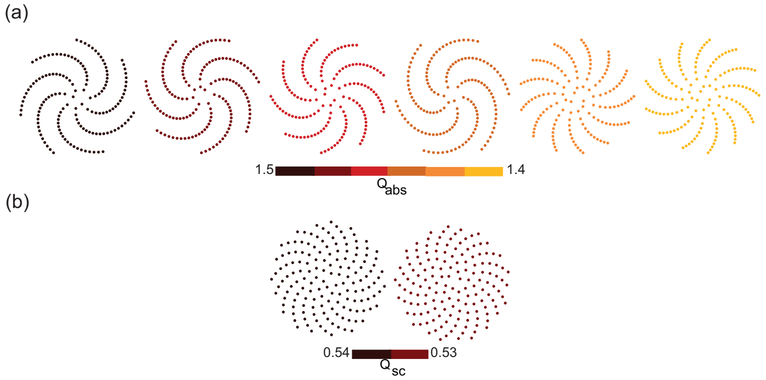

Figure 3·13: Set of optimal Vogel Spirals with respect to (a)Q_{abs} (b)Q_{sc} within 5 percent of highest found value; Gold; $N = 150$ (Razi et al., 2018) sist of evenly distributed silver nanospheres. The underlying physical reason for this behavior observed in arrays of silver nanospheres with $25nm$ radius, which are very effective at scattering the incoming radiation, is that evenly distributed nanoparticles separated by approximately the resonance wavelength produce the most efficient scattering within a given circular region. The optimization is however very sensitive to the geometrical parameters of the arrays. In fact, if we relax the optimal scattering/absorption efficiencies to be within 5% from the maximum, we obtain a larger number of chiral geometries within the class of the best results. Figure 3·9 shows a representative set of optimized arrays with 150 nanoparticles that are all within 5% of the optimal solution for absorption/scattering efficiencies. In the case of aluminum nanoparticles, shown in Fig. 3·10(a), the values of optimum Q_{abs} exhibit a linearly increasing trend as the number of particles is increased, whereas Q_{sca} remains mostly constant (see Fig. 3·10(b)). Similar to the case of silver nanoparticles, the optimal incident wavelength, as shown in Fig. 4·15, remains almost constant and very close to the value of the scattering/absorption peak of an isolated nanosphere. This situation is consistent with the regime of photonic coupling of the arrays where each particle is maximally excited by the coherent diffracted (far)-fields from all the other particles with only a small perturbation due to the near-field coupling. As efficient scatterers, optimal structures for both scattering and absorption efficiencies all feature very uniform particle distributions in the circular area occupied by each Vogel spiral. Being a better scatterer than the same-sized silver nanospheres, aluminum Vogel spirals all optimize to evenly distributed (over the wavelength scale) structures even when the condition for optimization is relaxed to be within 5% of the best result (see Fig. 3·11). Analogously to the case of silver and aluminum Vogel spiral arrays, optimal gold arrays show increasing trends with respect to absorption efficiency, and almost constant scattering efficiencies as the number of particles is varied in Fig. 3·12. However, the optimal values of absorption efficiencies for gold are much lower, and the scattering efficiencies show values that are constantly below unity. This behavior follows from the more dissipative nature of gold material as opposed to silver and aluminum. The characteristic material dispersion of gold produces some important differences in the Vogel spirals optimization as compared to structures created using the other two materials. For instance, for the absorption efficiency, while the optimal silver and aluminum spirals provide evenly distributed structures over the wavelength scale resulting in strong diffractive coupling, optimal gold arrays feature closely-packed clusters of particles with sub-wavelength separation giving rise to stronger near-field coupling effects. These effects perturbs more severely the resonant wavelength position of the optimized arrays compared to the one of the isolated gold particles, as evident in Fig. 3·13. In addition, the presence of strong near-field coupling in gold relaxes the importance of the geometrical array configuration leading to the appearance of a broad distribution of optimal configurations that include chiral structures as well. For instance, Fig. 3·13 shows a set of optimal solutions with opposite chirality, while maintaining the important feature of closely-packed clusters of particles on the sub-wavelength scale. Since we have enforced a lower bound on the edge-to-edge distance in the optimization, the minimum separation between gold nanospheres across the spiral arms approaches this limit. Therefore the study suggests that the sub-wavelength coupling in gold arrays is the most effective strategy to maximize the amount of scattering per unit area, resulting in continuum-like large substructures (i.e., the arms of the spirals) that strongly couple diffractively. The interplay between materials dissipation and plasmonic coupling results for gold in a much reacher space of optimal structures as we increase the total number of particles in the arrays.

In summary, by comparing the optimized structures for the three investigated materials we can infer some general rules: (a) the materials that most efficiently scatter radiation are optimized into evenly distributed Vogel spirals where the particles are separated over the wavelength scale giving rise to strong diffractive coupling effects that drive optimal scattering and absorption; and (b) materials such as gold that have large dissipation produce arrays of closely-packed particles at the sub-wavelength scales that arrange into highly-diffractive spiral arms that drive optimal cross sections with a strong perturbation of the single particle's resonant condition.

3.3.5 Section summary

In conclusion, a greedy optimization algorithm based on cyclic coordinate minimization has been used, and coupled it with CDA codes to find optimal solutions for absorption and scattering efficiencies for the three most common plasmonic materials, within the family of Vogel spirals. Due to the differences in material dispersions, Vogel spirals made with these three materials optimize to very different array geometries. The general understanding is that, for better scattering materials, more evenly distributed arrays over the wavelength scale produce both better absorption and scattering efficiencies. On the other hand, lossy materials such as gold lead to spiral-armed Vogel arrays with closely-packed clusters of particles at the sub-wavelength scale, strongly perturbing the plasmonic resonance of the individual particles.

Given the significantly reduced parameter space using Vogel spirals and the capability of CDA to deal with large particle clusters, the proposed optimization approach can be utilized to design large complex systems up to 10000 particles. This is important for the engineering of large-scale photonic-plasmonic coupled devices, such as plasmon-enhanced sensors, photodetectors, solar-cells, light sources, and more efficient nonlinear optical elements.

3.4 Chapter Summary

In this chapter, I have shown how nanostructures based on the concept of arrays can both improve our understanding of collective resonances of nanostructures and enable designs for more complex resonance features. In particular, randomly arranged gold nanofiber in the electrodes for electrocatalysis different sizes and result in broadband reflectance. On the other hand, Cesaro-type fractal structures feature deterministic and controllable resonance elements at different length scales, and provide the basis for multiband sensing. While above two examples exploits resonances due to mixture of different resonant elements in the array, the array effect enable gold nanohelicies, which is modeled as periodic repetition of identical elements, to show emergent features such as directionality and circular polarization. As motivated by the example of gold nanohelices, as well as reasons for ease of fabrication and modeling, arrays made of identical elements become the focus of my research. By designing and modeling complex nanostructures using arrays of identical elements, we can decouple the understanding of single-element resonance from the effect of overall array geometries. In the next chapter, I will introduce the Green's matrix method as a tool to rigorously understand effects of arrays.

Chapter 4

Rigorous Engineering of Collectrive Resonances and The Green's Matrix Method of Coupled Dipoles

In the previous chapter, I have shown the relevance of engineering the geometry of arrays in order to achieve desired collective resonance that are not observed at single-element level. Anderson localization of light (Lagendijk et al., 2009), which leads to a breakdown of wave propagation in strongly scattering media, is probably the best known example that requires understanding of complex and disordered scattering media beyond single-element. As I have previously discussed, the applications of random media to optical engineering are presently quite limited due to the lack of simple design rules for deterministic optimization. As an alternative, aperiodic optical media, including quasi-periodic crystals constructed by following deterministic mathematical rules (Senechal, 1995), recently attracted significant interest in the optics and electronics communities because of their simplicity in design and fabrication, as well as compatibility with current material deposition and device fabrication technologies (Kohmoto and Kadanoff, 1983; Merlin et al., 1985; Kohmoto et al., 1987a; Maciá, 2006; Maciá, 2009; Maciá, 2012; Dal Negro, 2014). Indeed, a large amount of recent theoretical and experimental investigations in the communities for nanophotonics, plasmonics and metamaterials have focused on understanding structure-property relationships in complex media with aperiodic order for the demonstration of novel optical functionalities (Steurer and Sutter-Widmer, 2007; Dal Negro and Feng, 2007;

Forestiere et al., 2009b; Forestiere et al., 2009a; Ostfeld and Pacifici, 2011; Dal Negro and Boriskina, 2012; Vardeny et al., 2013; Barthelemy et al., 2008).

In particular, it has been demonstrated that deterministic aperiodic structures support distinctive optical properties and collective resonances which are absent in either periodic or random systems, such as fractal mode spectra with controllable anomalous transport behavior (Abe and Hiramoto, 1987; Ketzmerick et al., 1997; Dal Negro et al., 2003; Dal Negro and Inampudi, 2017), and a rich spectrum of optical modes that show various degrees of spatial localization, known as critical modes (Kohmoto et al., 1987b; Maciá and Domínguez-Adame, 1996; Boriskina and Dal Negro, 2008a). Critical modes feature highly fragmented multi-fractal envelopes with a power-law decay that found recent applications in aperiodic lasing, optical sensing, photo-detection, and nonlinear optical devices (Yang et al., 2010; Boriskina and Dal Negro, 2008b; Dal Negro and Boriskina, 2012; Albuquerque and Cottam, 2003; Dal Negro, 2014). Moreover, topologically protected edge-states were recently discovered in the pseudo-gap spectra of quasicrystals (Bandres et al., ; Baboux et al., 2017; Levy and Akkermans, 2017), significantly broadening our understanding of topological phases in optical media. However, the vast majority of previous studies focused on quasicrystalline structures that are constructed by local matching rules, such as the Penrose lattice, or on deterministic scattering arrays generated by binary inflation rules, of which the Fibonacci, Thue-Morse, and Rudin-Shapiro sequences are the primary examples (Abe and Hiramoto, 1987; Gellerman et al., 1994; Dulea et al., 1992; Bandres et al., ; Baboux et al., 2017; Levy and Akkermans, 2017; Dal Negro et al., 2005; Yang et al., 2010; Boriskina et al., 2008).

In this chapter, I focus on introducing my works related to rigorous understanding and engineering array-geometry effect on optical properties through the Green's matrix method of coupled dipoles. I first provide a brief overview of various classes of point patterns. Then, I introduce the Green's matrix method in the second section, and show how it can be applied to two dimensional systems in the third section. In particular, I use Green's matrix method to understand resonances in novel prime-based arrays and show the richness of structural and spectral information one can extract from studying the Green's matrix eigen-properties.

In the fourth section, I show how the Green's matrix method can be relevant to understanding topological properties of optical systems as a result of collective resonance. In particular, by using full electromagnetic interactions in the Green's matrix, we show that topological edge states are possible but with novel localization properties beyond the widely used tight-binding models.

Finally, by recognizing the fact that the vectorial Green's matrix is also the kernel of Foldy-Lax equation for multiple scattering of coupled electric dipoles, it is natural to ask the question on how Green's matrix method can be extended to include magnetic dipoles. From the point of view of designing metamaterial and optical nanostructures, it is also important to consider both electric and magnetic properties. For large nanoparticle as elements in the array, especially dielectric particles, induce magnetic dipole moment also becomes important in fully modeling the design problem. As a result, including magnetic dipoles in the coupled-dipole multiple scattering problem naturally extends the validity limit of the existing Green's matrix method from small particles with only electric dipolar response. In the final section of this chapter, I show how this can be done, and present a few representative results in comparison to those of vectorial Green's matrix with only electric dipoles.

4.1 Classification of point patterns

It has been shown from the previous chapter that modeling and designing optical structures and media as arrays provides a powerful paradigm, as it decouples the engineering of single-element properties from the engineering of collective resonances at the array level. Here, we use point arrays (or point patterns) to denote the union of Dirac delta points (i.e. infinitesimal in size and featureless) in Euclidean space (e.g. 1D, 2D, or 3D). A general point pattern can be mathematically defined as a density function (Baake and Grimm, 2013):

$$\rho(\mathbf{r}) = \sum_{n} \delta(\mathbf{r} - \mathbf{r}_n), \tag{4.1}$$

where δ is the Dirac delta function, $\mathbf{r}_n$ is the position vector of the n point in the array.

Traditionally, point arrays have been classified as either periodic or aperiodic, without the need of further distinctions. However, the word *aperiodic* envelops a very wide range of concepts which are useful to characterize complex structures of varying degrees of spatial correlations, ranging from quasiperiodic crystals to more disordered patterns with diffuse diffraction spectra. As a result, a better understanding of aperiodicity of point patterns is pertinent to engineering desired optical properties for nanostructures.

In order to distinguish various classes of aperiodic arrays it is informative to compute the spatial Fourier spectrum of the point array which is related to the farfield diffraction pattern of the point array (Baake and Grimm, 2013):

$$\hat{\rho}(\mathbf{q}) = \sum_{n} exp(-2\pi i \mathbf{r}_n \cdot \mathbf{q}), \tag{4.2}$$

where $\mathbf{q}$ values are the spatial frequency coordinates. Based on the spatial Fourier spectrum, the static structure factor (at each spatial frequency position $\mathbf{q}$) of an N-point array can be defined as (Baake and Grimm, 2013; Senechal, 1995):

$$S(\mathbf{q}) = \frac{1}{N} |\hat{\rho}(\mathbf{q})|^2. \tag{4.3}$$

In general, the static structure factor spectrum in the spatial frequency space, $S(\mathbf{q})$, can have both discrete (pure-point) and continuous parts (which can be further distinguished as singular continuous and absolutly continuous parts) (Queffelec, 2010; Senechal, 1995). From a more physical point of view, discrete spectral components give rise to sharp diffraction peaks while absolutely continuous measures are responsible for diffuse scattering. In particular, periodic and quasiperiodic arrays can have discrete Fourier spectra, where disordered random arrays typically have absolutely continuous spectra (Levine and Steinhardt, 1984; Shechtman et al., 1984). The remaining singular continuous component does not have a simple physical interpretation, has features in between discrete and absolutely continuous components.

In order to visually appreciate the different point arrays mentioned above, I show three representative arrays and their corresponding static structure factors in Figs. 4·1(a) to 4·1(f), for a regular square lattice, a quasiperiodic Penrose point pattern with decagonal rotational symmetry (Penrose, ; de Bruijn, 1981), and a random array (single realization). In particular, Fig. 4·1(a) is a periodic square array, and its structure factor is in Fig. 4·1(b) which is pure-point. Fig. 4·1(c) is a Penrose array. Unlike square array, it does not repeat periodically in translational directions, apart from a ten-fold rotational symmetry. Its structure factor in Fig. 4·1(d) is also discrete, which is characteristic to quasiperiodic point patterns. In contrast, the random point pattern consisting of uniformly distributed dipoles (without overlaps) in Fig. 4·1(e) has an absolutely continuous spectrum in Fig. 4·1(f) (apart from the central bright spot resulting from $\mathbf{q} = 0$ in Eq. 4.2).

As aperiodic point patterns can be designed to accommodate arbitrary rotational symmetries as well as more abstract types of group symmetries, studying of their aperiodic Fourier space becomes particularly attractive to optical engineering applications where isotropic and polarization insensitive responses are of great interest.

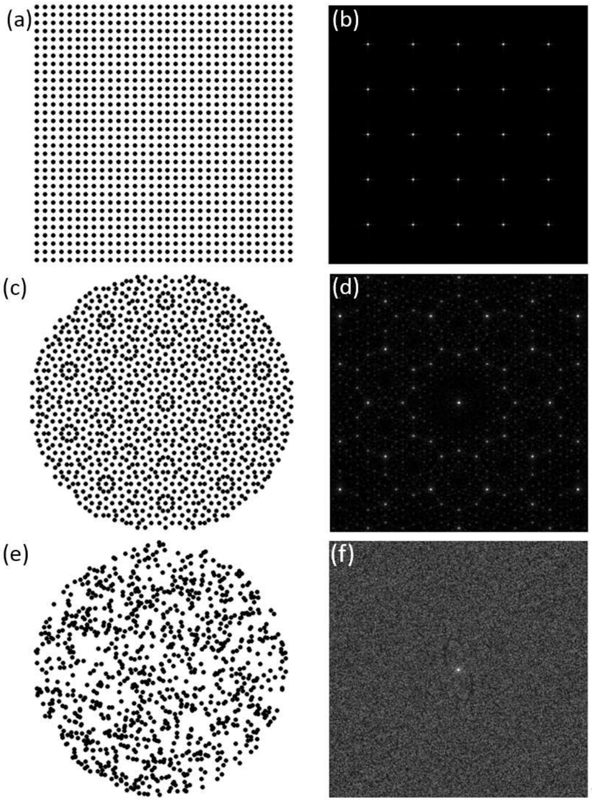

Figure 4·1: (a) $N = 1024$ square array, and its diffraction pattern in (b). (c) $N = 1108$ Penrose array, and its structure factor in (d). (e) $N = 1000$ pseudo-random 2D array, and its structure factor in (f). The third root of the structure factor is plotted for better visualization.(Dal Negro et al., 2016)

Therefore, I show additionally the structural and spectral properties of aperiodic spiral arrays.

Unlike Penrose array that has rotational symmetry but not translational symmetry, spiral point patterns are interesting examples of long-range ordered systems where both translational and orientational symmetries are missing. In particular, we focus on the properties of the so-called Vogel spiral arrays, which have been investigated by mathematicians, botanists, and theoretical biologists in relation to the fascinating geometrical problems of phyllotaxis (Mitchison, 1977; Adam, 2009). Aperiodic Vogel spiral arrays of nanoparticles are rapidly emerging as a powerful nanophotonics platform with distinctive optical properties of interest to a number of engineering applications (Trevino et al., 2012a; Christofi et al., 2016; Pollard and Parker, 2009; **?**; Liew et al., 2011; Dal Negro et al., 2012; Lawrence et al., 2012b; Trevino et al., 2012b; Lawrence et al., 2012a; Capretti et al., 2012). This fascinating class of deterministic aperiodic array pattern can be generated by simple mathematical rules and features circularly symmetric scattering rings in Fourier space with a very rich structural complexity.

In particular, as mentioned in the previous chapter, Vogel spiral point patterns are defined in polar coordinates (r, θ) by the following equations:

$$\rho_n = \sqrt{n} a_{vs}, \tag{4.4}$$

$$\theta_n = n\alpha_{vs}, \tag{4.5}$$

where ρ_n and θ_n denote, respectively, the radial distance and the polar angle of the n-th particle in a Vogel spiral array. a_{vs} is a positive constant called scaling factor, and α_{vs} is typically an irrational number known as the divergence angle (although α_{vs} can be any real number in general). This angle specifies the constant aperture between successive point particles in the array. Since α_{vs} is irrational, Vogel spiral

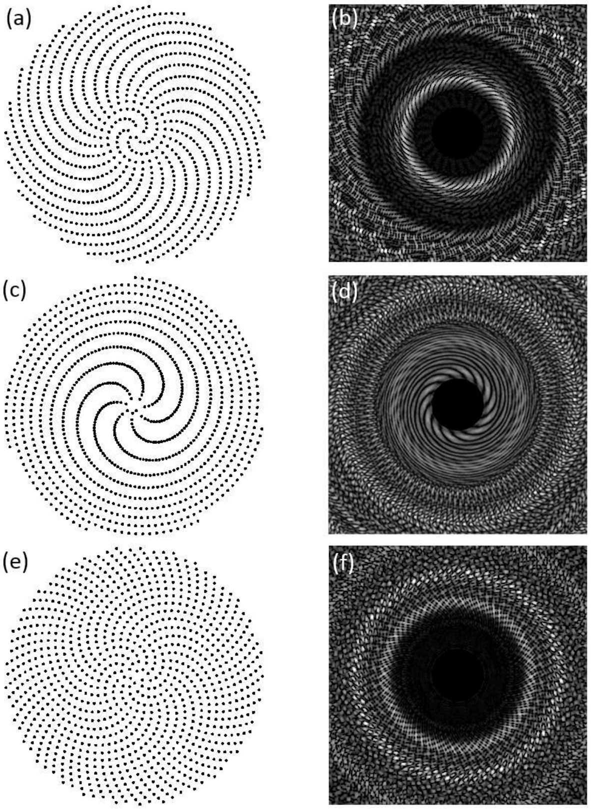

Figure 4·2: $N = 1000$ μ-spiral array in (a), and its structure factor in (b). $N = 1000$ π-spiral array in (c), and its structure factor in (d). $N = 1000$ τ-spiral array (e), and its structure factor in (f). The central maxima for structure factors are excluded to enhance details of higher order diffraction features. (Dal Negro et al., 2016)

point patterns lack both translational and rotational symmetry. Furthermore, for a given irrational number ζ, $\alpha_{vs} = 2\pi(1 - \mathbf{frac}(\zeta))$, where **frac** denotes the fractional part of the irrational number.

In Fig, 4·2, I show three representative $N = 1000$ Vogel spiral point arrays with three different irrational α_{vs}, as well as their corresponding structure factors. In particular, Fig. 4·2(a) is a μ-sprial array with $\zeta = (5 + \sqrt{29})/2$, Fig. 4·2(c) is a π-spiral with $\zeta = \pi$, and Fig. 4·2(e) is a τ-spiral with $\zeta = (2 + \sqrt{8})/2$. From the structure factors (i.e. diffraction patterns) in Figs. 4·2(b), 4·2(d), and 4·2(f), highly rotational symmetric features can be see from the singular continuous spectra. These spectra are neither point-like as in the cases of periodic (Fig. 4·1(b)) and quasiperiodic (Fig. 4·1(d)) arrays, nor absolutely continuous as in the case of the random array (Fig. 4·1(f)). As a result, Vogel spirals are described as deterministic aperiodic.

Calculating the structure factor provides a quick method for understanding the structural symmetries and correlations in the underlying point array, but richer spectral information in connection with electrodynamics needs more rigorous models. As optical media and nanostructures are typically formed by small elements, it is realistic to model point-array elements are interacting electric dipoles coupled through the array geometry. In the next section, I introduce the Green's matrix method, which provides the theoretical ground work for the later chapters.

4.2 The Green's matrix method of coupled electric dipoles

The Green's matrix method is a powerful approach to study wave propagation in random media. The method relies on the analysis of the spectra of the Green's matrix, which belongs to the important class of the so-called Euclidean random matrices that appear in Random Matrix Theory (RMT) (Mehta, 2004; Goetschy and Skipetrov, 2011). The elements of a Euclidean random matrix are determined by a function of the positions of pairs of randomly distributed points in Euclidean space. The interest on non-Hermitian random matrices such as the Green's matrix has significantly increased in recent years due their applications in the theoretical description of open systems.

When applied to random media, the study of the spectra of Green's matrices unveiled important information about scattering resonances (Rusek et al., 2000; Pinheiro et al., 2004; Goetschy and Skipetrov, 2011). Moreover, an analytical theory has also been developed for the eigenvalue density of random Green's matrices, providing fundamental insights into light-matter interactions in disordered media (Goetschy and Skipetrov, 2011). However, the applications of the Green's matrix method has been mostly restricted to random media so far.

The Green's matrix method relies on the analysis of the spectra of the vectorial Green's matrix for three-dimensional vector scattering systems and provides invaluable insights into their general physical properties. In fact, the vectorial Green's matrix also coincides with the kernel of the Foldy-Lax multiple scattering equations used to model arbitrary systems of coupled dipoles (Guerin et al., 2006; Christofi et al., 2016). The method has been extensively used to understand wave transport in multiply scattering open random media (Goetschy and Skipetrov, 2011; Rusek et al., 2000; van Tiggelen et al., 1996; Lagendijk and van Tiggelen, 1996) especially in conjunction with Random Matrix Theory (RMT) (Mehta, 2004). My group has recently applied this approach to understand the scattering properties of periodic, quasiperiodic, and deterministic aperiodic arrays of small nanoparticles (Dal Negro et al., 2016; Christofi et al., 2016). The elements of the $3N \times 3N$ normalized Green's matrix sub-blocks are obtained from the relative positions of N scattering dipoles (Lagendijk and van Tiggelen, 1996):

$$\mathbf{G}_{nm} = (1-\delta_{nm})\frac{1.5e^{ikr_{nm}}}{ikr_{nm}}\{[\mathbf{U} - \widehat{\mathbf{r}}_{nm}\widehat{\mathbf{r}}_{nm}] - (\frac{1}{ikr_{nm}} + \frac{1}{(kr_{nm})^2})[\mathbf{U} - 3\widehat{\mathbf{r}}_{nm}\widehat{\mathbf{r}}_{nm}]\}, \quad (4.6)$$

where $\mathbf{G}_{nm}$ is the 3×3 block element of the vectorial Green's matrix, the integers $n, m \in 1, 2, 3, ..., N$ label particles's positions, k is the optical wavenumber, $\mathbf{U}$ is the 3×3 identity matrix, $\widehat{\mathbf{r}}_{nm}$ is the unit vector position from the n-th to m-th particle, and its magnitude is r. The Green's matrix describes the coupling of each scatterer to all the other scatterers in an arbitrary system through the propagation of electromagnetic vector waves. The vectorial Green's matrix in (4.6) is the sum of three components, each describing electromagnetic interactions proportional to $1/r_{nm}$, $1/r_{nm}^2$, and $1/r_{nm}^3$ corresponding to long-range, intermediate range, and short-range coupling, respectively. Furthermore, it is important to note that the Green's matrix in this form is normalized (i.e. unitless) and bounded by -1 in the real part of the eigenvalues.

Since a Green's matrix is non-Hermitian, its eigenvalues are complex and they entirely characterize the scattering resonances of the system. Specifically, the real and the imaginary parts of the complex eigenvalue Λ_α are related to the relative decay rate $(\Gamma_\alpha - \Gamma_0)/\Gamma_0$ and relative energy position $(\omega_\alpha - \omega_0)/\Gamma_0$ of a scattering resonance, respectively (Rusek et al., 2000; Dal Negro et al., 2016; Christofi et al., 2016) $(\alpha \in 1, 2, 3, ..., 3N)$.

4.3 Spectral Statistics and Scattering Resonances of Complex Primes Arrays

4.3.1 Introduction

In this section, Green's matrix is applied to array structures based on complex-primes, and work is based on the my recently published paper (Wang et al., 2018a). I introduce a new class of highly-diffractive arrays with non-crystallographic rotational symmetries, based on the distinctive aperiodic distribution of prime numbers in complex quadratic fields and quaternion rings, referred to as Complex Primes Arrays (CPAs). In other words, these structures have spatial Fourier spectra that support countably infinite discrete components. These structures also exhibit a rich interplay between structural regularity, both locally and at the long-range level. Being based on prime numbers also results in structural unpredictability due to the distribution of prime numbers that has roots in the most fundamental questions of number theory (Apostol, 1976; Hardy and Wright, 2006). Remarkably, as shown in the next subsection, the structured factor showing the Fourier transform of the structure reveals a noise spectrum with self-similarity described by a power-law scaling (Wolf, 1997). This behavior indicates self-organized critical states of dynamical systems that do not possess any characteristic length scale (Bak et al., 1987).

By applying the Green' s matrix method, I will show a comprehensive investigation of the spectral statistics of scattering resonances in CPAs of electric dipoles, of the Eisenstein, Gaussian, Hurwitz, and Lifschitz prime arrays. Specifically in these structures, results from systematic studies are shown via analyzing the diffraction spectra, the eigenvalue distribution of the Green's matrix, the Density of States, the level spacing distribution, the decay rate statistics, and the spatial extent of the Green's matrix eigenmodes. Several unique spectral properties are demonstrated from these analyses, including the absence of level repulsion in the strongly scattering regime, critical level spacing statistics, and the existence of critical modes (i.e, extended fractal modes with long lifetime). In addition, based on the spectrum of the Green's matrix, one can make predictions about the the existence of spectral gaps in CPAs solely by analyzing the eigenvalue distribution in the complex plane. This introduces novel gapped photonic media with far richer localization and spectral properties compared to usual periodic and random structures.

This section is organized as follows. In the first subsection the structural properties of CPAs are analyzed whereas the spectra of the Green's matrix that describe light propagation in such structures is discussed in the second subsection. Level statistics and the spatial properties of the eigenmodes are treated in third and fourth subsections, respectively. The last subsection provides a summary of results.

4.3.2 The Structure of Complex Primes Arrays

This subsection provides more detailed introduction on the complex primes and prime-based arrays, which are used as examples for applying the Green's matrix method in the following subsections. As will be explained, the number-theoretical characteristics and derived properties make these geometric arrays interesting to study in the optics domain.

The aperiodic CPAs structures considered in this work are constructed based on extensions of the familiar prime number concept from the natural integers to the complex plane, where particles coordinates are made to correspond to the real and imaginary parts of complex primes. Specifically, the focus is on the prime elements of complex quadratic fields such as the Eisenstein and Gaussian integers as well as on the irreducible elements of Hurwitz and Lifschitz quaternions. Eisenstein integers are complex numbers of the form $a + b\omega$, where a and b are natural integers and $\omega = (-1+i\sqrt{3})/2$ is one of the cubic roots of one (i is the imaginary unit). Eisenstein integers are members of the imaginary quadratic field $\mathbb{Q}(\sqrt{-3})$ which is a commutative ring often denoted $\mathbb{Z}[\omega]$. The field of Eisenstein integers has six units, namely ± 1, $\pm\omega$, and $\pm\omega^2$, which when multiplied by prime elements form the so-called prime associates (i.e., equivalent primes). Gaussian integers are complex numbers of the form $a + bi$ where a and b are integers. They are members of the imaginary quadratic field $\mathbb{Q}(\sqrt{-1})$ and form a ring often denoted $\mathbb{Z}[i]$ with units ± 1 and $\pm i$. The Eisenstein integers form a triangular lattice in the complex plane while the Gaussian integers form a square lattice.

Based on algebraic number theory, Eisenstein and Gaussian integers fields are also unique factorization domains in which every non-zero and non-unit element can be written as a product of prime elements (or irreducible elements), uniquely up to rearrangement, complex conjugation and associates (i.e., unit multiples), analogously to the fundamental theorem of arithmetic for the natural integers. As a result, one can find Eisenstein and Gaussian primes and construct arrays by interpreting the real and imaginary parts as two geometric coordinates. In particular, an Eisenstein integer $a + b\omega$ is an Eisenstein prime if and only if either of the following mutually exclusive conditions hold: (i) z is equal to the product of a unit and a natural prime of the form $3n - 1$; (ii) $|z|^2 = a^2 + ab + b^2$ is a natural prime. Similarly, a Gaussian

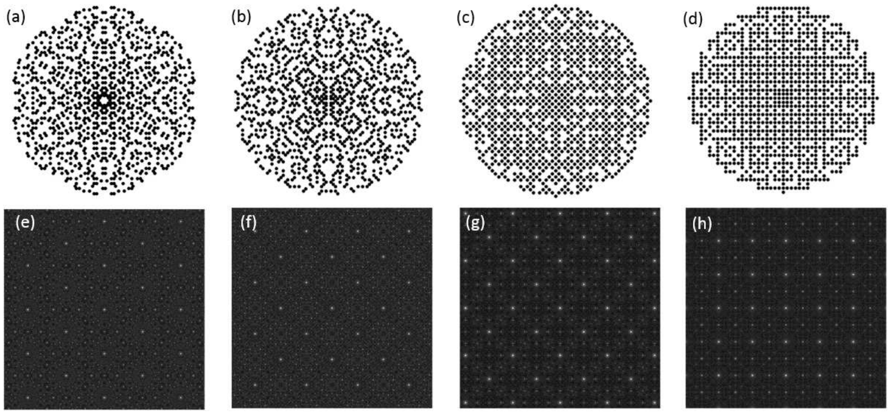

Figure 4·3: (a) N = 1050 Eisenstein prime array, (b) N = 1068 Gaussian prime array, (c) N = 1093 Hurwitz prime array, and (d) N = 1081 Lifschitz prime array. (e) and (h) are the diffraction patterns (5th root taken to enhance contrast) of the corresponding array on top of each panel. (Wang et al., 2018a)

integer $a + bi$ is a Gaussian prime when (i) one of a, b is zero and the absolute value of the other is a prime number of the form $4n + 3$; (ii) both are nonzero and $a^2 + b^2$ is a prime number.

Now, I discuss in more detail the structural properties of the proposed CPAs. Figures 4·3(a) and 4·3(b) show a representative Eisenstein prime array with $N = 1050$ elements and a representative Gaussian prime array with $N = 1068$ elements. Since multiplication by a unit and complex conjugation both preserve primality, the arrays exhibit characteristic $6 \times 2 = 12$ fold rotational symmetry and $2 \times 2 = 8$ fold symmetry, which are incompatible with translational symmetry (i.e., crystallographically forbidden). Moreover, the arrays display a regular structure that nevertheless coexists with their complete lack of periodicity. The unique interplay between symmetry and aperiodicity in these systems is captured by a rigorous result recently established by Tao (Tao, 2006). A second class of CPAs can be constructed based on two-dimensional cross-sections of the irreducible elements of quaternions. Quaternions are numbers of the form $z = a + bi + cj + dk = (a, b, c, d)$ where j, j, k are symbols satisfying

$i^2 = j^2 = k^2 = ijk = -1$. Integer quaternions form a noncommutative ring that unfortunately fails to be a unique factorization domain. However, Hurwitz (Hurwitz, 1919) realized that one can obtain a Euclidean domain when including half units, and defined the Hurwitz integers as quaternions of the form $(a, b, c, d) \in \mathbb{Z}^4 + 1/2(1, 1, 1, 1)$ with integer Euclidean norm $N(z)$. Therefore, Hurwitz quaternions (or Hurwitz integers) are quaternions whose components are either all integers or all half-integers. Moreover, Hurwitz primes are a subset of Hurwitz quaternions with an Euclidean norm ($N(z) = a^2 + b^2 + c^2 + d^2$) that is equal to an integer prime number. Furthermore, the prime elements of the half-integers Hurwitz quaternions are referred to as Lipschitz primes. Geometrically, Hurwitz and Lipschitz integers can be viewed as the integer and the half-integer lattice points on a sphere of radius $\sqrt{N(z)}$ in $\mathbb{R}^4$. A two-dimensional section of the Hurwitz primes is shown in Fig. 4·3(c), consisting of the 1093-element array obtained by projecting Hurwitz primes into the complex plane (considering only the coordinates a and b of each Hurwitz primes and associating the real and imaginary components with the Cartesian coordinates of the scattering dipoles). Similarly, a Lifschitz prime array is shown in Fig. 4·3(d) where only the subset of Hurwitz primes with integer coordinates have been considered (Conway and Smith,).

In order to more rigorously characterize the diffraction properties of the CPAs their spatial Fourier spectra are studied, which are obtained by computing the structure factor, shown in Figs. 4·3(e-h), computed as (Dal Negro et al., 2016):

$$S_N(\mathbf{k}) = \frac{1}{N} \sum_{n=1}^{N} \sum_{m=1}^{N} e^{-j\mathbf{k}\cdot(\mathbf{r}_n - \mathbf{r}_m)} \tag{4.7}$$

where N is the total number of particles in the array. The high degree of structural regularity of the CPAs is manifested in the rotational symmetry of the spectra in Figs. 4·3(e-h), which is a consequence of the corresponding number of associates, as well as in the presence of sharp diffraction peaks. At a closer inspection, these diffraction patterns reveal a hierarchical structure that encodes spatial correlations at multiple length scales. A similar behavior occurs in traditional quasicrystals, e.g. the Penrose lattice, where highly diffractive Bragg peaks densely fill the reciprocal space in a non-periodic and self-similar fashion.

However, in addition to singular components, which are sharp diffraction peaks in the diffraction spectra, Figs. 4·3(e-h) show the presence of a weaker continuous component, or a diffuse background that is typically associated to structural disorder in complex media. This is particularly evident for the Eisenstein prime array in Fig. 4·3(e) and for the Gaussian prime array in Fig. 4·3(f), whose structures are more complex than the ones of Hurwitz and Lifschitz prime arrays shown in Figs. 4·3(g) and 4·3(h), respectively. Aperiodic structures whose diffraction spectra display a coexistence of singular and continuous spectral components are referred to as singular-continuous, and the numerical results provide evidence that the proposed CPAs belong to this category. Singular-continuous spectra are often discovered in complex systems with chaotic dynamics, fractal structures, and are commonly observed in traditional quasicrystals (Senechal, 1995).

The nature of the Fourier spectra of CPAs can be more accurately understood by studying the behavior of the Integrated Intensity Function (IIF) (Maciá, 2009):

$$H_N(k) = \int_0^k \int_0^k |S_N(k'_x, k'_y)| dk'_x dk'_y \tag{4.8}$$

For two-dimensional arrays this function characterizes the distribution of the diffracted intensity peaks contained within a 2D square region, centered at the origin, with maximum size $2k \times 2k$ in the reciprocal space. It should be realized that the exact nature of the diffraction spectrum is only determined by the asymptotic limit of equation (4.8) for a system of infinite size ($N \to \infty$) and only heuristic information can be ex-

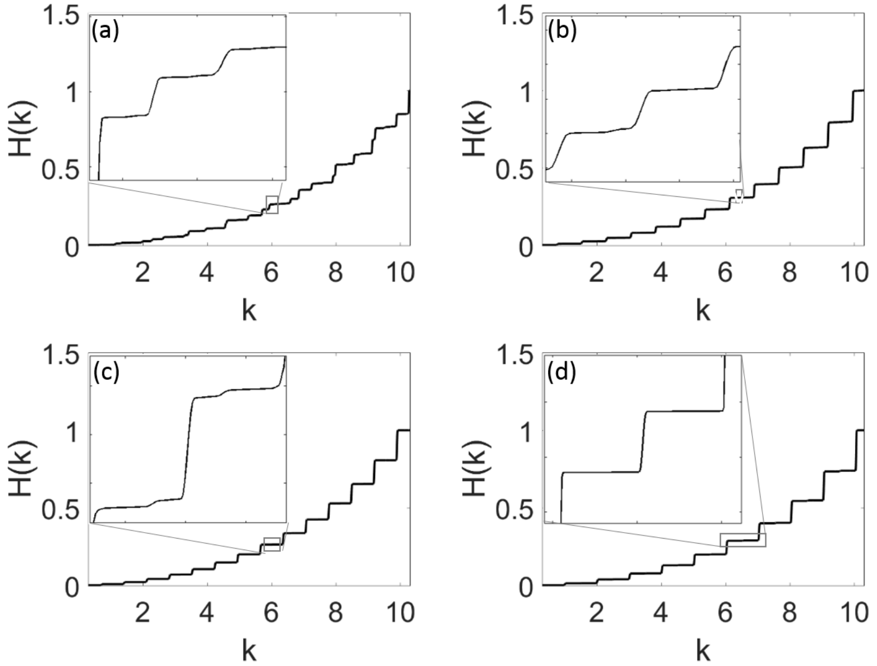

Figure 4·4: The H(k) of (a) Eisenstein prime, (b) Gaussian prime, (c) Hurwitz prime, (d) Lifschitz prime.(Wang et al., 2018a)

tracted for finite-size structures. The behavior of the IIF can be understood as follows. In both periodic and quasiperiodic structures there are regions where $H(k)$ vanishes due to the discrete nature of their spectra. Therefore, over those regions $H(k)$ must remain constant and it will present jump discontinuities every time an isolated Bragg peak is integrated. On the other hand, for structures with continuous Fourier spectra the function $H(k)$ is smooth (i.e. continuous and differentiable). In the case of structures with singular-continuous spectra the Bragg peaks are no longer well-separated but cluster into a hierarchy of self-similar contributions giving rise to a continuous component in the spectrum that smoothly increases the value of $H(k)$ in between the plateaus. Fig. 4·4 show the calculated $H(k)$ for each of the CPAs. The results demonstrate a characteristic aperiodic staircase with a fractal behavior highlighted by computing $H(k)$ over a much smaller scale, as shown in the insets of Fig. 4·4. Fig. 4·4(a) show the $H(k)$ of the Eisenstein prime array, which demonstrates clear jump discontinuities in correspondence of the bright diffraction peaks shown in Fig. 4·3(e). Moreover, the presence of the continuous components is manifested by the varying slopes that smoothly connect each plateau of $H(k)$, unveiling the singular-continuous nature of the spectra. Qualitatively similar features are also observed for all the other CPAs. However, the respective contribution of the continuous components weaken progressively from Eisenstein and Gaussian primes, shown in Figs. 4·3(a) and 4·3(b), to Hurwitz and Lifschitz structures shown in Figs. 4·3(c) and 4·3(d). This behavior is consistent with the much more regular structure displayed in real space by the Hurwitz and Lifschitz arrays. This heuristic analysis leads to conjecture a surprising connection between the distribution of primes in complex quadratic fields and the singular-continuous spectra of two-dimensional quasicrystals. This scenario can be regarded as a two-dimensional generalization of Freeman Dyson's conjecture on the quasi-crystalline nature of the the Fourier spectrum of the zeta-function zeros on the critical line, which encode information on the distribution of the natural prime numbers (Dyson, 2009).

4.3.3 Green's matrix spectral properties

By using the Green's matrix method, spectral information of the complex-prime based arrays can be analyzed. Figs. 3 and 4 show the eigenvalue distributions for different values of the optical density $\rho\lambda^2$ (with ρ the number of particles per unit area and λ the optical wavelength) for Eisenstein prime and Hurwitz prime arrays, respectively. Qualitatively similar results are also obtained for Gaussian primes and Lifschitz structures.

All the complex eigenvalues shown in Figs. 4·4 and 4·6 are color-coded based on the log_{10} value of Inverse Participation Ratio (IPR) of the corresponding eigenvectors,

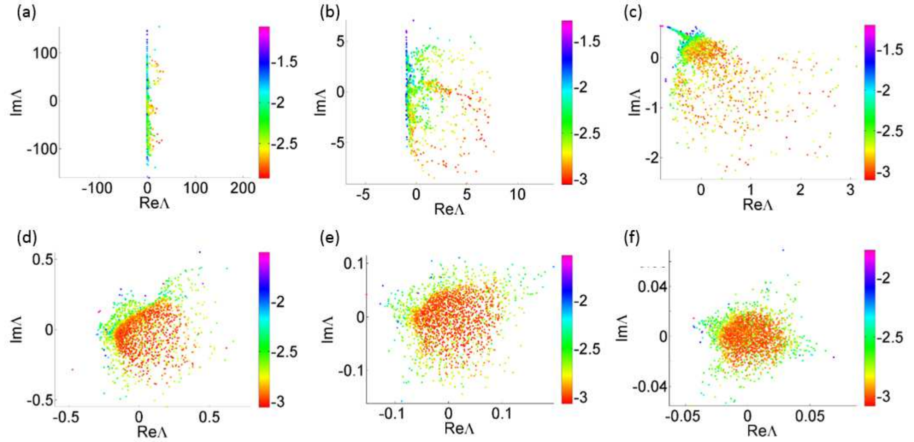

Figure 4·5: Eigenvalue distributions of Eisenstein prime arrays with $\rho\lambda^2$ = (a) 100, (b) 10, (c) 1, (d) 0.1, (e) 0.01, (f) 0.001. The color-coding shows the log10 values of IPR for the eigenmode corresponding to each eigenvalue.(Wang et al., 2018a)

defined as (Goetschy and Skipetrov, 2011):

$$IPR_p = \frac{\sum_{i=1}^{N} |\mathbf{R}_p(\mathbf{r}_i)|^4}{[\sum_{i=1}^{N} |\mathbf{R}_p(\mathbf{r}_i)|^2]^2} \ , \tag{4.9}$$

where $\mathbf{R}_p(\mathbf{r}_i)$ is the p-th normalized eigenmode of the Green's matrix, and $(\mathbf{r}_i)$ are positions of scatterers. The IPR measures the degree of spatial localization of the eigenvectors. An eigenvector that extends over all the N scatterers is characterized by a low value of $IPR \simeq 1/N$, while an eigenvector localized at a single point has $IPR = 1$.

We notice in Fig. 4·5(a) that when the optical density is the largest (i.e. $\rho\lambda^2 = 100$), the spectrum collapses around the region $Re\Lambda = -1$ which correspond to long-lived modes (i. e., the decay rate $\Gamma \approx 0$). Furthermore, we observe that the corresponding eigenstates display larger IPR values, $i.e.$ more spatial localization, towards larger values of $|Im\Lambda|$. Among the eigenvalues with $Re\Lambda \simeq -1$, those with larger absolute values in the imaginary part have increasingly higher IPR values. In random systems proximity resonances ($Re\Lambda \approx -1$, $Im\Lambda \gg 1$, and $IPR = 0.5$) spatially localized over pairs of particles very close together, may exist even for weakly scattering systems, far from the regime of Anderson localization (Rusek et al., 2000). In contrast, two-particle proximity resonances are generally absent in the investigated aperiodic systems, where eigenstates localized over small clusters of particles, similar to Efimov-type of resonances, occur more frequently due to locally symmetric particle clusters distributed across these structures. It is also interesting to notice in Fig. 4·5(a) that a spectral gap opens in the complex plane between $Im\Lambda = 0$ and 100. This feature, which does not occur in random arrays, reflects the role of spatial correlations in the Eisenstein prime array, and can also be observed in all the other aperiodic arrays at large enough density.

On the other hand, when the optical density decreases the sub-radiant eigenmodes at $Re\Lambda \approx -1$ gradually disappear from the spectra as shown in Figs. 4·5(b) to 4·5(f) and the complex eigenvalue distributions eventually evolve into a more homogeneous domain in the complex plane centered near $\Lambda = 0$ (Fig. 4·5(d) to 4·5(f)). This spectral evolution reflects the occurrence of an increasing proportion of short-lived eigenstates with low IPR extending over a larger number of particles and characterized by a larger decay rate. Besides, the IPR values are more uniformly distributed across the different eigenvalues at low optical densities showing that these states are very similar in both energy and decay characteristics.

Importantly, the low-density distribution of eigenvalues for all the investigated CPAs does not approach a circular distribution in the complex plane, as it would be the case for a uniform random medium (Rusek et al., 2000; Dal Negro et al., 2016; Goetschy and Skipetrov, 2011; Skipetrov and Goetschy, 2011), even at very low optical density of 0.001 particle per λ^2. This indicates a persistent correlation effect, which is present even at very small optical densities, where the average interparticle separation is more than one order of magnitude larger compared than the wavelength.

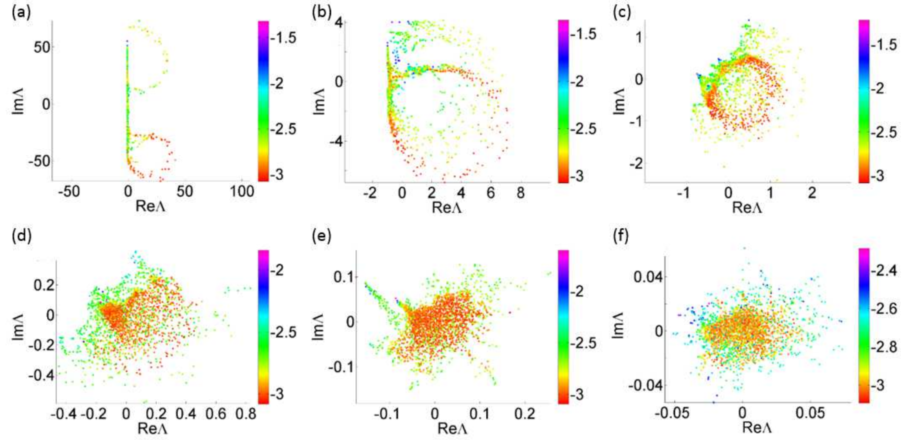

Figure 4·6: Eigenvalue distributions of Hurwitz prime arrays with $\rho\lambda^2$ = (a) 100, (b) 10, (c) 1, (d) 0.1, (e) 0.01, (f) 0.001. The color-coding shows the log10 values of IPR for the eigenmode corresponding to each eigenvalue.(Wang et al., 2018a)

In Figs. 4·6(a) to 4·6(f), we summarize the evolution of eigenvalue distributions at the six representative optical densities for a N = 1093 Hurwitz prime array. Unlike in the case of Eisenstein prime array, the distribution of eigenvalues for the Hurwitz prime array at $\rho\lambda^2 = 100$ does not feature large sub-radiant components, and it exhibits two large circular gap regions in the high-density spectrum that originates from its more significant structural regularity. This behavior is very similar to the eigenvalue distribution of a periodic square array at such large optical density. As the optical density decreases from Figs. 4·6(b) to 4·6(f), the eigenvalues eventually cluster into a smaller region of the complex plane around $\Lambda = 0$. Similar to the case of the Eisenstein prime array, the presence of correlation effects prevent the eigenvalue distribution to approach, even at the smallest density values, the circular disk distribution expected for uniform random systems.

We notice that in all the investigated CPAs the value $\rho\lambda^2 \approx 1$ appears to separate a highly structured eigenvalue distribution, where spatial correlations plays a dominant role, from a diffuse eigenvalue distribution with weaker correlations at low density.

The formation of spectral gaps in CPAs when increasing the optical density is best demonstrated in Fig. 4·7 by the density of states (DOS) computed for all the investigated structures based on the imaginary part of the Green's matrix eigenvalues. In Fig. 4·7, we plot the DOS for all the structures at three representative optical densities, $\rho\lambda^2 = 100$, 10, and 0.001, and plot them versus the normalized energy. The numerical study indicates opening of gaps at values of the optical density $\rho\lambda^2 \gtrsim 10$. This density regime corresponds to a linear particle separation approximately equal to the wavelength, resulting in a strong diffractive response of the CPA structures. In particular, in Fig. 4·7(e), Eisenstein prime array has a gap near $(E - E_0)/\Gamma_0 = 1$, whereas in Fig. 4·7(h), Hurwitz prime array has multiple gaps near $(E - E_0)/\Gamma_0 = 0$, 1, and 2. On the other hand, at the lowest optical density $\rho\lambda^2 = 0.001$ the scattering strength is too weak to open optical gaps in all the investigated structures, as demonstrated in Figs. 4·7(i) to 4·7(l).

4.3.4 Spectral Statistics of Complex Primes

Level statistics provides important information about electromagnetic propagation in both closed and open systems, and from RMT one can to identify the wave transport regime (extended or localized) in closed systems. For open systems that are not random, level statistics remains not very well understood especially at low optical densities. In my previous work, the Green's matrix method has been applied to study open systems that are either random, or aperiodic, and have shown the transition from the absence to the presence of level repulsion as the optical density decreases (Dal Negro et al., 2016). In open systems the Green's matrix is non-Hermitian, so that for each Λ_i the nearest eigenvalue Λ_j is identified as the eigenvalue that minimizes the distance between the two eigenvalues in the complex plane $|\Delta\Lambda| = |\Lambda_i - \Lambda_j|$

In closed random systems, an established result from RMT predicts the suppression of level repulsion in the presence of localizes states (Mehta, 2004; Haake, 2010).

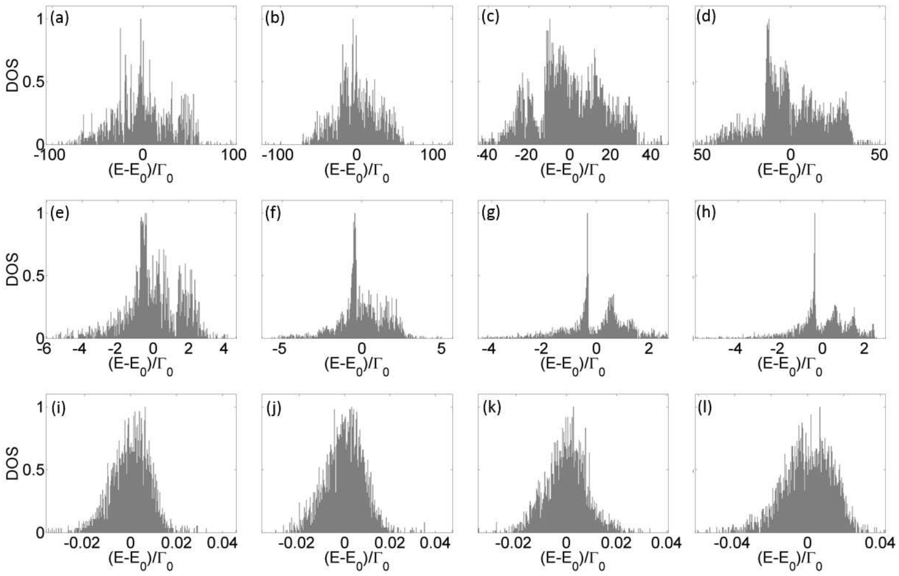

Figure 4·7: The DOS for (a) Eisenstein prime, (b) Gaussian prime, (c) Hurwitz prime, (d) Lifschitz prime, at $\rho\lambda^2$=100; (e) Eisenstein prime, (f) Gaussian prime, (g) Hurwitz prime, (h) Lifschitz prime, at $\rho\lambda^2$=10.(i) Eisenstein prime, (j) Gaussian prime, (k) Hurwitz prime, (l) Lifschitz prime, at $\rho\lambda^2$=0.001.(Wang et al., 2018a)

In this case two spatially separated, exponentially localized states hardly influence each other, so that distinct modes with infinitely close energies are possible. In the strong localization regime the distribution of level spacings is described by the Poisson distribution (Haake, 2010):

$$p(s) \propto \exp\left(-s\right), \tag{4.10}$$

where we consider the nearest-neighbor level spacing normalized to the average spacing as $s = |\Delta\Lambda|/\langle|\Delta\Lambda|\rangle$. For inhomogeneous systems, as it is the case of CPAs, special care needs to be exercised in order to eliminate degenerate energy states caused by the geometrical symmetries inherent to the structure of the arrays.

In Fig. 4·8, we show the two most extreme cases (highest and lowest optical densities) of level spacing statistics for each of the four CPA structures. In particular, Figs. 4·8(a) to 4·8(d) show the first-neighbor level statistics of the Eisenstein prime,

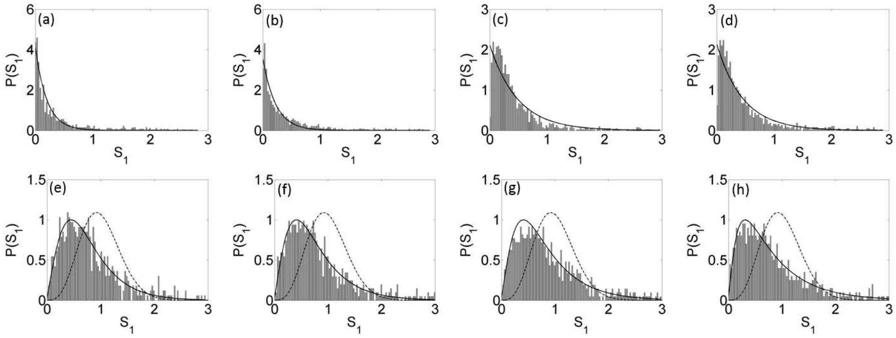

Figure 4·8: The 1st-neighbor level statistics of complex eigenvalues for (a) Eisenstein prime, (b) Gaussian prime, (c) Hurwitz prime, (d) Lifschitz prime, at $\rho\lambda^2$=100; (e) Eisenstein prime, (f) Gaussian prime, (g) Hurwitz prime, (h) Lifschitz prime, at $\rho\lambda^2$=0.001.(Wang et al., 2018a)

Gaussian prime, Lifschitz prime, and Hurwitz prime arrays, respectively, at $\rho\lambda^2 = 100$. The black lines in Figs. 4·8(a) to 4·8(d) are best fitting curves using a Poisson distribution model. The results demonstrate that level spacing with Poisson statistics has been achieved in the proposed CPAs for high optical densities, in complete analogy with the localization regime observed in uniform random media.

In contrast, a well-known result of RMT is the phenomenon of level repulsion in the extended regime of wave transport in closed systems (Mehta, 2004; Haake, 2010). In open systems, the concept of eigenvalue repulsion can be generalized to non-Hermitian matrices. Indeed, for the Ginibre's ensemble of random matrices, the probability density function of normalized eigenvalue spacing is (Haake, 2010)

$$p(s) = \frac{3^4\pi^2}{2^7} s^3 \exp(-\frac{3^2\pi}{2^4} s^2), \tag{4.11}$$

which has been successfully applied to describe the statistical properties of eigenmodes in random optical media (Skipetrov and Sokolov, 2015). For all aperiodic media considered, we demonstrate the emergence of level repulsion, $i.e. P(0) = 0$, at low optical densities of $\rho\lambda^2 = 0.001$, as shown in In Figs. 4·8(e) to 4·8(h). However, in contrast to random media, the distribution of level spacing predicted by the Ginibre's ensemble in equation (4.11) (represented by dashed lines in Fig. 4·8) does not accurately describe the spectral statistics of CPAs. Instead, a good fit to the level statistics can be obtained only using the derivative of interpolation function, called critical cumulative probability, proposed in (Zharekeshev and Kramer, 1997):

$$I(s) = \exp[\mu - \sqrt{\mu^2 + (A_c s)^2}], \tag{4.12}$$

where $I(s)$ is the cumulative level spacing distribution function, μ and A_c are fitting parameters. The fit of the data using this model is shown by the black lines in Figs. 4·8(e) to 4·8(h). The critical statistics model has been introduced to account for the level spacing at the Anderson transition in random media (Zharekeshev and Kramer, 1997), where the wavefunctions feature multifractal scaling, and it has been proposed as a third universal level statistics valid at the Metal Insulator Transition (MIT) of aperiodic media. The findings demonstrate the applicability of critical statistics to the weakly scattering regime of CPAs. Indeed, the critical nature of the CPAs level spacing statistics can be traced back to their singular-continuous spectra that support critically localized eigenmodes with self-similar scaling at all optical densities. Differently from random media, where criticality is only achieved at the localization threshold, which occurs for a specific optical density in 3D, the critical behavior of CPAs occurs for a broader range of optical densities for planar, weakly scattering systems, and it is inherent to the fractal nature of their geometries and critical eigenmodes.

In Fig. 4·9 we show the decay rate statistics $P(\Gamma)$ for different CPAs and for for three distinct values of the optical density, where decay rates were obtained form the Green's matrix eigenvalues, $\Gamma/\Gamma_0 \approx Re\Lambda + 1$. (Rusek et al., 2000) In particular, in Figs. 4·9(a-d) we plot the statistics of the normalized decay rates in a double-logarithmic scale, for the four prime-based aperiodic arrays at the highest optical density $\rho\lambda^2 = 100$. In this regime, we have conclusively found that the data follow a linear decay, which unveils an algebraic power law scaling $P(\Gamma) \simeq 1/\Gamma$. This power law behavior of the decay rate statistics, which has been reported in disordered systems (Pinheiro et al., 2004; Goetschy and Skipetrov, 2011), is a result of multiple scattering (Goetschy and Skipetrov, 2011). Figures 4·9(a-d) indicate that the power law of $P(\Gamma) \sim \Gamma^{-1}$ also occurs for more general open aperiodic systems such as the CPAs for high optical densities ($\rho\lambda^2 = 100$). As it occurs in random systems (Pinheiro et al., 2004), the range of this algebraic decay increases for increasing optical densities for which multiple scattering effects are stronger, as it can be seen by comparing Figs 4·9(a-d) with Figs 4·9(e-h), for which the optical density is lower, ($\rho\lambda^2 = 10$).

Finally we note that, differently from uniformly random systems, the tails with very large decay rate in the statistics of CPAs shown in Figs. 4·9(a) to 4·9(d) do not feature any prominent peak due to Dicke superradiant modes, which would manifest as a peak at $P(\Gamma)$ at $\Gamma = 2\Gamma_0$) with IPR=0.5 (Akkermans et al., 2008; Dicke, 1954). This result, together with the absence of proximity resonances with small decay rates unveiled in Fig. 4·5, show that collective effects involving pair of scatterers (subrandiance and superradiance), do not occur in the investigated CPAs. We believe that this behavior can be attributed to the highly correlated nature of CPAs, which prevents the formation of such modes.

4.3.5 Spatial distribution of eigenstates

In order to further understand the spatial distribution of eigenmodes in aperiodically ordered structures, in Fig. 4·10 we show the maximum IPR value among all CPA eigenstates for different values of the optical density. For comparison, we also show the results obtained for a uniform random array of dipoles as well as for periodic square and triangular arrays. We have found that among all the investigated geometries the uniformly random array support eigenstates with the largest IPR values for all

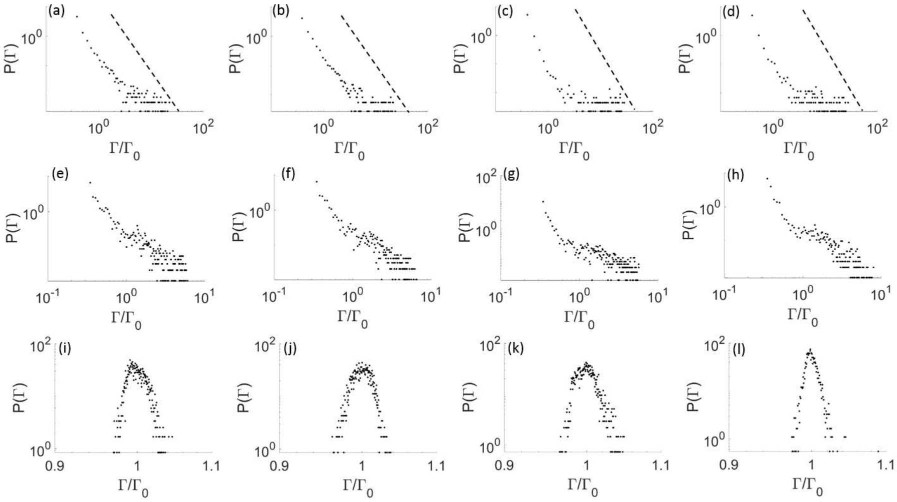

Figure 4·9: The decay rate statistics for ((a) Eisenstein prime, (b) Gaussian prime, (c) Hurwitz prime, (d) Lifschitz prime, at $\rho\lambda^2$=100; (e) Eisenstein prime, (f) Gaussian prime, (g) Hurwitz prime, (h) Lifschitz prime, at $\rho\lambda^2$=10.(i) Eisenstein prime, (j) Gaussian prime, (k) Hurwitz prime, (l) Lifschitz prime, at $\rho\lambda^2$=0.001.(Wang et al., 2018a)

optical densities considered, as shown in Fig. 4·10. Indeed, these modes with largest $IPR = 0.5$ correspond to proximity resonances that involve only two neighboring particles and, as Fig. 4·10 reveals, can occur even for weakly scattering systems (low optical densities) (Rusek et al., 2000). Figure 4·10 demonstrates that these proximity resonances cannot be supported by CPAs under the conditions investigated. Besides, the largest values of IPR for CPAs are significantly larger than the corresponding ones of periodic arrays of dipoles. Based on the value of maximum IPR, we can estimate the number of particles over which the most spatially localized states are distributed. In particular, at high optical densities, Efimov resonances (Efimov, 1970), typically distributed over few dipoles, are more likely to occur in structures such as Eisenstein prime and Gaussian prime arrays.

In Figs. 4·11(a) to 4·11(d) the statistical distributions of IPRs are shown for CPAs in the strongly scattering regime, achieved at the largest optical density considered, $\rho\lambda^2 = 100$. It can be seen that the IPR distributions for Eisenstein prime and

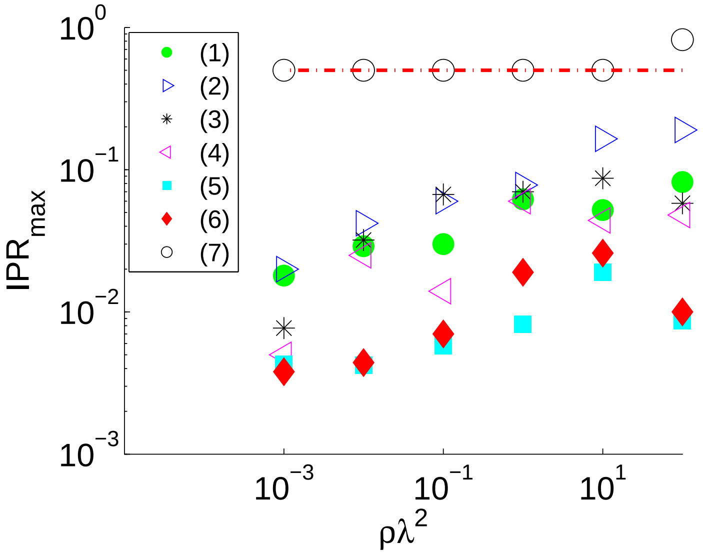

Figure 4·10: A comparison of maximum IPR values among (1) Eisenstein prime, (2) Gaussian prime, (3) Lifschitz prime, and (4) Hurwitz prime arrays, at each representative optical density. (5) square, (6) triangular and (7) uniform random arrays are included for references. The red dashed line indicate the proximity resonance of two particles with IPR = 0.5.(Wang et al., 2018a)

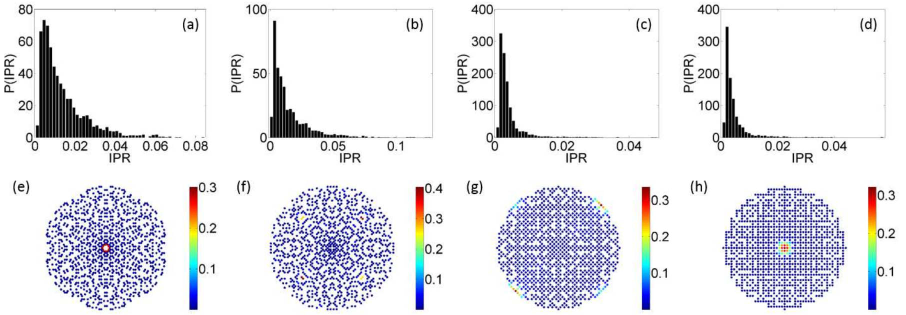

Figure 4·11: The IPR statistics for (a) Eisenstein prime, (b) Gaussian prime, (c) Hurwitz prime, (d) Lifschitz prime, at $\rho\lambda^2 = 100$; The mode with the highest IPR values are for each of the structures at this density are shown respectively from (e) to (h).(Wang et al., 2018a)

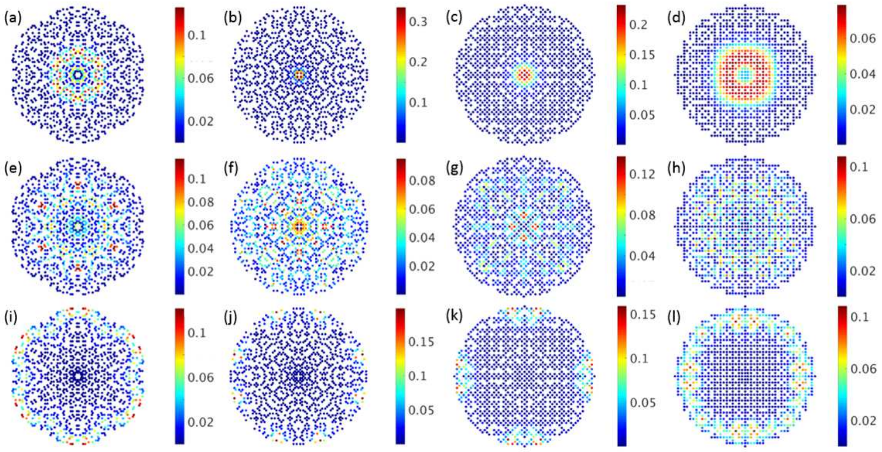

Figure 4·12: At $\rho\lambda^2 = 10$, (a) to (d) are the most localized (highest associated IPR value) eigenmode for Eisenstein prime, Gaussian prime, Hurwitz prime and Lifschitz prime arrays, respectively. (e) to (h) are corresponding structure's critical mode, which has the lowest IPR and small ReΛ (low decay rate). (i) to (l) are spectral-gap edge-modes of each corresponding structure.(Wang et al., 2018a)

Gaussian prime arrays are considerably broader than the ones of the corresponding Hurwitz and Lifschitz primes structures. This result reflects the fact Hurwitz and Lifschitz prime arrays are much more regularly distributed in real space than the Eisenstein and Gaussian prime arrays, consistent with the results for the Integrated Intensity Function shown in Fig. 4·4. Figures 4·11(a) to 4·11(d) also confirm that the probability of finding Efimov resonances, spatially localized over a small number M of scattering particles (with corresponding larger IPRs $\simeq 1/M$), is smaller for more regular CPAs, such as the Hurwitz and Lifschitz primes arrays. In Figs. 4·11(e-h) we show the intensities of the eigenvectors with largest IPR at the positions' of the scattering particles at optical density $\rho\lambda^2 = 100$ for different CPAs. The spatial distribution of the mode with largest IPR strongly depends on the particular spatial structure of the CPA in the real space. For instance, in the Eisenstein and Lifschitz prime arrays the mode with largest IPR is highly localized over a small cluster of dipoles in the center of structure, as Fig. 9(e) and (h) reveal. On the other hand,

Fig. 4·11(g) demonstrates that for the Hurwitz prime array the highest-IPR eigenstate is symmetrically localized at the edge of the structure over T-shaped particle clusters.

In Fig. 4·12 we provide a more complete survey of the spatial extent of distinctive eigenstates that can be supported by different CPAs, namely the one with highest-IPR (Figs. 4·12(a) to 4·12(d)), the critical modes (Figs. 4·12(e) to 4·12(h)), and the ones localized at the edge of the structures (panels (i) to (l)) at $\rho\lambda^2 = 10$. Again, the spatial distribution of intensities of the highest-IPR mode crucially depends on the particular structure of the CPA in the real space. Indeed, Figs. 4·12(a) to 4·12(d) demonstrate that, for a given optical density, the highest-IPR mode may be either extremely localized at the center of the array, as it is the case of Gaussian prime array, or more radially spread around the center of the structure, as in the Lifschitz prime array. The critical modes, which have been recently identified as the ones with long-lived resonances (small decay rates) with low IPR values (Dal Negro et al., 2016), are depicted in Figs. 4·12(e-f). These modes, which are spatially extended over the whole array, are unique to deterministic aperiodic systems and cannot be supported by either random or periodic systems. Figs. 4·12(e-h) unveil the very rich spatial distribution and distinctive critical nature of eigenmodes for all CPAs considered. Finally, we also discovered in the CPAs mode spectrum long-lived modes that are spatially localized close to the edge of the structures, as shown in Figs. 4·12(i-l). Such surface-localized modes appear to be analogous to the recently discovered topological edge-states in quasiperiodic systems (Bandres et al.,). However, further studies beyond the scope of this work are needed to established the exact physical nature of edge-states in the investigated CPAs.

4.3.6 Section summary

In conclusion, this section investigates the structural, spectral and localization properties of aperiodic arrays generated from the distribution of prime numbers in complex quadratic fields (Eisenstein, Gaussian) and quaternion rings (Hurwitz, and Lifschitz primes arrays) and studied their distinctive scattering resonances using the vector Green's matrix method. We systematically study the Fourier spectra, the eigenvalue distribution of the Green's matrix, the Density of States, level spacing distribution, the decay rate statistics, and the spatial extent of eigenmodes in all these structures. The findings demonstrate several unique spectral properties, such as the absence of level repulsion for strongly scattering systems, critical level statistics, and the existence of critical modes, extended fractal modes with long lifetime that cannot be supported by either random and periodic systems. From the distribution of eigenvalues of Green's matrix in the complex plane, the existence spectral gaps can be predicted. The results unveil the importance of aperiodic correlations for the engineering of novel gapped photonic structures that support far richer spectral properties compared to traditional periodic and random media.

4.4 Edge Modes of Scattering Chains with Aperiodic Order

In the previous section, I have shown the use of Green's matrix method in understanding complex prime-based arrays which can be useful to engineer novel metamaterials and metasurfaces. In the current section, I present work on applying Green's matrix method to aperiodic chains. This section, adopted and modified based on my work in review (Wang et al., 2018b), hints the potential of using Green's matrix as a tool to engineer topological metamaterial characterized by coupled radiating dipoles with full electromagnetic scattering of vector waves.

4.4.1 Introduction

Analogues of topological insulating phases have been discovered in periodic photonic structures and quasiperiodic systems with modulated short-range coupling (Rechtsman et al., 2013; Noh et al., 2017; Levy and Akkermans, 2017; Verbin et al., 2015;

Bandres et al., ; Xiao and Fan, 2017) in close correspondence with the transport of quantum waves in electronic materials. However, topological effects in dissipative (non-Hermitian) electromagnetic scattering systems that support long-range collective resonances have not been investigated.

In this section, by systematically studying the spectral properties of the vectorial Green's matrix for linear chains of point dipoles with aperiodic order, we discover and characterize topological band structures and edge-localized resonances in open scattering systems. In particular, our work shows that edge modes with topological dispersion appear in the complex spectrum of the scattering resonances as described by the vectorial Green's matrix, beyond the tight-binding approximation. Remarkably, we found that distinctive topological structures also appear in more complex deterministic aperiodic systems with Thue-Morse modulated coupling. We focus specifically on the optical analogues of the Su-Schrieffer-Heeger (SSH) and the Harper models, and extend our analysis to Fibonacci and Thue-Morse chains, which are primary examples of periodic, quasiperiodic, and deterministic aperiodic systems, respectively. Our results extend the concept of topological states to open scattering systems and provide an efficient tool for the predictive design of novel topological effects in aperiodic photonic structures.

In the following sections, we will focus on the distribution of energy states of the resonances of chains of dipole scatterers with different positional order, and retrieve topological information directly from the eigenvalues of the Green's matrix. Although we present results on chains with optical density $\rho = 10$ (10 dipoles per wavelength), our main conclusions remain valid even in lower density chains down to approximately $\rho = 1$.

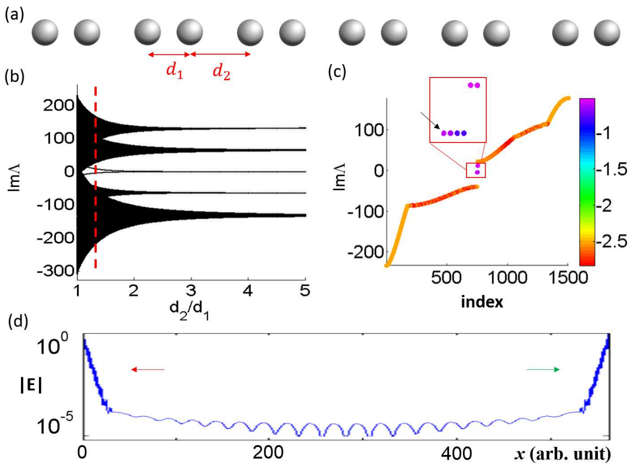

Figure 4·13: (a) Dimer chain of identical dipole scatterers with alternating distance modulation. (b) Topological band-structure from the vectorial Greens matrix of a 500-dipole chain. (c) Energy spectrum for $d_2/d_1 = 1.25$ (red line in (b)), and the inset shows the 6 edge modes inside the band gap. Color-bar shows $log_{10}(IPR)$. (d) A representative edge mode in the gap. (Wang et al., 2018b)

4.4.2 Topological bandstructure and edge states from the Green's matrix method

First we consider a doubly periodic dimer chain, which is the photonic counterpart of the Su-Schrieffer-Heeger (SSH) model of a topological insulator (Asboth et al., 2016). This model describes spinless fermions hopping on a one-dimensional lattice with staggered hopping amplitudes. In our photonic implementation we identify the SSH hopping amplitudes with two separate values of inter-particle separations, d_1 and d_2, which alternate along the chain as illustrated schematically in Fig. 4·13(a). The periodic variation in the inter-dipole separations results in a modulation of the electromagnetic interaction that gives rise to distinctive gaps and topological effects. However, differently from the standard tight-binding description, in our photonic implementation the vector dipoles interact not only through short-range coupling, but also via the intermediate- and long-range contributions of the Green's matrix. In Fig. 4·13(b), the imaginary part of the eigenvalues, which is proportional to the energy position of the scattering resonances, is plotted for the dimer chain against the ratio of the two inter-particle distances, d_1/d_2, which ranges from 1 to 5. In close analogy with the case of the electronic SSH dimer case (Asboth et al., 2016), this quantity plays the role of an effective topological parameter. As it is varied, there appear in Fig. 4·13(b) energy gaps that are traversed by band-gap states near $Im\Lambda = 0$. We will now show that these band-gap states correspond to edge-localized modes. In particular, we focus for concreteness on the spectrum of the dimer structure with $d_1/d_2 = 1.25$, which is highlighted by the vertical red line in Fig. 4·13(b), and plot in Fig. 4·13(c) the energies of its scattering resonances. We observe one clear band-gap around $Im\Lambda = 0$ containing 6 states. The inset of Fig. 1(c) magnifies the energy region around the band-gap states, which separate into 2 distinct energies. These band-gap states originate from the 3 polarizations of the vectorial Green's matrix and are doubly degenerate. In order to better understand their spatial localization properties, we compute the inverse participation ratio (IPR) for the eigenmodes defined in the last subsection 4.9. The IPR measures the degree of spatial extent of each eigenmode in the system. For example, an eigenmode that extends over all the N scattering centers is characterized by a low value of $IPR \simeq 1/N$, while an eigenmode localized at a single dipole of the chain has a large $IPR = 1$. Fig. 4·13(c) is color-coded to reflect the value of the IPR for each eigenstate in a logarithmic scale, and demonstrates that the modes residing within the gap region display the largest IPR values. We plot in Fig. 4·13(d) the spatial distribution of one representative edge-state in the selected gap region, which displays a large amplitude localized at both edges of the chain. The remaining band-gap states have almost identical edge-localized profiles.

We now apply the same methodology to more complex structures with aperiodic order. Tight-binding models for deterministic aperiodic potentials based on the Harper Hamiltonian or the Fibonacci quasi-periodic potential have attracted a con-

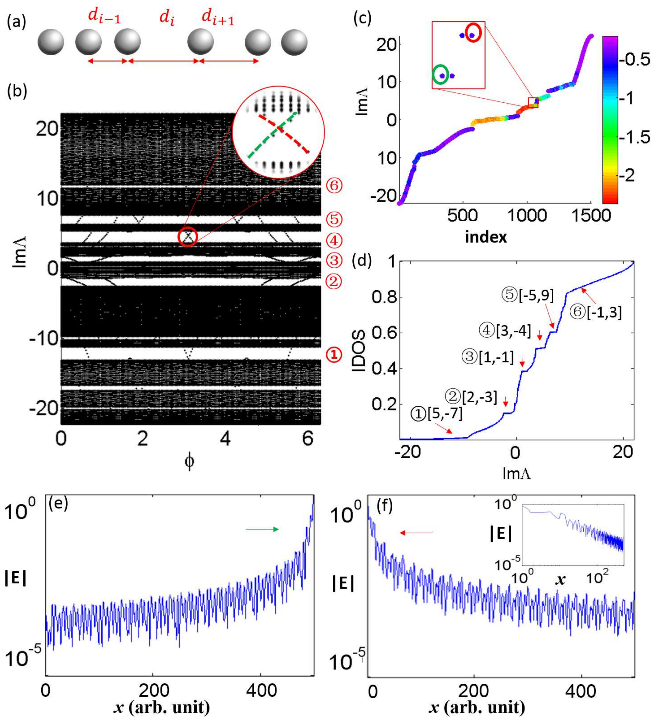

Figure 4·14: (a) Harper chain with distance modulation; (b) Topological band-structure obtained with with the vectorial Green's matrix for the Harper chain with 500 particles. The inset is a zoom-in around the crossing of the edge states. (c) Energy levels for $\phi = 3.05$, and the edge-state in the gap. (d) Corresponding IDOS and labeling of gaps by the two integers [p,q] as in Eq. 4.14. (e) and (f) are two edge modes in the gap. The inset of (f) shows the log-log plot of the field profile.(Wang et al., 2018b)

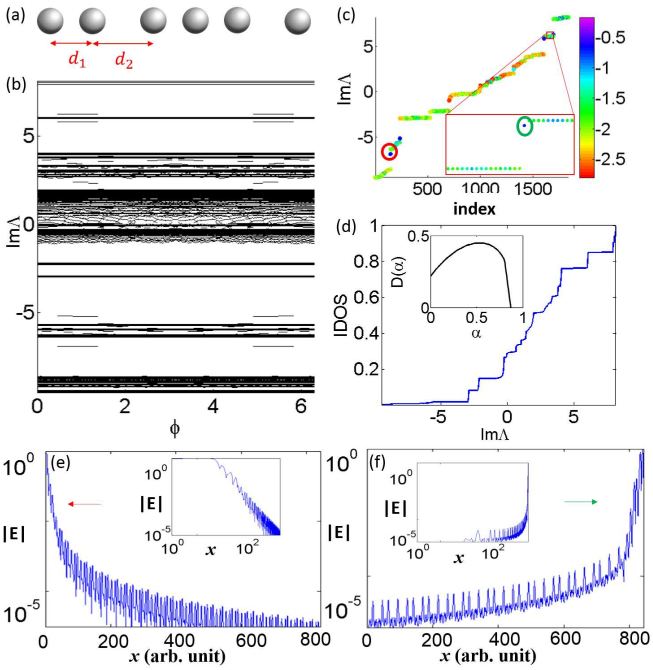

Figure 4·15: (a) Schematic illustration of a Fibonacci chain of point scatterers with binary distance modulation $d_2/d_1 = 2$; (b) Topological band-structure for the energy levels for a 610-particle Fibonacci chain. (c) Energy spectrum for the $\phi = 1$ case showing an edge-state in the gap. (d) Corresponding IDOS for the $\phi = 1$ case. The inset plots the singularity spectrum D(α) of the gap width distribution. (e) Edge mode with power-law decay and (f) edge mode with exponential localization (insets are in double-logarithmic scale).(Wang et al., 2018b) siderable interest in condensed matter theory (Macia, 2014; Hofstadter, 1976; Han et al., 1994) and have also been recently studied in optics (Verbin et al., 2015; Lucic et al., 2015). Here we address these systems using the vectorial Green's matrix method for the first time. We consider an optical scattering chain defined by the inter-particle separations:

$$d_n = d_0 \left[1 - \varepsilon \cos\left(\frac{2\pi}{n\tau} + \phi \right) \right], \tag{4.13}$$

where d_n is interpreted as the n-th inter-particle distance, $d_0 = 1$ is a scaling constant, $\varepsilon = 0.5$ is the coefficient that controls the strength of the modulation, $\tau = (\sqrt{5}+1)/2$ is the golden ratio, and ϕ is the topological parameter. Since τ is irrational, the spatial modulation is quasiperiodic. Moreover, when ϕ varies continuously between 0 and 2π, Eq. (4.13) describes an adiabatic deformation of the chain. The modulation defined in (4.13) is isomorphic to the Aubry-André or Harper model describing lattice systems in the presence of a gauge field (Hofstadter, 1976; Macia, 2014). A schematic illustration of a portion of the investigated Harper chain is shown in Fig. 4·14(a). In Fig. 4·14(b), we display the computed topological bandstructure obtained by varying the parameter ϕ from 0 to 2π. The bandstructure features a very rich distribution of energy band-gaps in the scattering spectra that are crossed by different numbers of edge-localized modes. In addition, at $Im\Lambda \simeq 5$ and when $\phi \simeq \pi$ we observe a crossing between two band-gap states that gives rise to a crossing, similar to a Dirac point (see magnified picture in the inset). The two crossing states are strongly localized at the two opposite edges of the chain. In Figs. 4·14(c)-(f) we study the energy spectrum for a Harper chain with $\phi = 3.05$, which is near the crossing point of two edge states. In Fig. 4·14(c), we plot the IPR color-coded imaginary part of the scattering eigenvalues against their indices in the chain, and the inset shows four strongly localized edge-states (doubly degenerate) inside the band-gap. Based on the imaginary part of the eigenvalues, we have also calculated the IDOS for the Harper chain, which is shown in Fig. 4·14(d). The IDOS displays a characteristic staircase structure where each plateau indicates the presence of an energy gap in the spectrum. We have identified each gap by applying the gap-labeling theorem using the relation (Baboux et al., 2017):

$$N = p + q\tau, \tag{4.14}$$

where τ is the golden number, p and q are integer labels. Besides, q can be interpreted as the topological Chern numbers of the labelled gaps (Baboux et al., 2017). In Figs. 4·14(e) and 4·14(f) we show the spatial profiles of two representative band-gap states that are strongly localized at the two edges of the chain. However, unlike the dimer case, the edge-localized states of the Harper chain display a characteristic power-law amplitude localization (see log-log plot in the inset of 4·14(f)) attributed to the fractal nature of the underlying eigenmodes.

We now discuss the scattering resonances of one-dimensional Fibonacci chains, which have been widely investigated due to their unique light transport and localization properties (Dal Negro et al., 2003). Moreover, such canonical structures recently attracted significant attention in relation to the topological properties of short-range coupled photonic waveguide systems (Levy and Akkermans, 2017; Baboux et al., 2017). A one-dimensional Fibonacci chain can be obtained as a special case of the Harper model equation (Kraus and Zilberberg, 2012; Baboux et al., 2017):

$$s_n = sgn\left[\cos\left(\frac{2n\pi}{\tau} + \phi\right) - \cos\left(\frac{\pi}{\tau}\right)\right], \tag{4.15}$$

where sgn denotes the sign operator of the argument that outputs only the binary values ±1, and τ is the golden mean. The s_n from Eq. 4.15 takes only two values, ±1, and are interpreted as a binary sequence of two different interparticle distances, d_1 and d_2. As a result, by varying the topological parameter ϕ, equivalent representations of

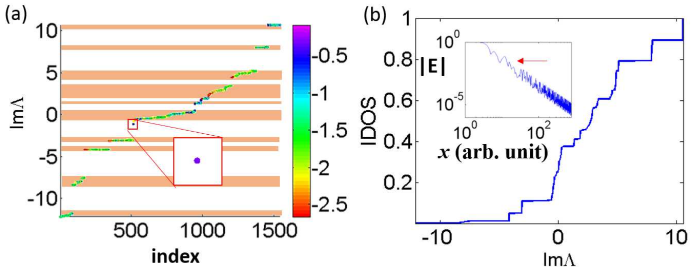

Figure 4·16: (a) Greens matrix energy spectrum and band-structure for a 512-particle Thue-Morse linear chain, with binary distance modulation $d_2/d_1 = 2$. The inset shows a magnified view of a band-gap state. (b) IDOS of the Thue-Morse chain, and edge-localized eigenstate inside the band gap (inset).(Wang et al., 2018b)

the Fibonacci chains can be generated. In Fig. 4·15(a) we illustrate a portion of the Fibonacci binary sequence. In Fig. 4·15(b) we vary the topological parameter ϕ from 0 to 2π and obtain the topological band diagram that features a rich distribution of energy band-gaps and gap-localized states. However, unlike in the case of the Harper chain, the structure of the Fibonacci chain flips abruptly when continuously varying the topological parameter ϕ due to the effect of the *sgn* operation in Eq. 4.15. These sudden structural transitions are known as phason flips (Levy et al., 2016).

By choosing the value $\phi = 1$, we show in Fig. 4·15(c) the distribution of the imaginary parts of the eigenvalues, and identify two edge-localized states residing in the band-gaps circled (see inset). The corresponding IDOS is displayed in Fig. 4·15(d), and consists of a fractal staircase of band-gap widths. The fractal nature of the gap-width distribution is demonstrated by the singularity spectrum shown in the inset, obtained by using the Wavelet Transform Modulus Maxima (WTMM) method described in (Dal Negro and Inampudi, 2017). In Fig. 4·15(e) we show the spatial distribution of the edge state highlighted by the red circle in Fig. 4·15(c), while in Fig. 4·15(f) we display the edge state inside the green circle in Fig. 4·15(c). It is evident that both states are strongly localized on the edges of the chain. However, we also notice that the amplitude in Fig. 4·15(e) decays as a power-law (see double logarithmic scale in the inset) while the state in Fig. 4·15(f) is exponentially localized, similarly to the dimer chain. Such a coexistence of two different localization regimes in a single physical system is a novel phenomenon driven by the long range correlation of the electromagnetic interactions, as captured by the vectorial Green's matrix.

The results obtained so far demonstrate that the presence of edge modes is a generic feature of electromagnetically coupled, one-dimensional chains with aperiodic order. However, topological parameters for more complex structures beyond quasi-periodic order, such as one-dimensional Thue-Morse chains, have not yet been reported. We address this challenge directly by computing the energy spectrum of the Thue-Morse chain, which unveils the presence of edge-localized band-gap states. This is achieved in Fig. 4·16(a) where the imaginary part of the Thue-Morse eigenvalues for a linear chain with $N = 512$ dipoles. We observe the presence of a single state in the band-gap near $Im\Lambda = 0$. Here, we are not able to obtain a full topological band-structure due to the lack of a known topological parameter for Thue-Morse systems. However, we report clear edge-localized states with power-law amplitude decay in the Thue-Morse energy gaps, similar to the Harper or Fibonacci chains. Finally, in Fig. 4·16(b) we show the IDOS of the Thue-Morse chain, which also displays a complex staircase structure. Further work beyond the scope of this contribution is needed in order to understand the nature of edge-localization in Thue-Morse structures.

4.4.3 Section summary

In conclusion, through the study of the vectorial Green's matrix spectra of electromagnetic scattering systems including analogs of SSH and Harper models, as well as aperiodic Fibonacci and Thue-Morse chains, we have unambiguously identified and characterized scattering edge modes. In particular, we have found crossing of modes localized on opposite edges inside band gaps, analogously to the crossing of edge states with opposite chirality in topological insulators. We have also discovered a novel power-law edge-mode localization in deterministic aperiodic one-dimensional scattering systems. Notably, Fibonacci chains are found to support both power-law and exponentially decaying edge states. Our work extends the concept of topological states to open electromagnetic scattering systems and fully demonstrates the potential of the vectorial Green's matrix method for the engineering of novel topological phenomena in collectively coupled electromagnetic structures and aperiodic metamaterials.

4.5 Vectorial Green's Matrix with Both Electric and Magnetic Dipole

In the previous sections, I have presented results using vectorial Green's matrix with only electric dipoles. However, for more general problems in optical nanostructure and metamaterial design, inclusion of magnetic dipole is crucial in order for a complete modeling of both effective electric and magnetic behaviors. Besides, when the size of the nanosphere is large, Mie theory predicts higher order multipoles contributing to the scattering problems (Bohren and Huffman, 1983). As a result, restricting the multiple scattering model to include only electric dipoles limits not only the complexity of single-elements but also our understanding of more general electromagnetic response of complex aperiodic media.

In order to include magnetic dipoles into the Green's matrix, it is important to know how the multiple scattering problem of coupled electric and magnetic dipoles is formulated. In particular, I use the next subsection to introduce the multiple scattering formulism (Mulholland et al., 1994; Garcia-Camara et al., 2010).

4.5.1 The coupled dipole approximation with both electric and magnetic dipoles

The electric and magnetic fields (in S.I. unit system) at the ith particle ($\mathbf{E}_i$ and $\mathbf{H}_i$ respectively) resulting from the electric ($\mathbf{p}$) and magnetic ($\mathbf{m}$) dipole moments at the jth particle are:

$$\mathbf{E}_i = a_{ij}\alpha_E\mathbf{E}_j + b_{ij}\alpha_E(\mathbf{E}_j \cdot \mathbf{n}_{ji})\mathbf{n}_{ji} - d_{ij}(\frac{\mu_0}{\epsilon_0})^{1/2}\alpha_H(\mathbf{n}_{ji} \times \mathbf{H}_j), \tag{4.16}$$

$$\mathbf{H}_i = a_{ij}\alpha_H\mathbf{H}_j + b_{ij}\alpha_H(\mathbf{H}_j \cdot \mathbf{n}_{ji})\mathbf{n}_{ji} + d_{ij}(\frac{\epsilon_0}{\mu_0})^{1/2}\alpha_E(\mathbf{n}_{ji} \times \mathbf{E}_j), \tag{4.17}$$

where Green's matrix terms are:

$$a_{ij} = \frac{1}{4\pi}\frac{e^{ikr_{ij}}}{r_{ij}}(k^2 - \frac{1}{r_{ij}^2} + \frac{ik}{r_{ij}}), \tag{4.18}$$

$$b_{ij} = \frac{1}{4\pi}\frac{e^{ikr_{ij}}}{r_{ij}}(-k^2 + \frac{3}{r_{ij}^2} - \frac{3ik}{r_{ij}}), \tag{4.19}$$

$$d_{ij} = \frac{1}{4\pi}\frac{e^{ikr_{ij}}}{r_{ij}}(k^2 + \frac{ik}{r_{ij}}), \tag{4.20}$$

In particular, d_{ij} is new and accounts for the cross interaction between the electric and magnetic part of the equations.

In order to solve practical problems involving coupled electric and magnetic dipoles, it is important to also specify material properties. For high-index dielectric nanospheres of sufficiently large size, induced currents in the nanosphere can create not only effective dielectric permittivity but also magnetic permeability (Mulholland et al., 1994; Bohren and Huffman, 1983). As correctly pointed out in Ref. (Lumme and Rohola, 1994), the electric and magnetic polarizability volumes are:

$$\alpha_E = \frac{3i}{2k^3}a_1, \tag{4.21}$$

and

$$\alpha_H = \frac{3i}{2k^3} b_1, \tag{4.22}$$

and k is the wavenumber of the background medium. The polarizability volumes have units of volume (e.g. m^3).

In Equations 4.21 and 4.22, a_1 and b_1 are the Mie coefficients for electric and magnetic dipoles (Bohren and Huffman, 1983), respectively. The νth order Mie coefficients can be expressed as (Bohren and Huffman, 1983):

$$a_\nu = \frac{n\psi_\nu(nkr)\psi'_\nu(kr) - \psi_\nu(kr)\psi'_\nu(nkr)}{n\psi_\nu(nkr)\xi'_\nu(kr) - \xi_\nu(kr)\psi'_\nu(nkr)}, \tag{4.23}$$

and

$$b_\nu = \frac{\psi_\nu(nkr)\psi'_\nu(kr) - n\psi_\nu(kr)\psi'_\nu(nkr)}{\psi_\nu(nkr)\xi'_\nu(kr) - n\xi_\nu(kr)\psi'_\nu(nkr)}, \tag{4.24}$$

where r is the radius of the spherical scatterer, and n is the relative refractive index of the nanosphere with respect to the background medium. $\psi_\nu(x)$ and $\xi_\nu(x)$ are Riccati-Bessel functions constructed from spherical bessel functions via $\psi_\nu(x) = xj_\nu(x)$ and $\xi_\nu(x) = xh_\nu^{(1)}(x)$. In addition, $j_\nu(x)$ is the spherical bessel function of the first type, and $h_\nu^{(1)}(x)$ is the spherical Hankel function of the first type.

From above, for N-scatterers, we can assemble linear system of equations for local fields $\mathbf{E}_i$ and $\mathbf{H}_i$ with given (local) incident fields $\mathbf{E}_{i,0}$ and $\mathbf{H}_{i,0}$ as:

$$\mathbf{E}_i = \mathbf{E}_{i,0} + \sum_{j\neq i}^{N} \alpha_{E,i}\tilde{C}_{ij}\mathbf{E}_j - (\frac{\mu_0}{\epsilon_0})^{1/2} \sum_{j\neq i}^{N} \alpha_{H_i}\tilde{f}_{ij}\mathbf{H}_j, \tag{4.25}$$

and

$$\mathbf{H}_i = \mathbf{H}_{i,0} + \sum_{j\neq i}^{N} \alpha_{H,i}\tilde{C}_{ij}\mathbf{H}_j + (\frac{\epsilon_0}{\mu_0})^{1/2} \sum_{j\neq i}^{N} \alpha_{E,i}\tilde{f}_{ij}\mathbf{E}_j, \tag{4.26}$$

where $\tilde{C}_{ij}$ is a 3×3 matrix block:

$$\begin{pmatrix} a_{ij} + b_{ij}(n_{ij}^x)^2 & b_{ij}n_{ij}^x n_{ij}^y & b_{ij}n_{ij}^x n_{ij}^z \\ b_{ij}n_{ij}^y n_{ij}^x & a_{ij} + b_{ij}(n_{ij}^y)^2 & b_{ij}n_{ij}^y n_{ij}^z \\ b_{ij}n_{ij}^z n_{ij}^x & b_{ij}n_{ij}^z n_{ij}^y & a_{ij} + b_{ij}(n_{ij}^z)^2 \end{pmatrix}$$

and $\tilde{f}_{ij}$ is also a 3×3 matrix block

$$\begin{pmatrix} 0 & -d_{ij}n_{ij}^z & d_{ij}n_{ij}^y \\ d_{ij}n_{ij}^z & 0 & -d_{ij}n_{ij}^x \\ -d_{ij}n_{ij}^y & d_{ij}n_{ij}^x & 0 \end{pmatrix}$$

When writing into the total matrix form, the E and H fields are assembled as a single column component-wise:

$$\begin{pmatrix} E_{1x} \\ E_{1y} \\ E_{1z} \\ H_{1x} \\ H_{1y} \\ H_{1z} \\ E_{2x} \\ \vdots \end{pmatrix}$$

and the full Green's matrix will have $6N \times 6N$ elements, in 6×6 blocks formed by $\tilde{C}_{ij}$ and $\tilde{f}_{ij}$.

Finally, based on the above formulation for coupled electric and magnetic dipoles, it is possible to calculate cross-sections from $\mathbf{p} = \alpha_E \mathbf{E}$ and $\mathbf{m} = \alpha_H \mathbf{H}$. In particular, the extinction cross-section is (the aterisk $*$ denotes complex conjugation):

$$C_{ext} = \frac{4\pi k}{|\mathbf{E}_0|^2} \sum_{i=1}^{N} Im[\mathbf{p}_i \cdot \mathbf{E}_{i,0}^* + \mathbf{m}_i \cdot \mathbf{H}_{i,0}^*], \tag{4.27}$$

and the absorption cross-section is:

$$C_{abs} = \frac{4\pi k}{|\mathbf{E}_0|^2} \sum_{i=1}^{N} [|\mathbf{E}_i|^2 (Im[\alpha_{E,i}] - \frac{2}{3}k^3 |\alpha_{E,i}|^2) + |\mathbf{H}_i|^2 (Im[\alpha_{H,i}] - \frac{2}{3}k^3 |\alpha_{H,i}|^2)] \tag{4.28}$$

and scattering cross-section is $C_{sca} = C_{ext} - C_{abs}$.

In addition, the scattering cross-section can also be computed via integrating the differential scattering cross-section over all solid angle Ω on a farfield sphere:

$$C_{sca} = \frac{k^2}{|\mathbf{E}_0|^2} \int |\sum_{i=1}^{N} e^{-ik\mathbf{n}\cdot\mathbf{r}_i} \{\mathbf{p}_i - [\mathbf{n}\cdot\mathbf{p}_i]\mathbf{n} - \mathbf{n}\times\mathbf{m}_i\}|^2 d\Omega, \qquad (4.29)$$

where $\mathbf{n}$ is the unit direction vector to the observation point.

In order to appreciate the importance of including magnetic dipoles, Fig. 4·17 I show the situation of a single Si nanosphere's (radius being $150nm$) scattering efficiency. In particular, I have used realistic material dispersion (Palik, 1998) for silicon and computed effective electric and magnetic polarizabilities from silicon's dielectric constants using Eqn. 4.21 and 4.22. In Fig. 4·17, I show that two peaks in scattering efficiency due to the electric ($\mathbf{p}$, dominating near $\lambda = 1100nm$, Fig. 4·17(f)) and magnetic ($\mathbf{m}$, dominating near $\lambda = 900nm$, Fig. 4·17(d)) dipole moments. Special attention is directed to the crossing between the electric and magnetic dipoles' scattering near $\lambda = 1200nm$. In this case, one would expect cancellation of backscattering (Staude et al., 2013; Liu et al., 2012). Indeed, as shown in Fig. 4·17(b), I plot the forward to backward ratio of scattered power, based on Eq. 4.29, there is a minimum point near $\lambda = 1200nm$. In the inset of Fig. 4·17(b), the backward part of the 3D radiation diagram can be appreciated by noticing the "dip" in the backward direction (i.e. $-z$ direction).

With this extended formulation of CDA including both electric magnetic dipoles, I have also computed cross-sections in Fig. 4·18. In particular, I compute the scattering, absorption and extinction efficiencies for golden-angle Vogel spiral ($\zeta = (\sqrt{5}+1)/2$ as defined in Chapter 3) in Fig. 4·18(a), and Penrose array (Penrose,) in Fig. 4·18(b), each with about 1000 identical Si nanospheres with the same size as in Fig. 4·17. Again, the double-peak character of having both electric and magnetic resonances in the spectra is demonstrated. Furthermore, in each case, I also plot the amplitude of

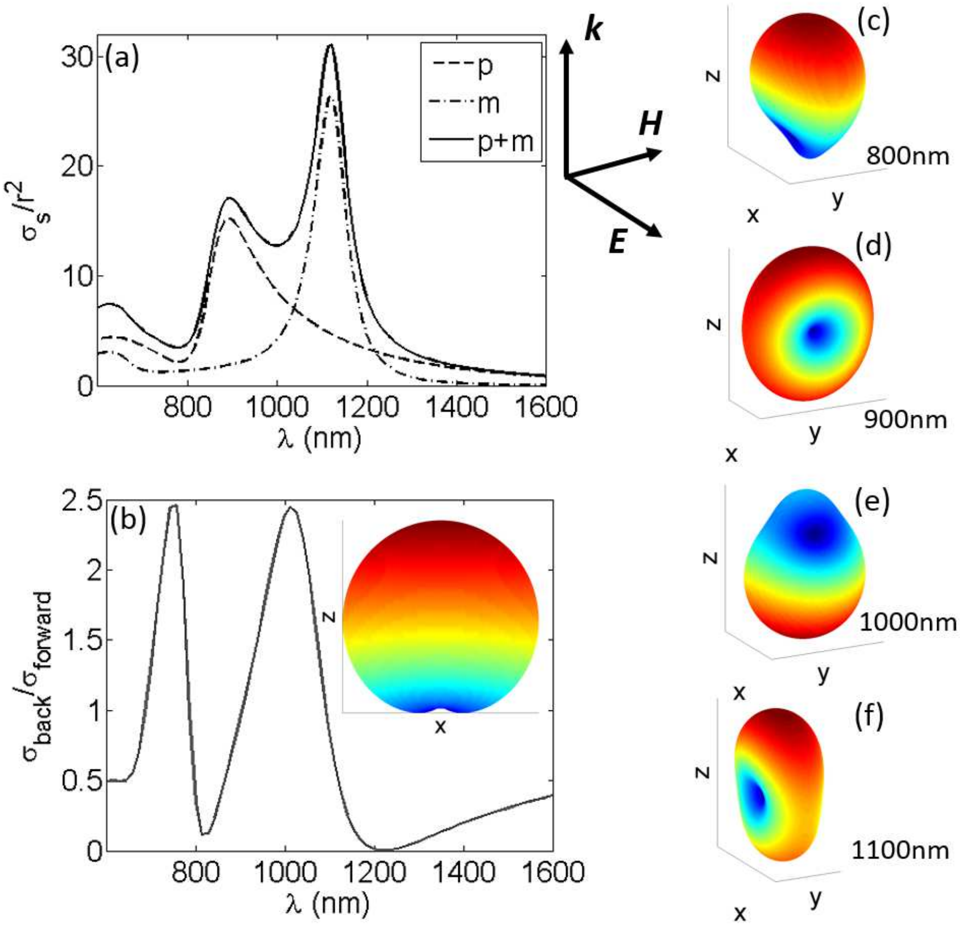

Figure 4·17: (a) shows the scattering efficiency spectrum normalized to radius (r = 150nm) of the silicon nanosphere. The electric (**p**) and magnetic (**m**) dipole components are indicated. (b) shows the forward to backward ratio of calculated radiation pattern (differential scattering cross-sections d/d). The inset shows the 3D radiation diagram at the p-m crossing near 1200nm, where backward radiation is zero. (c) to (f) shows 3D radiation diagrams at 800nm, 900nm, 1000nm, and 1100nm, respectively. In particular the radiation is dominated by magnetic dipole at900nm, and by electric dipole at 1100nm. The direction of $\{\mathbf{E}, \mathbf{H}, \mathbf{k}\}$ vector triplets for excitation, in relation to the indicated Cartesian coordinates are shown in the bottom-right corner.

the electric field distribution at the peak of each spectra near $\lambda = 1100nm$, where complex fractal-like physical modes upon plane wave excitation from the top of each nanostructure can be seen.

4.5.2 The Green's matrix with both electric and magnetic dipoles

The as shown previously, the vectorial Green's matrix for electric dipole decouples from the material properties (i.e. polarizability volumes α) of individual scatterers in the array. Besides, the form of Green's matrix of interest is normalized to be unitless, so that the results depend only on optical density and are scaling invariant. With theses in mind, the μ_0 and ϵ_0 in Eqs. 4.16 and 4.17 are set to be 1 (i.e. for relative electric and magnetic fields of the coupled system with respect to given incident fields).

As a result, the $6N \times 6N$ electromagnetic vectorial Green's matrix sub-blocks describing interactions between the n-th and m-th particles can be sub-divided into diagonal $3N \times 3N$ and off-diagonal $3N \times 3N$ blocks:

$$\begin{pmatrix} G^{ee}_{nm} & G^{eh}_{nm} \\ G^{he}_{nm} & G^{hh}_{nm} \end{pmatrix} \tag{4.30}$$

In particular, the diagonal blocks G^{ee}_{nm} and G^{hh}_{nm} have the same form as Eq. 4.6, while off diagonal terms $G^{he}_{nm} = -G^{eh}_{nm}$, and:

$$G^{he}_{nm} = \frac{1.5e^{ikr_{nm}}}{ikr_{nm}}(1 + \frac{i}{kr_{nm}})\Re, \tag{4.31}$$

where $\Re$ is:

$$\begin{pmatrix} 0 & -\widehat{r}^{z}_{nm} & \widehat{r}^{y}_{nm} \\ \widehat{r}^{z}_{nm} & 0 & -\widehat{r}^{x}_{nm} \\ -\widehat{r}^{y}_{nm} & \widehat{r}^{x}_{nm} & 0 \end{pmatrix} \tag{4.32}$$

and the superscripts x, y, z denote Cartesian components of unit directional vector $\widehat{\mathbf{r}}_{nm} = \mathbf{r}_{nm}/|\mathbf{r}_{nm}|$.

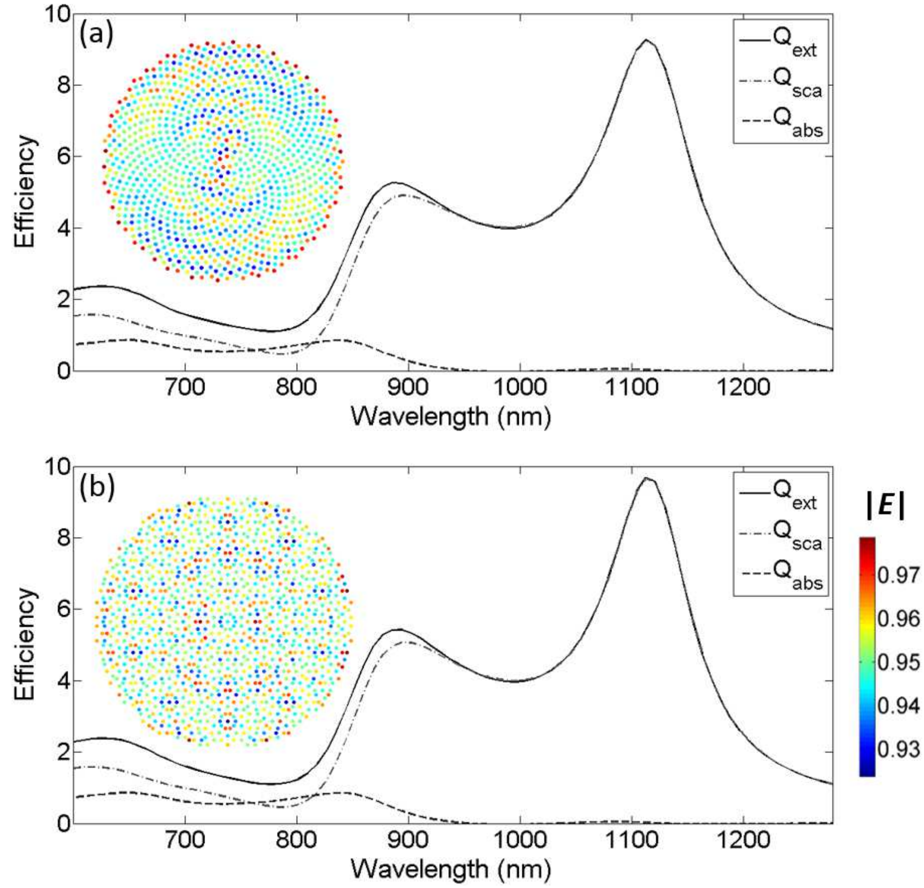

Figure 4·18: Scattering, absorption and extinction efficiencies calculated for (a) $N = 1000$ golden-angle Vogel spiral array, and (b) $N = 1108$ Penrose array (Penrose,). Both arrays are made of silicon nanospheres (Palik, 1998) with radius $150nm$ and minimum separation (center-to-center) of $350nm$ in the array. In this coupled dipole method, both electric and magnetic dipole moments induced in the nanospheres are considered. The effective dielectric permittivity and magnetic permeability are computed using Mie coefficients for electric and magnetic dipoles, respectively. Both insets show normalized electric field amplitudes are $1115nm$ for each case (maximum of scattering cross-sections), and the colorbar shows normalized scale for both insets.

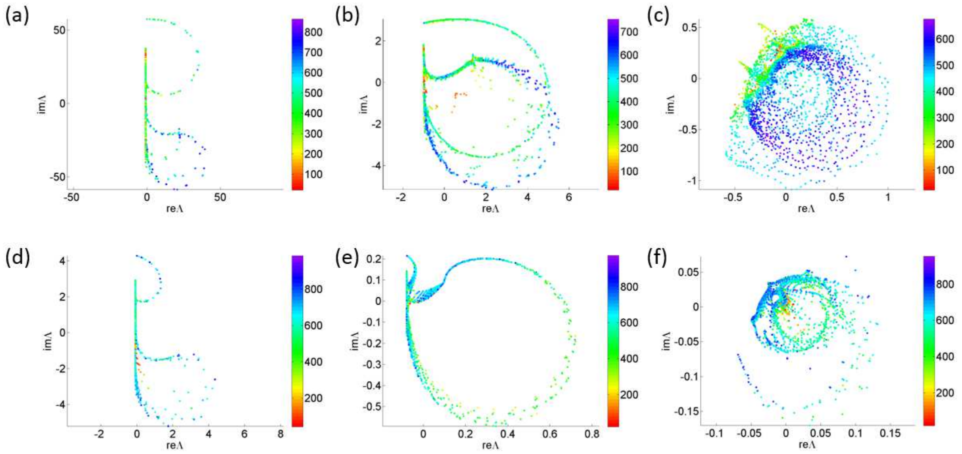

Figure 4·19: (a) to (c) are complex eigenvalues for $N = 1000$ golden-angle Vogel spiral using vectorial Green's matrix with only electric dipoles, for optical densities $\rho\lambda^2 = 100, 10, 0.5$, respectively. (d) to (f) are complex eigenvalues the same Vogel spiral using vectorial Green's matrix with both electric and magnetic dipoles, for optical densities $\rho\lambda^2 = 100, 10, 0.5$, respectively.

In Fig. 4·19, I show a representative comparison between eigenvalue distributions for the Green's matrix with only electric dipoles and those for the Green's matrix with both electric and magnetic dipoles. In particular, Figs. 4·19(a) to 4·19(c) are complex eigenvalues for $N = 1000$ golden-angle Vogel spiral, computed using vectorial Green's matrix with only electric dipoles, for optical densities $\rho\lambda^2 = 100, 10, 0.5$, respectively. On the other hand, Figs. 4·19(d) to 4·19(f) are complex eigenvalues for $N = 1000$ golden-angle Vogel spiral, computed using vectorial Green's matrix with both electric and magnetic dipoles, for optical densities $\rho\lambda^2 = 100, 10, 0.5$, respectively. In general, the main feature of spectral gap opening towards larger optical densities holds for both formulations, while spectral gap in the complex plane is far more pronounced in the cases where magnetic dipoles are included.

4.6 Chapter Summary

In this chapter, the Green's matrix method of coupled electric dipoles is introduced as a powerful tool to model and study complex aperiodic media. In particular, I applied the Green's matrix method to study complex-prime based 2D arrays, and revealed insightful information regarding frequency localization and fractal modes. In addition, with the examples of 1D aperiodic dipole chains, I demonstrate the relevance of using Green's matrix method in engineering topological metamaterial. Finally, in order to extend the capability of the Green's matrix method, I concluded my work by including the effect of magnetic dipoles.

Chapter 5

Conclusions

5.1 Summary of The Thesis

In this thesis, I have shown my works on direct and inverse designs of single nanoparticles resonances as well as nanostructures that can be understood as collective resonances.

In particular, I have addressed two questions for engineering single nanoparticle element: (I) what is the optimal nanoparticle shape for a given optical functionality? (II) what is the nature of a given resonance? To address the first question, I have used my work in collaboration with the University of Utah on optimizing the single plasmonic nanoparticle shape for optimal surface field enhancement. For the second question, I used multipolar decomposition method including the toroidal dipole moment to show the nature of resonances in high-index dielectric nanodisks and nanopixels, and used the findings to engineer absorption through anapoles.

At the array level, various of my past works, including broadband gold-nanofiber electrodes, multiband fractal-nanoantenna sensors, and gold nanohelix with polarization and direction control, have demonstrated the importance of understanding and modeling collective resonances for the design of optical nanostructures and metamaterials. On the other hand, these works point to a more controllable and theoretically straightforward paradigm of designing complex optical media using the concept of arrays. By decoupling the resonance engineering of single particle from that of the array geometry, metamaterials and metasurfaces can be modeled and designed as point arrays formed by identical elements.

Motivated by this paradigm, the Green's matrix spectral method is introduced as a powerful tool to study coupled dipolar elements in arbitrary arrays. In particular, I applied the Green's matrix method to study complex-prime based 2D arrays, and revealed insightful information regarding frequency localization and fractal modes. I also show the relevance of using Green's matrix method in engineering topological metamaterial with the examples of 1D aperiodic dipole chains. Finally, in order to extend the capability of the Green's matrix method, I concluded my work by including the effect of magnetic dipoles.

5.2 Outlook for Future Works

Green's matrix method provides universal geometry-induced electromagnetic properties of complex aperiodic systems, and has been efficiently applied to understanding and engineering of large-scale aperiodic media. Currently, I have extended the existing Green's matrix method for coupled vectorial electric dipoles to include also vectorial magnetic dipoles. This extension greatly expanded the validity limit of the model, and makes it especially useful for modeling high-index dielectric nanoparticle clusters. On the other hand, it would be desirable to as a future work explore the possibility of including higher order multipole moments in the Green's matrix. This would not only make the Green's matrix method more powerful, correspondingly, the existing CDA will also be extended to model more general multiple scattering problems with coupled-multipoles. Some existing studies that are useful for future researches in this direction include Refs. (Yurkin and Hoekstra, 2007; Kallos et al., 2012; Bourrely et al., 1992).

Besides, from an engineering point of view, it would be interesting to ask about the potential to inversely engineer geometries for photonic-plasmonic applications from desired Green's matrix spectra. One potential approach draws inspiration from the mass-spring model where only nearest neighbor coupling is relevant. In this case, inverse problems can be solved rigorously through Lanczos algorithms (Chu and Golub, 2005), and coupling constants from a given Hamiltonian matrix can be found. As described in the Chapter 4 of Ref. (Gladwell, 2004), starting from a diagonal matrix A made of known eigenvalues, as well as one eigenstate, it is possible recover the three-diagonal matrix that describes the interactions of a one-dimensional mechanical chain. Similarly, for Green's matrix of simple one-dimensional scattering system with weak coupling, we may approximate the system's electromagnetic interactions using a three-diagonal scalar Green's matrix. In this case, with desired eigenvalues, we can infer the terms in the Green's matrix, which is computed based on the inter-particle distance r_{ij} through $g_{ij} = \frac{\exp(ikr_{ij})}{ikr_{ij}}$. However, considering only an approximated Green's matrix in three-diagonal form does not fully describe the electromagnetic interaction between all scatterer pairs, and greatly limits the system to very weakly coupled regime. In addition, as I will discuss below, the set of recovered r_{ij} from the Green's matrix may not permit physically feasible geometries in 1D, or even 2D or 3D.

Although beyond the scope of the this thesis, I would like to discuss the possibility of solving inverse problems involving full Green's matrix. To demonstrate this point, we can assume a (scalar) Green's matrix (Rusek et al., 2000) is given for two particles, and the Euclidean distance between the two particles is $r = |\mathbf{r}_1 - \mathbf{r}_2|$. First of all, a physical scalar Green's matrix for this system is 2×2, symmetric, with zeros diagonal elements and complex-valued off-diagonal elements $g_{12} = g21$. Therefore, the problem can be further reduced to computing r from $g_{12} = exp(ikr)/(ikr)$ (k being the wavenumber). Fortunately, this problem has analytical solutions, known as Lambert-W functions (Dence, 2013), and real r can be calculated analytically. Once

r is found, by fixing the coordinate of one particle in the dimer system (a property of geometrical invariance), the other scatterer's position can be found. For a more general complex array, solution will be the set of distances between each pair of scatterers in the array. This is known as the distance geometry problem commonly encountered in determining molecular structures (Lavor et al., 2017). Now, considering a hypothetical 1D chain that is required to be described by an arbitrary 3 by 3 Green's matrix, from a given set of three eigenvalues. In this case, we can get three pair-wise distance information, $r_{12} = r_{21}$, $r_{13} = r_{31}$, and $r_{23} = r_{32}$ (assuming $r_{12} \leq r_{23} \leq r_{13}$). It is obvious from the geometry point of view, the likelihood of collinear condition $r_{13} + r_{23} = r_{13}$ is very slim. As a result, the general physical structure with 3 eigenvalues (i.e. 3 scatterers from the scalar Green's matrix) is a triangle, which needs at least 2 spatial dimensions to specify. From this, it is evident that an arbitrary set of N eigenvalues will result in a Green's matrix describing a point system that exists in $N - 1$ dimensions in general. This implies that, eigenvalues of a Green's matrix cannot be arbitrary as one desires, while the method of interpreting Green's matrix inverse problem as a distance geometry problem is generally valid. This observation is equally true if one is to assume an approximate three-diagonal scalar Green's matrix for weakly one-dimensional chain. Without additional information or constraints, freely choosing eigenvalues will almost certainly results in geometric solutions that contradict the one-dimensional assumption. For vectorial Green's matrices, the inverse problem is likely more complicated, and researches in this direction is certainly exciting and meaningful from a rigorous inverse engineering point of view.

References

Abe, S. and Hiramoto, H. (1987). Fractal dynamics of electron wave packets in one-dimensional quasiperiodic systems. *Physical Review A*, 36:5349.

Adam, J. A. (2009). *A Mathematical Nature Walk*. Princeton University Press: Princeton, NJ, USA.

Adams, B. M., Ebeida, M. S., Eldred, M., Jakeman, J. D., Maupin, K. A., Monschke, J. A., Swiler, L. P., Stephens, J. A., Vigil, D. M., Wildey, T., Bohnhoff, W. J., Dalbey, K. R., Eddy, J. P., Hooper, R. W., Hu, K. T., and Ridgway, E. M. (2016). Dakota, a multilevel parallel object-oriented framework for design optimization, parameter estimation, uncertainty quantification, and sensitivity analysis: Version 6.4 users manual.

Afanasiev, G. N. (1993). Toroidal solenoids in an electromagnetic field and toroidal aharonov-casher effect. *Physica Scripta*, 48(4):385–392.

Afanasiev, G. N. (1994). Vector solutions of the laplace equation and the influence of helicity on aharonov-bohm scattering. *Journal of Physics A: Mathematical and General*, 27:2143–2160.

Afanasiev, G. N. (2001). Simplest sources of electromagnetic fields as a tool for testing the reciprocity-like theorems. *Journal of Physics D: Applied Physics*, 34:539–559.

Afanasiev, G. N. and Dubovik, V. M. (1998). Some remarkable charge-current configurations. *Physics of Particles and Nuclei*, 29:366–391.

Akkermans, E., Gero, A., and Kaiser, R. (2008). Photon localization and dicke superradiance in atomic gases. *Physical Review Letters*, 101:103602.

Akselrod, G. M., Argyropoulos, C., Hoang, T. B., Ciraci, C., Fang, C., Huang, J., Smith, D. R., and Mikkelsen, M. H. (2014). Probing the mechanisms of large purcell enhancement in plasmonic nanoantennas. *Nature Photonics*, 8:1–15.

Albuquerque, E. L. and Cottam, M. G. (2003). Theory of elementary excitations in quasiperiodic structures. *Physics Reports*, 376:225–337.

Alonso-González, P., Albella, P., Neubrech, F., Huck, C., Chen, J., Golmar, F., Casanova, F., Hueso, L. E., Pucci, A., Aizpurua, J., and Hillenbrand, R. (2013). Experimental verification of the spectral shift between near- and far-field peak intensities of plasmonic infrared nanoantennas. *Physical Review Letters*, 110:203902.

Alu, A. (2011). Restoring the physical meaning of metamaterial constitutive parameters. *Physical Review B*, 83:081102(R).

Alu, A. and Engheta, N. (2008). Plasmonic and metamaterial cloaking: physical mechanisms and potentials. *Journal of Optics A: Pure and Applied Optics*, 10(9):093002.

Alù, A. and Engheta, N. (2009). Cloaking a sensor. *Physical Review Letters*, 102:233901.

Apostol, T. (1976). *Introduction to Analytic Number Theory, 2nd Edition.* Springer-Verlag NY.

Asboth, J. K., Oroszlany, L., and Palyi, A. (2016). *A Short Course on Topological Insulators: Band Structure and Edge States in One and Two Dimensions.* Springer International Publishing.

Aslan, E., Aslan, E., Wang, R., Hong, M. K., Erramilli, S., Turkmen, M., Saracoglu, O. G., and Dal Negro, L. (2016). Multispectral cesaro-type fractal plasmonic nanoantennas. *ACS Photonics*, 3(11):2102–2111.

Ayala-Orozco, C., Liu, J. G., Knight, M. W., Wang, Y., Day, J. K., Nordlander, P., and Halas, N. J. (2014). Fluorescence enhancement of molecules inside a gold nanomatryoshka. *Nano Letters*, 14:2926–2933.

Baake, M. and Grimm, U. (2013). *Quasicrystals and Geometry.* Cambridge University Press: New York, NY, USA.

Baboux, F., Levy, E., Lemaitre, A., Gmez, C., Galopin, E., Gratiet, L. L., Sagnes, I., A. Amo, J. B., and Akkermans, E. (2017). Measuring topological invariants from generalized edge states in polaritonic quasicrystals. *Physical Review B*, 95:161114(R).

Bak, P., Tang, C., and Wiesenfeld, K. (1987). Self-organized criticality: an explanation of 1/f noise. *Physical Review Letters*, 59:381.

Balanis, C. A. (2005). *Antenna Theory: Analysis and Design, 3rd Edition.* John Wiley and Sons, Canada.

Bandres, M. A., Rechtsman, M. C., and Segev, M. Topological photonic quasicrystals: Fractal topological spectrum and protected transport. *Physical Review X*, 6.

Bao, Y., Zhu, X., and Fang, Z. (2015). Plasmonic toroidal dipolar response under radially polarized excitation. *Scientific Reports*, 5:11793.

Barthelemy, P., Bertolotti, J., and Wiersma, D. S. (2008). A lvy flight for light. *Nature*, 453:495–498.

Basharin, A. A., Kafesaki, M., Economou, E. N., Soukoulis, C. M., Fedotov, V. A., Savinov, V., and Zheludev, N. I. (2015). Dielectric metamaterials with toroidal dipolar response. *Physical Review X*, 5:011036.

Batty, M. and Longley, P. (1994). *Fractal Cities: A Geometry of Form and Function.* Academic Press: San Diego, CA.

Bharadwaj, P., Deutsch, B., and Novotny, L. (2009). Optical antennas. *Advances in Optics and Photonics*, 1:438–483.

Bharadwaj, P., Novotny, L., Bharadwaj, P., and Novotny, L. (2007). Spectral dependence of single molecule fluorescence enhancement. *Optics Express*, 15:14266.

Bohren, C. F. and Huffman, D. (1983). *Absorption and scattering of light by small particles.* Wiley.

Boriskina, S. and Dal Negro, L. (2008a). Optical gap formation and localization properties of optical modes in deterministic aperiodic photonic structures. *Optics Express*, 16:18813.

Boriskina, S. and Dal Negro, L. (2008b). Sensitive label-free biosensing using critical modes in aperiodic photonic structures. *Optics Express*, 16:12511.

Boriskina, S. V., Gopinath, A., and Negro, L. D. (2008). Optical gaps, mode patterns and dipole radiation in two-dimensional aperiodic photonic structures. *Optics Express*, 16:18813–18826.

Bouman, C. A. and Sauer, K. (1996). A unified approach to statistical tomography using coordinate descent optimization. *IEEE Transactions on image processing*, 5(3):480–492.

Bourrely, C., Chiappetta, P., Lemaire, T., and Torrésani, B. (1992). Multidipole formulation of the coupled dipole method for electromagnetic scattering by an arbitrary particle. *Journal of the Optical Society of America. A, Optics, Image Science, and Vision*, 9(8):1336–1340.

Breheny, P. and Huang, J. (2011). Coordinate descent algorithms for nonconvex penalized regression, with applications to biological feature selection. *The annals of applied statistics*, 5(1):232.

Brongersma, M. L. and Kik, P. G. (2007). *Surface Plasmon Nanophotonics.* Springer, Dordrecht, The Netherlands.

Busson, M. P., Rolly, B., Stout, B., Bonod, N., and Bidault, S. (2012). Accelerated single photon emission from dye molecule-driven nanoantennas assembled on dna. *Nature Communications*, 3:962.

Cao, L., White, J. S., Park, J., Schuller, J. A., Clemens, B. M., and Brongersma, M. L. (2009). Engineering light absorption in semiconductor nanowire devices. *Nature Materials*, 8:643–647.

Capretti, A., Walsh, G. F., Minissale, S., Trevino, J., Forestiere, C., Miano, G., and Dal Negro, L. (2012). Multipolar second harmonic generation from planar arrays of au nanoparticles. *Optics Express*, 20(14):15797–15806.

Casadei, A., Llado, E. A., Amaduzzi, F., Russo-Averchi, E., Ruer, D., Heiss, M., Dal Negro, L., and Morral, A. F. i. (2015). Polarization response of nanowires a la carte. *Scientific Reports*, 5:7651.

Caswell, K. K., Wilson, J. N., Bunz, U. H. F., and Murphy, C. J. (2003). Preferential end-to-end assembly of gold nanorods by biotin-streptavidin connectors. *Journal of the American Chemical Society*, 125:13914–13915.

Cesàro, E. (1905). *Remarques sur la courbe de Von Koch.* Tipografia della R. Accademia delle scienze fisiche e matematiche.

Chang, J.-Y., Wu, H., Chen, H., Ling, Y.-C., and Tan, W. (2005). Oriented assembly of au nanorods using biorecognition system. *Chemical Communications*, 8:1092–1094.

Chen, D., Zhang, R., Wang, R., Dal Negro, L., and Minteer, S. D. (2016). Gold nanofiber-based electrodes for plasmon-enhanced electrocatalysis. *Journal of The Electrochemical Society*, 163(14):H1132–H1135.

Christofi, A. C., Pinheiro, F. A., and Dal Negro, L. (2016). Probing scattering resonances of vogels spirals with the greens matrix spectral method. *Optics Letters*, 41(9):1933–1936.

Chu, M. T. and Golub, G. H. (2005). *Inverse Eigenvalue Problems: Theory, Algorithms, and Applications.* Oxford University Press, UK.

Ciattoni, A., Rizza, C., and Palange, E. (2010). Extreme nonlinear electrodynamics in metamaterials with very small linear dielectric permittivity. *Physical Review A*, 81:043839.

Ciattoni, A. and Spinozzi, E. (2012). Efficient second-harmonic generation in micrometer-thick slabs with indefinite permittivity. *Physical Review A*, 85:043806.

Collings, P. J. (2002). *Liquid Crystal: Natures Delicate Phase of Matter, 2nd Ed.* Princeton University Press, USA.

Conway, J. H. and Smith, D. A. *On quaternions and octonions: their geometry, arithmetic, and symmetry.* A. K. Peters: Natick, Massachusetts, USA:.

Dal Negro, L. (2014). *Optics of Aperiodic Structures: Fundamentals and Device Applications.* Pan Stanford Publishing: Singapore.

Dal Negro, L. and Boriskina, S. V. (2012). Deterministic aperiodic nanostructures for photonics and plasmonics applications. *Laser Photonics Review*, 6:178–218.

Dal Negro, L. and Feng, N. N. (2007). Spectral gaps and mode localization in fibonacci chains of metal nanoparticles. *Optics Express*, 15:14396.

Dal Negro, L. and Inampudi, S. (2017). Fractional transport of photons in deterministic aperiodic structures. *Scientific Reports*, 7(2259).

Dal Negro, L., Lawrence, N., and Trevino, J. (2012). Analytical light scattering and orbital angular momentum spectra of arbitrary vogel spirals. *Optics Express*, 20(16):18209–18223.

Dal Negro, L., Oton, C. J., Gaburro, Z., Pavesi, L., Johnson, P., Lagendijk, A., Righini, R., Colocci, M., and Wiersma, D. S. (2003). Light transport through the band-edge states of fibonacci quasicrystals. *Physical Review Letters*, 90:055501.

Dal Negro, L., Wang, R., and Pinheiro, F. A. (2016). Structural and spectral properties of deterministic aperiodic optical structures. *Crystal*, 6(12):161.

Dal Negro, L., Yi, J. H., Nguyen, V., Yi, Y., Michel, J., and Kimerling, L. C. (2005). Spectrally enhanced light emission from aperiodic photonic structures. *Applied Physics Letters*, 86:261905.

de Broglie, L. (1955). *Physics and microphysics.* Hutchinson's Scientific and Technical Publications.

de Bruijn, N. (1981). Algebraic theory of penrose's non-periodic tilings of the plane. ii. *Indagationes Mathematicae (Proceedings)*, 84(1):53 – 66.

Dence, T. P. (2013). A brief look into the lambert w function. *Applied Mathematics*, 4(6).

Devaney, A. J. (2012). *Mathematical Foundations of Imaging, Tomography and Wavefield Inversion.* Cambridge Press, UK.

Devaney, A. J. and Wolf, E. (1973). Radiating and nonradiating classical current distributions and the fields they generate. *Physical Review D*, 8(4):1044–1047.

Dicke, R. H. (1954). Coherence in spontaneous radiation processes. *Physical Review*, 93:99.

Dong, Z., Ni, P., Zhu, J., Yin, X., and Zhang, X. (2012). Toroidal dipole response in a multifold double-ring metamaterial. *Optics Express*, 20:13065–13070.

Dong, Z., Zhu, J., Yin, X., Li, J., Lu, C., and Zhang, X. (2013). All-optical hall effect by the dynamic toroidal moment in a cavity-based metamaterial. *Physical Review B*, 87:245429.

Dubovik, V. M., Martsenyuk, M. A., and Saha, B. (2000). Material equations for electromagnetism with toroidal polarizations. *Physical Review E*, 61:7087.

Dubovik, V. M., Tosunyan, L. A., and Tugushev, V. V. (1986). Axial toroidal moments in electrodynamics and solid-state physics. *Zhurnal Eksperimentalnoi i Teoreticheskoi Fiziki*, 90:590–605.

Dubovik, V. M. and Tugushev, V. V. (1990). Toroid moments in electrodynamics and solid-state physics. *Physics Reports*, 187:145.

Dulea, M., Johansson, M., and Riklund, R. (1992). Localization of electrons and electromagnetic waves in a deterministic aperiodic system. *Physical Review B*, 45:105.

Dyson, F. (2009). Birds and frogs. *Notices of the AMS*, 56(212).

Edwards, B., Alù, A., Young, M. E., Silveirinha, M., and Engheta, N. (2008). Experimental verification of epsilon-near-zero metamaterial coupling and energy squeezing using a microwave waveguide. *Physical Review Letters*, 100:033903.

Efimov, V. (1970). Energy levels arising from resonant two-body forces in a three-body system. *Phys. Lett. B*, 33(8):563–564.

Fernandez-Corbaton, I., Nanz, S., and Rockstuhl, C. On the dynamic toroidal multipoles from localized electric current distributions. *Scientific Reports*, 7(7527).

Flake, G. W. (1998). *The Computational Beauty of Nature: Computer Explorations of Fractals, Chaos, Complex Systems, and Adaptation.* The MIT Press: Cambridge, MA,.

Forestiere, C., He, Y., Wang, R., Kirby, R. M., and Dal Negro, L. (2016). Inverse design of metal nanoparticles' morphology. *ACS Photonics*, 3(1):68–78.

Forestiere, C., Iadarola, G., Rubinacci, G., Tamburrino, A., Dal Negro, L., and Miano, G. (2012). Surface integral formulations for the design of plasmonic nanostructures. *Journal of the Optical Society of America. A, Optics, Image Science, and Vision*, 29(11):2314–2327.

Forestiere, C., Miano, G., Boriskina, S. V., and Dal Negro, L. (2009a). The role of nanoparticle shapes and deterministic aperiodicity for the design of nanoplasmonic arrays. *Optics Express*, 17:9648.

Forestiere, C., Miano, G., Rubinacci, G., and Dal Negro, L. (2009b). Role of aperiodic order in the spectral, localization, and scaling properties of plasmon modes for the design of nanoparticle arrays. *Physical Review B*, 79:085404.

Friedman, J., Hastie, T., and Tibshirani, R. (2010). Regularization paths for generalized linear models via coordinate descent. *Journal of statistical software*, 33(1):1.

Fu, Y., Zhang, J., and Lakowicz, J. R. (2010). Plasmon-enhanced fluorescence from single fluorophores end-linked to gold nanorods. *Journal of the American Chemical Society*, 132:5540–5541.

Gansel, J. K., Thiel, M., Rill, M. S., Decker, M., Badea, K., Saile, V., von Freymann, G., Linden, S., and Wegener, M. (2009). Gold helix photonic metamaterial as broadband circular polarizer. *Science*, 325:1513.

Gansel, J. K., Wegener, M., Burger, S., and Linden, S. (2010). Gold helix photonic metamaterials: A numerical parameter study. *Optics Express*, 18(2).

Garcia-Camara, B., Moreno, F., Gonzalez, F., and Martin, O. J. F. (2010). Light scattering by an array of electric and magnetic nanoparticles. *Optics Express*, 18(10):10001–10015.

Gellerman, W., Kohmoto, M., Sutherland, B., and Taylor, P. C. (1994). Localization of light waves in fibonacci dielectric multilayers. *Physical Review Letters*, 72:633.

Gibbs, J. G., Mark, A. G., Eslami, S., and Fischer, P. (2013). Plasmonic nanohelix metamaterials with tailorable giant circular dichroism. *Applied Physics Letters*, 103:213101.

Gielis, J. (2003). A generic geometric transformation that unifies a wide range of natural and abstract shapes. *American Journal of Botany*, 90(3):333–338.

Gielis, J., Haesen, S., and Verstraelen, L. (2005). Universal shapes: from the supereggs of Piet Hein to the cosmic egg of George Lemaitre. *Kragujevac Journal of Mathematics*, 28:55–67.

Gladwell, G. M. L. (2004). *Inverse Problems in Viberation.* Springer, USA.

Goetschy, A. and Skipetrov, S. E. (2011). Non-hermitian euclidean random matrix theory. *Physical Review E*, 84:011150.

Gordon, R., Brolo, A. G., McKinnon, A., Rajora, A., Leathem, B., , and Kavanagh, K. L. (2004). Strong polarization in the optical transmission through elliptical nanohole arrays. *Physical Review Letters*, 92.

Gottheim, S., Zhang, H., Govorov, A. O., and Halas, N. J. (2015). Fractal nanoparticle plasmonics: The cayley tree. *ACS Nano*, 9:3284–3292.

Govorov, A. O., Bryant, G. W., Zhang, W., Skeini, T., Lee, J., Kotov, N., Slocik, J. M., and Naik, R. R. (2006). . exciton plasmon interaction and hybrid excitons in semiconductor metal nanoparticle assemblies. *Nano Letters*, 6:98–994.

Graglia, R. D. (1993). On the numerical integration of the linear shape functions times the 3-d green's function or its gradient on a plane triangle. *IEEE Transactions on Antennas and Propagation*, 41(10):1448–1455.

Guerin, C.-A., Mallet, P., and Sentenac, A. (2006). Effective-medium theory for finite-size aggregates. *Journal of the Optical Society of America A*, 23(2):349–358.

Guo, K., Du, M., Osorio, C. I., and Koenderink, A. F. (2017). Broadband light scattering and photoluminescence enhancement from plasmonic vogel's golden spirals. *Laser and Photonics Reviews*, 11(3):1600235.

Haake, F. (2010). *Quantum Signitures of Chaos, Third Revised and Enlarged Edition.* Springer-Verlag Berlin Heidelberg.

Han, J. H., Thouless, D. J., Hiramoto, H., and Kohmoto, K. (1994). Critical and bicritical properties of harper's equation with next-nearest-neighbor coupling. *Physical Review B*, 50:11365.

Hardy, G. H. and Wright, E. M. (2006). *An introduction to the theory of numbers, 6th Edition.* Oxford University Press, Oxford.

Harrington, R. F. and Harrington, J. L. (1996). *Field Computation by Moment Methods.* Oxford University Press.

Ho, C. M. and Scherrer, R. J. (2013). Anapole dark matter. *Physics Letters, Section B: Nuclear, Elementary Particle and High-Energy Physics*, 722:341–346.

Hoffmann, J., Hafner, C., Leidenberger, P., Hesselbarth, J., and Burger, S. (2009). Comparison of electromagnetic field solvers for the 3d analysis of plasmonic nanoantennas. *Proceedings of SPIE*, 7390:73900J.

Hofstadter, D. R. (1976). Energy levels and wave functions of bloch electrons in rational and irrational magnetic fields. *Physical Review B*, 14:2239.

Hohenester, U.; Trugler, A. (2012). Mnpbem - a matlab toolbox for the simulation of plasmonic nanoparticles. *Chem. Rev.*, 183:370–381.

Hsieh, C.-J., Chang, K.-W., Lin, C.-J., Keerthi, S. S., and Sundararajan, S. (2008). A dual coordinate descent method for large-scale linear svm. In *Proceedings of the 25th international conference on Machine learning*, pages 408–415. ACM.

Huang, Y.-W., Chen, W. T., Wu, P. C., Fedotov, V., Savinov, V., Ho, Y. Z., Chau, Y.-F., Zheludev, N. I., and Tsai, D. P. (2012). Design of plasmonic toroidal metamaterials at optical frequencies. *Optics Express*, 20:1760–1768.

Hurwitz, A. (1919). *Vorlesungen uber die Zahlentheorie der Quaternionen.* Berlin: J. Springer.

Jackson, J. D. (1999). *Classical electrodynamics.* Wiley, New York, NY, 3rd ed. edition.

Jin, Y. and Gao, X. (2014). Plasmonic fluorescent quantum dots. *Nature Nanotechnology*, 4:571–576.

Johnson, P. B. and Christy, R. W. (1972). Optical constants of the noble metals. *Physical Review B*, 6:4370–4379.

Jones, D. R., Schonlau, M., and Welch, W. J. (1998). Efficient global optimization of expensive black-box functions. *Journal of Global Optimization*, 13(4):455–492.

Kaelberer, T., Fedotov, V. A., Papasimakis, N., Tsai, D. P., and Zheludev, N. I. (2010). Toroidal dipolar response in a metamaterial. *Science*, 330:1510.

Kallos, E., Chremmos, I., and Yannopapas, V. (2012). Resonance properties of optical all-dielectric metamaterials using two-dimensional multipole expansion. *Physical Review B*, 86:245108.

Ketzmerick, R., Kruse, K., and S. Kraut, T. G. (1997). What determines the spreading of a wave packet? *Physical Review Letters*, 79:1959.

Kim, J., Naik, G. V., Emani, N. K., Guler, U., and Boltasseva, A. (2013). Plasmonic resonances in nanostructured transparent conducting oxide films. *IEEE Journal of Selected Topics in Quantum Electronics*, 19(3):4601907–4601907.

Kim, K. and Wolf, E. (1986). Non-radiating monochromatic sources and their fields. *Optics Communications*, 59:1.

Kinkhabwala, A., Yu, Z., Fan, S., Avlasevich, Y., Mullen, K., and Moerner, W. E. (2009). Large single-molecule fluorescence enhancements produced by a bowtie nanoantenna. *Nature Photonics*, 3:654–657.

Kohmoto, M. and Kadanoff, L. P. (1983). Localization problem in one dimension: Mapping and escape. *Physical Review Letters*, 50:1879.

Kohmoto, M., Sutherland, B., and Iguchi, K. (1987a). Localization in optics: Quasiperiodic media. *Physical Review Letters*, 58:2436.

Kohmoto, M., Sutherland, B., and Tang, C. (1987b). Critical wave functions and a cantor-set spectrum of a one-dimensional quasicrystal model. *Physical Review B.*, 35:1020.

Kosako, T., Kadoya, Y., and Hofmann, H. F. (2010). Directional control of light by a nano-optical yagiuda antenna. *Nature Photonics*, 312:312–315.

Kraus, J. D. (1949). The helical antenna. *Proceedings of the IRE*, 37:263–272.

Kraus, J. D. and Marhefka, R. J. (2001). *Antennas For All Applications, 3rd Edition.* McGraw-Hill Education, Singapore.

Kraus, Y. E. and Zilberberg, O. (2012). Topological equivalence between the fibonacci quasicrystal and the harper model. *Physical Review Letters*, 109(11):116404.

Kuzyk, A., Schreiber, R., Fan, Z., Pardatscher, G., Roller, E., Hgele, A., Simmel, F. C., Govorov, A. O., and Liedl, T. (2012). Dna-based self-assembly of chiral plasmonic nanostructures with tailored optical response. *Nature*, 483:311–314.

Kyrola, A., Bickson, D., Guestrin, C., and Bradley, J. K. (2011). Parallel coordinate descent for l1-regularized loss minimization. In *Proceedings of the 28th International Conference on Machine Learning (ICML-11)*, pages 321–328.

Lagendijk, A. and van Tiggelen, B. A. (1996). Resonant multiple scattering of light. *Physics Reports*, 270:143–215.

Lagendijk, A., van Tiggelen, B. A., and Wiersma, D. S. (2009). Fifty years of anderson localization. *Physics Today*, 62:24.

Lavor, C., Liberti, L., Lodwick, W., and da Costa, T. (2017). *An Introduction to Distance Geometry applied to Molecular Geometry.* SpringerBriefs in Computer Science. Springer International Publishing.

Lawrence, N., Trevino, J., and Dal Negro, L. (2012a). Aperiodic arrays of active nanopillars for radiation engineering. *Journal of Applied Physics*, 111:113101.

Lawrence, N., Trevino, J., and Dal Negro, L. (2012b). Control of optical orbital angular momentum by vogel spiral arrays of metallic nanoparticles. *Optics Letters*, 37(24):5076–5078.

Levine, D. and Steinhardt, P. J. (1984). Quasicrystals: A new class of ordered structures. *Physical Review Letters*, 53:2477–2480.

Levy, E. and Akkermans, E. (2017). Topological boundary states in 1d: An effective fabry-perot model. *The European Physics Journal Special Topics*, 226:1563–1582.

Levy, E., Barak, A., Fisher, A., and Akkermans, E. (2016). Topological properties of fibonacci quasicrystals: A scattering analysis of chern numbers. *arXiv:1509.04028*, (v3).

Li, K., Stockman, M. I., and Bergman, D. J. (2003). Self-similar chain of metal nanospheres as an efficient nanolens. *Physical Review Letters*, 91:227402.

Li, L., Li, T., Tang, X., Wang, S. M., Wang, Q. J., and Zhu, S. N. (2015). Plasmonic polarization generator in well-routed beaming. *Light: Science and Applications*, 4:e330.

Liew, S. F., Noh, H., Trevino, J., Dal Negro, L., and Cao, H. (2011). Localized photonic band edge modes and orbital angular momenta of light in a golden-angle spiral. *Optics Express*, 19(24):23631–23642.

Liu, L., Zhang, L., Kim, S. M., and Park, S. (2014). Helical metallic micro- and nanostructures: fabrication and application. *Nanoscale*, 6:9355–9365.

Liu, W., Miroshnichenko, A. E., Neshev, D. N., and Kivshar, Y. (2012). Broadband unidirectional scattering by magneto-electric coreshell nanoparticles. *ACS Nano*, 6(6):5489–5497.

Liu, W., Shi, J., Lei, B., Hu, H., and Miroshnichenko, A. E. (2015). Efficient excitation and tuning of toroidal dipoles within individual homogenous nanoparticles. *Optics Express*, 23:24738–24747.

Lu, D., Kan, J. J., Fullerton, E. E., and Liu, Z. (2014). Enhancing spontaneous emission rates of molecules using nanopatterned multilayer hyperbolic metamaterials. *Nature Nanotechnology*, 9:48–53.

Lucic, N. M., Savic, D. M. J., Piper, A., Grujic, D. Z., Vasiljevic, J. M., Pantelic, D. V., Jelenkovic, B. M., and Timotijevic, D. V. (2015). Light propagation in quasi-periodic fibonacci waveguide arrays. *Journal of the Optical Society of America B*, 32:1510.

Lumerical Solutions, I. `http://www.lumerical.com/tcad-products/fdtd/`.

Lumme, K. and Rohola, J. (1994). Light-scatterig by porous dust particles in the discrete-dipole approximation. *Astrophysical Journal*, 425:653–667.

Maciá, E. (2006). The role of aperiodic order in science and technology. *Reports on Progress in Physics*, 69:397.

Maciá, E. (2009). *Aperiodic Structures in Condensed Matter: Fundamentals and Applications*. CRC Press Taylor and Francis: Boca Raton, FL, USA.

Maciá, E. (2012). Exploiting aperiodic designs in nanophotonic devices. *Reports on Progress in Physics*, 75:036502.

Macia, E. (2014). On the nature of electronic wave functions in one-dimensional self-similar and quasiperiodic systems. *ISRN Condensed Matter Physics*, 2014.

Maciá, E. and Domínguez-Adame, F. (1996). Physical nature of critical wave functions in fibonacci systems. *Physical Review Letters*, 76:2957.

Macías, D., Adam, P.-M., Ruíz-Cortés, V., Rodríguez-Oliveros, R., and Sánchez-Gil, J. A. (2012). Heuristic optimization for the design of plasmonic nanowires with specific resonant and scattering properties. *Optics Express*, 20(12):13146–13163.

Maier, S. A. (2007). *Plasmonics: Fundamentals and Applications*. Springer, New York, NY.

Mandelbrot, B. B. (1977). *Fractal Geometry of Nature*. WH Freeman and Company: New York.

Marengo, E. A. and Devaney, A. J. (2004). Nonradiating sources with connections to the adjoint problem. *Physical Review E*, 70:037601.

Mark, A. G., Gibbs, J. G., Lee, T. C., and Fischer, P. (2013). Hybrid nanocolloids with programmed three-dimensional shape and material composition. *Nature Materials*, 12:802–807.

McPeak, K. M., Jayanti, S. V., Kress, S. J. P., Meyer, S., Iotti, S., Rossinelli, A., and Norris, D. J. (2015). Plasmonic films can easily be better: Rules and recipes. *ACS Photonics*, 2:326–333.

Mehta, M. L. (2004). *Random Matrices*. Elsevier, Amsterdam.

Menzel, C., Rockstuhl, C., Paul, T., and Lederer, F. (2008). Retrieving effective parameters for metamaterials at oblique incidence. *Physical Review B*, 77:195328.

Merlin, R., Bajema, K., Clarke, R., Juang, F. Y., and Bhattacharya, P. K. (1985). Quasiperiodic gaas-alas heterostructures. *Physical Review Letters*, 55:1768.

Michel, J., Liu, J., and Kimerling, L. C. (2010). High-performance ge-on-si photodetectors. *Nature Photonics*, 4:527–534.

Miroshnichenko, A. E., Evlyukhin, A. B., Yu, Y. F., Bakker, R. M., Chipouline, A., Kuznetsov, A. I., Lukyanchuk, B., Chichkov, B. N., and Kivshar, Y. S. (2015). Nonradiating anapole modes in dielectric nanoparticles. *Nature Communications*, 6:8069.

Mitchison, G. (1977). Phyllotaxis and the fibonacci series. *Science*, 196:270–275.

Mulholland, G. W., Bohren, C. F., and Fuller, K. A. (1994). Light scattering by agglomerates: Coupled electric an magnetic dipole method. *Langmuir*, 10:2533–2546.

Nanz, S. (2016). *Toroidal Multipole Moments in Classical Electrodynamics: An Analysis of their Emergence and Physical Significance*. Springer Fachmedien Wiesbaden.

Noh, J., Huang, S., Leykam, D., Chong, Y. D., Chen, K. P., and Rechtsman, M. C. (2017). Experimental observation of optical weyl pointsand fermi arc-like surface states. *Nature Physics*.

Novotny, L. and van Hulst, N. (2011). Antennas for light. *Nature Photonics*, 5:83–90.

Ogut, B., Talebi, N., Vogelgesang, R., Sigle, W., and van Aken, P. A. (2012). Toroidal plasmonic eigenmodes in oligomer nanocavities for the visible. *Nano Letters*, 12:5239–5244.

Ostfeld, A. E. and Pacifici, D. (2011). Plasmonic concentrators for enhanced light absorption in ultrathin film organic photovoltaics. *Applied Physics Letters*, 98:113112.

Ou, J. Y., Plum, E., Zhang, J., and Zheludev, N. I. (2013). An electromechanically reconfigurable plasmonics metamaterial operating in the near-infrared. *Nature Nanotechnology*, 8:252–255.

Pakizeh, T. (2012). Unidirectional radiation of a magnetic dipole coupled to an ultracompact nanoantenna at visible wavelengths. *Journal of the Optical Society of America B*, 29:2446–2452.

Palik, E. D. (1998). *Handbook of Optical Constants of Solids*. Academic.

Papasimakis, N., Fedotov, V. A., Savinov, V., Raybould, T. A., and Zheludev, N. I. (2016). Electromagnetic toroidal excitations in matter and free space. *Nature Materials*, 15:263–271.

Penrose, R. The role of aesthetic in pure and applied mathematical research. *Institute of Mathematics and its Applications*, 7(10):266–271.

Pinheiro, F. A., Rusek, M., Orlowski, A., and van Tiggelen, B. A. (2004). Probing anderson localization of light via decay rate statistics. *Physical Review E*, 69:026605.

Pinter, J. D. (2002). *In Handbook of Global Optimization*, volume 62. Springer: U.S.

Pollard, M. E. and Parker, G. J. (2009). Low-contrast bandgaps of a planar parabolic spiral lattice. *Optics Letters*, 34(18):2805–2807.

Pompa, P. P., Martiradonna, L., Torre, A. D., Sala, F. D., Manna, L., De Vittorio, M., Calabi, F., Cingolani, R., and Rinaldi, R. (2006). Metal-enhanced fluorescence of colloidal nanocrystals with nanoscale control. *Nature Nanotechnology*, 1:126–130.

Purcell, E. M. (1946). Spontaneous emission probabilities at radio frquencies. *Physical Review*, 69:674.

Queffelec, M. (2010). *Substitution Dynamical Systems-Spectral Analysis.* Springer: Berlin/Heidelberg, Germany.

Radescu, E. E. and Vaman, G. (2002). Exact calculation of the angular momentum loss, recoil force, and radiation intensity for an arbitrary source in terms of electric, magnetic, and toroidal multipoles. *Physical Review E*, 65:046609.

Radke, A., Gissibl, T., Klotzbcher, T., Braun, P. V., and Giessen, H. (2011). Three-dimensional bichiral plasmonic crystals fabricated by direct laser writing and electroless silver plating. *Advanced Materials*, 23:3018–3021.

Rao, S., Wilton, D., and Glisson, A. (1982). Electromagnetic scattering by surfaces of arbitrary shape. *IEEE Transactions on Antennas and Propagation*, 30(3):409–418.

Razi, M., Wang, R., He, Y., Kirby, R. M., and Dal Negro, L. (2018). Optimization of large-scale vogel spiral arrays of plasmonic nanoparticles. *Optics Express (in review).*

Rechtsman, M. C., Zeuner, J. M., Plotnik, Y., Lumer, Y., Podolsky, D., Dreisow, F., Nolte, S., Segev, M., and Szameit, A. (2013). Photonic floquet topological insulators. *Nature*, 496(12066).

Rodrguez-Fortuo, F. J., Marino, G., Ginzburg, P., OConnor, D., Martnez, A., Wurtz, G. A., and Zayats, A. V. (2013). Near-field interference for the unidirectional excitation of electromagnetic guided modes. *Science*, 340:328–330.

Rodríguez-Oliveros, R. and Sánchez-Gil, J. A. (2011). Localized surface-plasmon resonances on single and coupled nanoparticles through surface integral equations for flexible surfaces. *Optics Express*, 19(13):12208–12219.

Rusek, M., Mostowski, J., and Orlowski, A. (2000). Random green matrices: From proximity resonances to anderson localization. *Physical Review A*, 61:022704.

Saha, A. and Tewari, A. (2013). On the nonasymptotic convergence of cyclic coordinate descent methods. *SIAM Journal on Optimization*, 23(1):576–601.

Savinov, V., Fedotov, V. A., and Zheludev, N. I. (2014). Toroidal dipolar excitation and macroscopic electromagnetic properties of metamaterials. *Physical Review B*, 89:205112.

Senechal, M. (1995). *Aperiodic Order. Volume 1: A Mathematical Invitation.* Cambridge University Press: Cambridge, UK.

Shechtman, D., Blech, I., Gratias, D., and Cahn, J. W. (1984). Metallic phase with long-range orientational order and no translational symmetry. *Physical Review Letters*, 53:1951–1953.

Silveirinha, M. G. and Engheta, N. (2009). Transporting an image through a subwavelength hole. *Physical Review Letters*, 102:103902.

Skipetrov, S. E. and Goetschy, A. (2011). Eigenvalue distributions of large euclidean random matrices for waves in random media. *Journal of Physics A: Mathematical and Theoretical*, 44:065102.

Skipetrov, S. E. and Sokolov, I. M. (2015). Magnetic-field-driven localization of light in a cold-atom gas. *Physical Review Letters*, 114:053902.

Smajic, J., Hafner, C., Raguin, L., Tavzarashvili, K., and Mishrikey, M. (2009). Comparison of numerical methods for the analysis of plasmonic structures. *Journal of Computational and Theoretical Nanoscience*, 6:763774.

Song, C., Blaber, M. G., Zhao, G., Zhang, P., Fry, H. C., Schatz, G. C., and Rosi, N. L. (2013). Tailorable plasmonic circular dichroism properties of helical nanoparticle superstructures. *Nano Letters*, 13:3256–3261.

Soukoulis, C. M. and Wegener, M. (2011). Past achievements and future challenges in the development of three-dimensional photonic metamaterials. *Nature Photonics*, 5:523–530.

Staude, I., Miroshnichenko, A. E., Decker, M., Fofang, N. T., Liu, S., Gonzales, E., Dominguez, J., Luk, T. S., Neshev, D. N., Brener, I., and Kivshar, Y. (2013). Tailoring directional scattering through magnetic and electric resonances in subwavelength silicon nanodisks. *ACS Nano*, 7(9):7824–7832. PMID: 23952969.

Steurer, W. and Sutter-Widmer, D. (2007). Photonic and phononic quasicrystals. *Journal of Physics D: Applied Physics*, 40:R229.

Sugimoto, H., Chen, T., Wang, R., Fujii, M., Reinhard, B. M., and Dal Negro, L. (2015). Plasmon-enhanced emission rate of silicon nanocrystals in gold nanorod composites. *ACS Photonics*, 2:1298–1305.

Tan, C. L., Karar, A., Alameh, K., and Lee, Y. T. (2013). Optical absorption enhancement of hybrid-plasmonic-based metal-semiconductor-metal photodetector incorporating metal nanogratings and embedded metal nanoparticles. *Optics Express*, 21:1713–1725.

Tang, L., Kocabas, S. E., Latif, S., Okyay, A. K., Ly-Gagnon, D., Saraswat, K. C., and Miller, D. A. B. (2008). Nanometre-scale germanium photodetector enhanced by a near-infrared dipole antenna. *Nature Photonics*, 2:226–229.

Tao, T. (2006). The gaussian primes contain arbitrarily shaped constellations. *Journal d'Analyse Mathématique*, 99(1):109–176.

Tassadit, A., Macas, D., Snchez-Gil, J., Adam, P.-M., and Rodriguez-Oliveros, R. (2011). Metal nanostars: Stochastic optimization of resonant scattering properties. *Superlattices and Microstructures*, 49(3):288–293.

Trevino, J., Forestiere, C., Di Martino, G., Yerci, S., Priolo, F., and Dal Negro, L. (2012a). Plasmonic-photonic arrays with aperiodic spiral order for ultra-thin film solar cells. *Optics Express*, 20(S3):A418–A430.

Trevino, J., Liew, S. F. L., Noh, H., Cao, H., and Dal Negro, L. (2012b). Geometrical structure, multifractal spectra and localized optical modes of aperiodic vogel spirals. *Optics Express*, 20(3):3015–3033.

Trevino, J., Walsh, G. F., Pecora, E. F., Boriskina, S. V., and Dal Negro, L. (2013). Photonic plasmonic-coupled nanoantennas for polarization-controlled multispectral nanofocusing. *Optics Letters*, 38(22):4861–4863.

van Tiggelen, B. A., Maynard, R., and Nieuwenhuizen, T. M. (1996). Theory for multiple light scattering from rayleigh scatterers in magnetic fields. *Physical Review E*, 53:2881–2908.

Vardeny, Z. V., Nahata, A., and Agrawal, A. (2013). Optics of photonic quasicrystals. *Nature Photonics*, 7:177–187.

Verbin, M., Zilberberg, O., Lahini, Y., Kraus, Y. E., and Silberberg, Y. (2015). Topological pumping over a photonic fibonacci quasicrystal. *Physical Review B*, 91:064201.

Wang, K. X., Yu, Z., Liu, V., Cui, Y., and S.Fan (2012). Absorption enhancement in ultrathin crystalline silicon solar cells with antireflection and light-trapping nanocone gratings. *Nano Letters*, 12(3):1616–1619.

Wang, R. and Dal Negro, L. (2016). Engineering non-radiative anapole modes for broadband absorption enhancement of light. *Optics Express*, 24(17):19048–19062.

Wang, R., Forestiere, C., and Dal Negro, L. (2015). Radiative properties of diffractively-coupled optical nano-antennas with helical geometry. *Optics Express*, 23(20):25496–25508.

Wang, R., Pinheiro, F. A., and Dal Negro, L. (2018a). Spectral statistics and scattering resonances of complex primes arrays. *Physical Review B*, 97:024202.

Wang, R., Rontgen, M., Morfonios, C. V., Pinheiro, Felipe A.and Schmelcher, P., and Dal Negro, L. (2018b). Edge modes of scattering chains with aperiodic order. *arXiv:1801.03550.*

Wang, Y., Overvig, A. C., Shrestha, S., Zhang, R., Wang, R., Yu, N., and Dal Negro, L. (2017). Tunability of indium tin oxide materials for mid-infrared plasmonics applications. *Optical Materials Express*, 7(8):29.

Warner, M. and Terentjev, E. M. (2003). *Liquid Crystal Elasomers, International Series of Monographs on Physics 120.* Oxford Science Publications, UK.

Wolf, M. (1997). 1/f noise in the distribution of prime numbers. *Physica A*, 241:493.

Wright, S. J. (2015). Coordinate descent algorithms. *Mathematical Programming*, 151(1):3–34.

Wu, T. T. and Lange, K. (2008). Coordinate descent algorithms for lasso penalized regression. *The Annals of Applied Statistics*, pages 224–244.

Xiao, M. and Fan, S. (2017). Photonic chern insulator through homogenization of an array of particles. *Physical Review B*, 96(10):100202.

Xiong, F., Zhang, J., Zhu, Z., Yuan, X., and Qin, S. (2015). Ultrabroadband, more than one order absorption enhancement in graphene with plasmonic light trapping. *Scientific Reports*, 5:16998.

Yang, J.-K., Boriskina, S. V., Noh, H., Rooks, M. J., Solomon, G. S., Dal Negro, L., and Cao, H. (2010). Demonstration of laser action in a pseudorandom medium. *Applied Physics Letters*, 97:223101.

Yang, W.-H., Schatz, G. C., and Van Duyne, R. P. (1995). Discrete dipole approximation for calculating extinction and raman intensities for small particles with arbitrary shapes. *The Journal of Physical Chemistry B*, 103(3):869–875.

Yao, J., Yang, M., and Duan, Y. (2014). Chemistry, biology, and medicine of fluorescent nanomaterials and related systems: New insights into biosensing, bioimaging, genomics, diagnostics, and therapy. *Chemical Reviews*, 114:6130–6178.

Ye, J. C., Webb, K. J., Bouman, C. A., and Millane, R. P. (1999). Optical diffusion tomography by iterative-coordinate-descent optimization in a bayesian framework. *Journal of the Optical Society of America. A*, 16(10):2400–2412.

Yla-Oijala, P. and Taskinen, M. (2005). Application of combined field integral equation for electromagnetic scattering by dielectric and composite objects. *IEEE Transactions on Antennas and Propagation*, 53:1168–1173.

Yu, N., Wang, Q. J., Pflugl, C., Diehl, L., Capasso, F., Edamura, T., Furuta, S., Yamanishi, M., and Kan, H. (2009). Semiconductor lasers with integrated plasmonic polarizers. *Applied Physics Letters*, 94:151101.

Yurkin, M. and Hoekstra, A. (2007). The discrete dipole approximation: An overview and recent developments. *Journal of Quantitative Spectroscopy and Radiative Transfer*, 106(1):558 – 589. IX Conference on Electromagnetic and Light Scattering by Non-Spherical Particles.

Zel'dovich, Y. (1957). Electromagnetic interaction with parity violation. *Zhurnal Eksperimentalnoi i Teoreticheskoi Fiziki*, 33:1531.

Zeman, E. J. and Schatz, G. C. (1987). An accurate electromagnetic theory study of surface enhancement factors for ag, au, cu, li, na, ai, ga, in, zn, and cd. *The Journal of Physical Chemistry*, 91(3):634–643.

Zhang, X. and Wu, Y. (2015). Effective medium theory for anisotropic metamaterials. *Scientific Reports*, 5:7892.

Zhao, L., Kelly, K. L., and Schatz, G. C. (2003). The extinction spectra of silver nanoparticle arrays: Influence of array structure on plasmon resonance wavelength and width. *The Journal of Physical Chemistry B*, 107(70):7343–7350.

Zharekeshev, I. K. and Kramer, B. (1997). Asymptotics of universal probability of neighboring level spacings at the anderson transition. *Physical Review Letters*, 79(4).

Zheludev, N. I. and Plum, E. (2016). Reconfigurable nanomechanical photonic metamaterials. *Nature Nanotechnology*, 11:16–22.

Zuo, Z. and Wu, C. (1989). Successive approximation technique for a class of large-scale nlp problems and its application to dynamic programming. *Journal of optimization theory and applications*, 62(3):515–527.

CURRICULUM VITAE

[redacted]

[redacted]

[redacted]